Multi-Higgs Production at Future Hadron Colliders

Dissertation

zur Erlangung des akademischen Grades eines Doktors der Naturwissenchaften

vorgelegt von

Zhijie Zhao

eingereicht bei der Naturwissenschaftlich-Technische Fakultät

Universität Siegen

Siegen, November 2018

Gutachter der Dissertation:	Prof. Dr. Wolfgang Kilian
	Dr. Oscar Cata
Datum der Disputation:	07.01.2019
Prüfungskommission:	Prof. Dr. Wolfgang Kilian
	Dr. Oscar Cata
	Prof. Dr. Thomas Mannel
	Prof. Dr. Ivor Fleck

Eidesstattliche Erklärung

Ich versichere, dass ich die Arbeit ohne fremde Hilfe und ohne Benutzung anderer als der angegebenen Quellen angefertigt habe und dass die Arbeit in gleicher oder ähnlicher Form noch keiner anderen Prüfungsbehörde vorgelegen hat und von dieser als Teil einer Prüfungsleistung angenommen wurde. Alle Ausführungen, die wörtlich oder sinngemäß übernommen wurden, sind als solche gekennzeichnet.

Siegen, den 26. November 2018

Abstract

The Standard Model of particle physics is a successfully tested theory to describe interactions of elementary particles. However, experimental data hints us at possible new physics beyond Standard Model should exist. After the discovery of the Higgs boson, measurements of its property and couplings to other particles are essential to search for new physics.

Multi-Higgs production processes are important to reconstruct the Higgs potential and to study the mechanism of electroweak symmetry breaking. Possible new physics deviation can be observed in these processes. We study the multi-Higgs production via gluon-gluon fusion and vector-boson fusion at hadron collider using an effective Lagrangian to describe potential new physics.

For the multi-Higgs production process via gluon-gluon fusion, we explore the potential for the discovery of the triple-Higgs signal in the $2b2l^{\pm}4j + \not{E}$ decay channel at a 100 TeV hadron collider. Our detector analysis shows that the discovery of Standard Model signals via this channel is a challenging task for the future hadron collider. Combined with the projected constraints from single and double Higgs-boson production, the measurement of triple Higgs process can further reduces the allowed parameter space.

For the multi-Higgs production process via vector-boson fusion, our numerical calculation shows the energy dependence of the effective parameters. Experimentally, a measurement of triple-Higgs final state via vector-boson fusion process is very challenging due to its small cross section, even on future high energy colliders, but the constraints on anomalous couplings should be obtained. Our numerical results describe the potential for constraining these couplings at the LHC and at future hadron colliders. We also derive theoretical constraints on the parameter space from the unitarity of $2 \to n$ scattering amplitudes and apply the results to $VV \to hh$ and hhh processes.

Zusammenfassung

Das Standard-Modell der Teilchenphysik ist die erfolgreich getestete Theorie zur Beschreibung von Wechselwirkung von Elementarteilchen. Jedoch deuten Daten aus Experimenten daraufhin, dass mögliche Physik jenseits des Standard-Modells existiere. Nach der Entdeckung des Higgs-Boson ist die Bestimmung seiner Eigenschaften sowie Kopplung zu anderen Teilchen essentiell für die Suche nach neuer Physik.

Multi-Higgs-erzeugende Prozesse sind daher wichtig, um die Form des Higgs-Potential zu rekonstruieren und um die Wirkungsweise der elektroschwachen Symmetriebrechnnung zu studieren. Wir untersuchen die Multi-Higgs-Erzeugung durch Gluon-Gluon-Fusion und Vektorboson-Fusion an Hadronen-Kollidern mithilfe einer effektiven Lagrangedichte, welche mögliche neue Physik beschreibt.

Für den Multi-Higgs-erzeugenden Prozess durch Gluon-Gluon-Fusion studieren wir das Potential zur Entdeckung des dreifachen Higgs-Singal im $2b2l^{\pm}4j + \not{E}$ Zerfallskanal bei einem 100 TeV Hadronen-Kollider. Unsere Detektor-Analyse zeigt, dass die Entdeckung von Standard-Modell Signalen über diese Produktionskanäle eine herausfordernde Aufgabe für einen zukünftigen Hadronen-Kollider ist. Zusammen mit den projizierten Randbedingungen aus einfacher und zweifacher Higgs-Boson-Erzeugung kann die Messung der dreifachen Higgs-Boson-Erzeugung den erlaubten Parameterraum weiter einschränken.

Für den Multi-Higgs-erzeugenden Prozess durch Vektorboson-Fusion zeigen unsere numerischen Berechnungen die Energieabhängigkeit der effektiven Parameter. Experimentell ist die Messung des dreifachen Higgs-Endzustands über Vektorboson-Fusionsprozesse aufgrund des im Vergleich kleinen Wirkungsquerschnitt sehr herausfordernd, selbst mit einem zukünftigen Hochenergie-Kollider. Jedoch sollten Einschränkungen für anomale Kopplungen bestimmbar sein. Unsere Resultate beschreiben mögliche Einschränkungen für diese Kopplungen am LHC und an einem zukünftigen Hadronen-Kollider. Wir bestimmen darüber hinaus Bedingungen für den Parameterraum basierend auf der Unitarität von $2 \rightarrow n$ Streuungsamplituden und wende diese auf die Resultate von $V \rightarrow hh$ und hhh Prozessen an.

Contents

List of Figures

List of Tables

Chapter 1

Introduction

Modern particle physics suggests that all matter is composed of elementary particles. Three of the four fundamental interactions (the electromagnetic, weak and strong interactions) between elementary particles can be described by a quantum field theory, namely the Standard Model (SM). The up-to-date experimental measurements are consistent with the SM pridictions. In particular, the discovery of the Higgs boson at Large Hadron Collider (LHC) has completed the picture of the SM [1, 2].

However, it is known that the SM is not a complete theory for our universe. First of all, the forth kind of fundamental interaction, gravitational interaction, is not included in the SM framework. The SM also cannot answer some questions, such as dark matter and dark energy, matter-antimatter asymmetry, and the neutrion oscillations. It is expected that physics beyond SM should exists, namely New Physics (NP). Searching for NP is the main task for physicists.

Though Higgs boson is discovered, its property is still under investigation. Measurements of Higgs boson coupling to SM particles are essential for the search for NP. The SM predicts that the Higgs boson has three types of interaction at tree level: (1) the Yukawa interactions with fermions; (2) the interaction with electroweak gauge bosons ($W^\pm$ and Z); (3) the triple and quartic Higgs self-interactions. A measurement of the last type of interaction can provide the knowledge of the Higgs potential and the electroweak symmetry breaking (EWSB). Furthermore, Higgs self-interactions are also related to the problems of baryogenesis [3] and vacuum stability [4, 5, 6]. However, any measurement of triple and quartic self-coupling of Higgs involves two or more Higgs boson production in a collider process. The production rates of these processes are small at the LHC, even if it is upgraded to 14 TeV. So it is challenging to measure these couplings. At a 100 TeV hadron collider, the rate for these processes will be enhanced significantly. Accurate measurements of triple and quartic self-coupling become possible.

In this thesis, we study multi-Higgs production at LHC and a future 100 TeV collider. Two production modes are considered: (1) multi-Higgs production via gluon-gluon-fusion (ggF); (2) multi-Higgs production via vector-boson-fusion (VBF). The computations of cross sections and events generation of these processes are performed by Monte-Carlo (MC) generator WHIZARD [7] or Madgraph [8]. We analyze these processes in an effective field theory (EFT) framework, and obtain projections for

bounds on the parameters.

   This thesis is organized as follows. In Chapter 2 we give a brief introduction to the SM. In Chapter 3 we describe the EFT framework and its parameterization. Chapter 4 presents the project of the multi-Higgs production via ggF mode. We explore the potential for the discovery of the triple-Higgs signal in the $2b2l^{\pm}4j + \not{E}$ decay channel at a 100 TeV hadron collider. The NP effects are studied in the EFT framework given in Chapter 3. This chapter is based on our results in Ref. [9]. Chapter 5 shows the results of our analysis for multi-Higgs production via VBF mode. We derive the unitarity constraints of $2 \to n$ scattering amplitudes and apply the results to $VV \to hh$ and hhh processes. The cross sections are computed numerically with appropriate VBF cuts for 14 TeV, 27 TeV, and 100 TeV, respectively. The projected bounds on the EFT parameters are also obtained. The results of this chapter are based on our paper [10]. Finally, our conclusion is given in Chapter 6.

Chapter 2

The Standard Model of Particle Physics

The Standard Model (SM) is a quantum field field to describe the electromagnetic, strong and weak interactions of elementary particles. The elementary particles can be distinguish to fermions and bosons. The fermions contains 6 quarks and 6 leptons. For the quarks, they are named by up (u), down (d), strange (s), charm (c), bottom (b) and top (t). The 6 leptons are called electron (e), muon (μ), tau (τ) with their corresponding neutrino ν_e, ν_μ and ν_τ. All fermions have their anti-particles with the same mass and spin but opposite charge. The interactions between fermions is carried by gauge bosons. Photon (γ) is the carrier of the electromagnetic interactions. The strong interactions are mediated by gluon (g). The $W^\pm$ and Z boson are the carrier of the weak interactions. Finally, the Higgs boson is needed in the spontaneous symmetry breaking, and gives the mass of $W^\pm$ and Z. The properties of these particles are listed in Table. 2.1, where the data are taken from Ref. [11].

After the discovery of the Higgs boson in 2012 [1, 2], the picture of SM is completed. The SM has been proved to be a good theory to describe the properties of elementary particles. This chapter gives an overview of the Standard Model of particle Physics. The contents of this chapter can be found in many textbooks, for example [12, 13, 14].

2.1 Quantum Chromodynamics

Quantum Chromodynamics (QCD) is the gauge field theory of strong interactions. The symmetry group of QCD is $SU(3)_C$. The subscript C means color. There are three types of color (usually labelled by R,G,B) and quarks carry a color charge, while gluons are made by a color charge and an anti-color charge. We can use q_i to represent the quark field with color index i and write down the QCD Lagrangian

$$\mathcal{L}_{QCD} = -\frac{1}{4}G^a_{\mu\nu}G^{a,\mu\nu} + \sum_{q=u,d,s,...} \bar{q}_i(i\slashed{D} - m_q\delta_{ij})q_j, \tag{2.1}$$

Class	Name	Spin	Charge	Mass
Quark	up(u)	1/2	+2/3	2.2 MeV
	down(d)	1/2	−1/3	4.7 MeV
	charm(c)	1/2	+2/3	1.275 GeV
	strange(s)	1/2	−1/3	95.0 MeV
	top(t)	1/2	+2/3	173.0 GeV
	bottom(b)	1/2	−1/3	4.18 GeV
Lepton	electron(e)	1/2	−1	0.51 MeV
	electron neutrino(ν_e)	1/2	0	< 2 eV
	muon(μ)	1/2	−1	105.66 MeV
	muon neutrino(ν_μ)	1/2	0	< 2 eV
	tau(τ)	1/2	−1	1.777 GeV
	tau neutrino(ν_τ)	1/2	0	< 2 eV
Gauge boson	photon(γ)	1	0	0
	Z boson(Z)	1	0	91.1876 GeV
	W boson($W^\pm$)	1	±1	80.379 GeV
	gluon(g)	1	0	0
Scalar boson	Higgs boson(h)	0	0	125.18 GeV

Table 2.1: The elemental particles in SM and their properties are listed. The numbers are taken from Ref. [11].

where m_q denotes the mass of the corresponding quark. In this Lagrangian, the gluons are described by the field strength tensor

$$G_{\mu\nu}^a = \partial_\mu G_\nu^a - \partial_\nu G_\mu^a - g_s f_{abc} G_\mu^b G_\nu^c, \tag{2.2}$$

where $G_\mu^a (a = 1, 2, ..., 8)$ is the gluon field, f_{abc} are the $SU(3)$ structure constants, and g_s is the coupling constant of strong interation. The covariant derivative $\slashed{D}$ is defined by

$$\begin{aligned} \slashed{D} &= \gamma^\mu D_\mu \\ &= \gamma^\mu (\partial_\mu - i g_s G_\mu^a \frac{\lambda^a}{2}) \end{aligned} \tag{2.3}$$

where λ^a denotes the Gell-Mann matrices, corresponding to the $SU(3)$ generators.

Eq. 2.1 predicts the quark-gluon vertex and the self-interaction of three or four gluons.

2.2 The electroweak interaction

The electroweak theory is based on an $SU(2)_L \times U(1)$ gauge group. The electroweak Lagrangian contains three gauge boson $W^i (i = 1, 2, 3)$, associated with the $SU(2)_L$ group, and one gauge boson

B, associated with the $U(1)$ group. Analogy to QCD, the kinetic terms of the gauge bosons can be written as

$$\mathcal{L}_G = -\frac{1}{4} W^i_{\mu\nu} W^{i,\mu\nu} - \frac{1}{4} B_{\mu\nu} B^{\mu\nu}, \tag{2.4}$$

where the field strength tensors $W^i_{\mu\nu}$ and $B_{\mu\nu}$ are

$$W^i_{\mu\nu} = \partial_\mu W^i_\nu - \partial_\nu W^i_\mu - g_W \epsilon^{ijk} W^j_\mu W^k_\nu, \tag{2.5}$$

$$B_{\mu\nu} = \partial_\mu B_\nu - \partial_\nu B_\mu, \tag{2.6}$$

where g_W is the $SU(2)_L$ gauge coupling and ϵ^{ijk} is the total antisymmetric tensor. The coupling of the gauge bosons to fermion is implemented by defining the covariant derivative

$$D_\mu = \partial_\mu - ig_W T^i W^i_\mu - iY g'_W B_\mu. \tag{2.7}$$

$T^i = \sigma^i/2$, where σ^i are the Pauli matrics, are a representation of the $SU(2)$ weak isospin algebra. Analogy to g_W, g'_W is the coupling of $U(1)$ group. The $U(1)$ charge Y is called weak hypercharge. The electric charge, Q, of a elemental particle is always

$$Q = T^3 + Y \tag{2.8}$$

The $SU(2)_L$ also means only the left-handed fermions transform as a doublet under this symmetry, while the right-handed fermions transform as a singlet. The fermions field can be written as

$$\psi_L = \gamma_L \begin{pmatrix} \nu_e \\ e \end{pmatrix}, \gamma_L \begin{pmatrix} \nu_\mu \\ \mu \end{pmatrix}, \gamma_L \begin{pmatrix} \nu_\tau \\ \tau \end{pmatrix}, \gamma_L \begin{pmatrix} u \\ d \end{pmatrix}, \gamma_L \begin{pmatrix} c \\ s \end{pmatrix}, \gamma_L \begin{pmatrix} t \\ b \end{pmatrix}, \tag{2.9}$$

$$\psi_R = \gamma_R e, \gamma_R \mu, \gamma_R \tau, \gamma_R u, \gamma_R d, \gamma_R c, \gamma_R s, \gamma_R t, \gamma_R b, \tag{2.10}$$

where the left- and right-handed projectors are

$$\gamma_L = \frac{1}{2}(1 - \gamma_5), \gamma_R = \frac{1}{2}(1 + \gamma_5). \tag{2.11}$$

The couplings of fermions to the gauge bosons can be described by the Lagrangian

$$\mathcal{L}_F = \bar{\psi}_L i \slashed{D}_L \psi_L + \bar{\psi}_R i \slashed{D}_R \psi_R, \tag{2.12}$$

where $\slashed{D}_L = \gamma^\mu(\partial_\mu - ig_W T^i W^i_\mu - iY_L g'_W B_\mu)$ and $\slashed{D}_R = \gamma^\mu(\partial_\mu - iY_R g'_W B_\mu)$. This means that the third projection of isospin T^3 and weak hypercharge Y are different for left- and right-handed fermions. Table. 2.2 lists the numbers of T^3 and Y for quarks and leptons, so the relation Eq. 2.8 is always satisfied.

Fermion	T_L^3	Y_L	T_R^3	Y_R	Q
u, c, t	$+\frac{1}{2}$	$+\frac{1}{6}$	0	$+\frac{2}{3}$	$+\frac{2}{3}$
d, s, b	$-\frac{1}{2}$	$+\frac{1}{6}$	0	$-\frac{1}{3}$	$-\frac{1}{3}$
ν_e, ν_μ, ν_τ	$+\frac{1}{2}$	$-\frac{1}{2}$	$-$	$-$	0
e, μ, τ	$-\frac{1}{2}$	$-\frac{1}{2}$	0	-1	-1

Table 2.2: The weak isospin and hypercharge of left-handed (with subscript L) and right-handed (with subscript R) fermion.

We can write down a Lagrangian for electroweak interaction now:

$$\mathcal{L}'_{EW} = \mathcal{L}_G + \mathcal{L}_F. \tag{2.13}$$

The mass terms are absent in this Lagrangian, because they are forbidden by the $SU(2)_L \times U(1)$ symmetry. However, Table 2.1 shows that fermions and electroweak gauge bosons are massive. It is necessary to introduce a mechanism of the symmetry breaking which can give mass to these particles. This mechanism is well known as Higgs mechanism [15, 16], which is explained in the next section.

2.3   Higgs mechanism

In the SM, the $SU(2)_L \times U(1)$ symmetry is broken by introducing a doublet

$$H \;=\; \begin{pmatrix} \phi^+ \\ \phi^0 \end{pmatrix}. \tag{2.14}$$

Both ϕ^+ and ϕ^0 are complex. The mechanics of this doublet is described by Lagrangian

$$\mathcal{L}_H = (D^\mu H)^\dagger (D_\mu H) - V(H^\dagger H), \tag{2.15}$$

where the D_μ is defined by Eq. 2.7. The Higgs potential $V(H^\dagger H)$ is

$$V(H^\dagger H) = -\mu^2 (H^\dagger H) + \lambda (H^\dagger H)^2, \tag{2.16}$$

where $\mu^2, \lambda > 0$. This potential has a minimum when $H^\dagger H = 2\mu^2/\lambda$. The miminal value of the Higgs doublet can be chosen as

$$\langle H \rangle \;=\; \frac{1}{\sqrt{2}} \begin{pmatrix} 0 \\ v \end{pmatrix}, \tag{2.17}$$

where $v = \sqrt{\mu^2/\lambda}$ is called vacuum expectation value (VEV).

Since ϕ^+ and ϕ^0 are complex, the Higgs doublet has 4 degrees of freedom, we can reparameterize the Higgs doublet as

$$H = U^{-1}(\xi) \begin{pmatrix} 0 \\ (h+v)/\sqrt{2} \end{pmatrix}, \tag{2.18}$$

$$U(\xi) = \exp\left(-iT^i\xi^i/v\right), \tag{2.19}$$

where h and $\xi^i (i = 1, 2, 3)$ are four real degrees of freedom. With this parameterization, we can make a gauge transformation

$$H \rightarrow U(\xi)H, \tag{2.20}$$

$$T^i W^i_\mu \rightarrow UT^i W^i_\mu U^{-1} + \frac{i}{g_W}(\partial^\mu U)U^{-1}. \tag{2.21}$$

So the ξ^i degrees are eliminated, and only the physical degree h is remained. This gauge is called unitary gauge. In the unitary gauge, the Higgs doublet can be written in the following form

$$H = \frac{1}{\sqrt{2}} \begin{pmatrix} 0 \\ v+h \end{pmatrix}. \tag{2.22}$$

Now the Lagrangian Eq. 2.15 becomes

$$\mathcal{L}_H = \frac{1}{2}\partial^\mu h \partial_\mu h - V\left(\frac{(v+h)^2}{2}\right) + \frac{g_W^2}{4}(v+h)^2 W^-_\mu W^{+,\mu} + \frac{g_W^2}{8\cos^2\theta}(v+h)^2 Z_\mu Z^\mu, \tag{2.23}$$

where θ is the electroweak mixing angle with definition

$$\cos^2\theta = \frac{g_W^2}{g_W^2 + g_W'^2}. \tag{2.24}$$

The physical $W^\pm$ and Z field are mixed by the field strength W^i and B:

$$Z_\mu = \cos\theta W^3_\mu - \sin\theta B_\mu, \tag{2.25}$$

$$W^+_\mu = \frac{1}{\sqrt{2}}\left(W^1_\mu - iW^2_\mu\right), \tag{2.26}$$

$$W^-_\mu = \frac{1}{\sqrt{2}}\left(W^1_\mu + iW^2_\mu\right). \tag{2.27}$$

Eq. 2.23 shows that the $W^\pm$ and Z boson can obtain masses

$$m_W = \frac{g_W v}{2}, m_Z = \frac{g_W v}{2\cos\theta} \tag{2.28}$$

The remained gauge boson is photon

$$A_\mu = \sin\theta W_\mu^3 + \cos\theta B_\mu, \tag{2.29}$$

which is absent in the Eq. 2.23, so its mass is zero.

The coefficients of $hW_\mu^- W^{+,\mu}$ term and $hZ_\mu Z^\mu$ term in the Eq. 2.23 define the couplings of Higgs boson to gauge bosons pair:

$$g_{hWW} = \frac{g_W^2 v}{2} = \frac{2m_W^2}{v}, \tag{2.30}$$

$$g_{hZZ} = \frac{g_W^2 v}{4\cos^2\theta} = \frac{m_Z^2}{v}. \tag{2.31}$$

Similarly, the quartic couplings of Higgs bosons pair to gauge bosons pair are defined by

$$g_{hhWW} = \frac{g_W^2}{4} = \frac{m_W^2}{v^2}, \tag{2.32}$$

$$g_{hhZZ} = \frac{g_W^2}{8\cos^2\theta}\frac{m_Z^2}{2v^2}. \tag{2.33}$$

In the unitary gauge, the Higgs potential Eq. 2.16 is expanded to

$$V(h) = \mu^2 h^2 + \lambda v h^3 + \frac{\lambda}{4}h^4. \tag{2.34}$$

This expression defines the Higgs triple and quartic self-coupling:

$$g_{hhh} = 6\lambda v = \frac{3m_h^2}{v}, \tag{2.35}$$

$$g_{hhhh} = 6\lambda = \frac{3m_h^2}{v^2}, \tag{2.36}$$

where $m_h = \sqrt{2}\mu = \sqrt{2\lambda}v$ is the mass of Higgs boson. Since $v \approx 246$ GeV and the masses of these particles have been measured in experiments, the parameters in the Eq. 2.23 are completely fixed. However, the Higgs potential defined by Eq. 2.16 is the simplest form to obtain a VEV. Independent measurements of these couplings are necessary to understand the shape of the Higgs potential.

2.4 Yukawa interaction

In the SM, the Higgs boson couples to fermions via Yukawa interaction. The Lagrangian of Yukawa interaction can be written as

$$\mathcal{L}_Y = -\sum_f (y_f \bar{\psi}_{f,L} H \psi_{f,R} + h.c.), \tag{2.37}$$

where $\psi_{f,L}$ is the left-handed doublet of fermion f, while $\psi_{f,R}$ is the right-handed singlet. After spontaneous symmetry breaking, a mass term $m_f \bar{\psi}_{f,L} \psi_{f,R} = y_f v/\sqrt{2} \bar{\psi}_{f,L} \psi_{f,R}$ is generated. So the Yukawa coupling is propotional to the fermion mass, $y_f = \sqrt{2} m_f/v$. Because the wide range of the fermion mass, it is easy to measure Yukawa coupling of heavy fermions like top quark, but it is very challenge to measure the light fermions like electron.

2.5 Summary of SM

From the previous sections, we can finally write down the complete Lagrangian for electroweak interaction:

$$\mathcal{L}_{EW} = \mathcal{L}_G + \mathcal{L}_F + \mathcal{L}_H + \mathcal{L}_Y. \tag{2.38}$$

The SM Lagrangian is combined by the $\mathcal{L}_{QCD}$ and $\mathcal{L}_{EW}$

$$\mathcal{L}_{SM} = \mathcal{L}_{QCD} + \mathcal{L}_{EW}. \tag{2.39}$$

It can describe the strong, electromagnetic and weak interaction of elemental particles. The modern experiments of particle physics have proved that SM is good model to understand the interaction of elemental particles. However, the SM cannot answer some quetions, such as

- Why only the left-handed neutrino exists?

- Why the masses of fermions and their Yukawa couplings are required in a wide range?

In addition, the experimental data of Higgs boson is not sufficient to determine its couplings to other particles or itself. At the LHC, Higgs couplings are measured through the Higgs decays process. The cross-section measurement of $h \to WW^*$ and $h \to ZZ^*$ can be found in [17, 18]. The observed signal strengths are $1.05 \sim 1.29$ times the SM prediction, which gives a strong bound on couplings g_{hWW} and g_{hZZ}. For the Higgs trilinear self-coupling, it is constrained by measuring double Higgs production at LHC. Current data give a weak constraint $g_{hhh}/g_{hhh}^{SM} \in [-8.82, 15.04]$ [19]. Since Yukawa couplings are proportional to the masses of fermions in the SM, the Yukawa coupling of top quark is the most easy to be determine. At the LHC, the Yukawa coupling of top quark is measured by observing the $pp \to ht\bar{t}$ process. Data show that the cross section is $1.26^{+0.31}_{-0.26}$ times SM value [20], which gives a strong constraint on the Yukawa coupling of top quark. The experimental results for other couplings are not reported in the literature at present.

It is very interesting to study the couplings of Higgs boson and how NP effects can contribute to the collider process involved Higgs boson.

Chapter 3

The Effective Field Theory

Since the SM cannot answer some quetions in our nature, it suggests that the SM is an effective theory in the low energy scale. In the high energy, new physics (NP) beyond the SM should exist. Many NP models predict one or more particles with multi-TeV mass. It is difficult to detect these particles in current collider experiments. Fortunately, the heavy particles can affect the production rate of SM particles at collider. To study the NP effects from these heavy partilces, a model independent method is effective field theory (EFT) [21, 22, 23, 24]. In the language of EFT, the heavy partilces are integrated out and higher-dimensional operators are remained.

A valid EFT should have following features [25]:

- Any extension of the SM should satisfy the unitarity condition of S-matrix.

- The Lorentz invariance and the $SU(3)_C \times SU(2)_L \times U(1)$ symmetry should be conserved.

- The SM should be recovered in an appropritate limit.

- The extended theory should be general enough to describe any physics beyond the SM, but should lead us to the place where the NP effects probably appear.

- It should be able to calculate the radiative corrections at any order in the SM interactions.

- It should be able to calculate the radiative corrections at any order in the NP interactions.

Generally, the EFT Lagrangian can be written as

$$\mathcal{L}_{EFT} = \mathcal{L}_{SM} + \frac{1}{\Lambda} \sum_k c_k^{(5)} \mathcal{O}_k^{(5)} + \frac{1}{\Lambda^2} \sum_k c_k^{(6)} \mathcal{O}_k^{(6)} + ... \tag{3.1}$$

where $\mathcal{O}_k^{(n)}$ denote the operators with dimension-n, and $c_k^{(n)}$ are dimensionless coefficients. Λ is the cutoff scale of the EFT. If $c_k^{(n)}$ are order one parameters, the EFT is only valid when the energy is below this scale. In previous chapter, we know that the Lagrangian $\mathcal{L}_{SM}$ only includes dimension-2

or dimension-4 operators. In an EFT, one can add the operators with dimension-5 or more. Once the NP model is specified, the coefficients $c_k^{(n)}$ are determined by integrating out the heavy particles.

All dimension-5 operators violate the lepton number conservation [26], while all dimension-7 operators violate the baryon number minus lepton number conservation [27]. So it is expected that the leading NP effects come from dimension-6 operators.

The full set of operators up to dimension-6 was introduced by Buchmuller and Wyler [21], but many operators are redundant. Many authors published their minimal basis of dimension-6 operators such as GIMR basis [28] and SILH basis [29].

3.1 EFT Lagrangian of the mass eigenstates

In collider experiment, the coefficients $c_k^{(n)}$ are translated from the experimental data. It is convenient to define an EFT Lagrangian of mass eigenstates. In this context, only the interactions relevant to Higgs boson are considered. After electroweak symmetry breaking and expressed in unitarity gauge, the EFT Lagrangian can be written as

$$\mathcal{L}_{EFT} = \mathcal{L}_{\overline{SM}} + \mathcal{L}_t + \mathcal{L}_{ggh} + \mathcal{L}_{Vh} + \mathcal{L}_{VVh} + \mathcal{L}_h, \tag{3.2}$$

where $\mathcal{L}_{\overline{SM}}$ is the SM Lagrangian after removing the Higgs interactions. $\mathcal{L}_t$, $\mathcal{L}_{ggh}$, $\mathcal{L}_{Vh}$, $\mathcal{L}_{VVh}$, and $\mathcal{L}_h$ are the terms of the effective Yukawa interactions, Higgs-gluon interactions, SM-like Higgs-vector-boson interactions, tensor structure interactions of Higgs to vector boson, and Higgs self-interactions, respectively. If we truncate this Lagrangian at dimension-6, we can obtain relations of its coefficients to any basis of dimension-6 operators.

The $\mathcal{L}_t$ is defined as

$$\mathcal{L}_t = -a_1 \frac{m_t}{v} \bar{t} t\, h - a_2 \frac{m_t}{2v^2} \bar{t} t\, h^2 - a_3 \frac{m_t}{6v^3} \bar{t} t\, h^3, \tag{3.3}$$

where t is the physical field of top quark, and m_t is the mass of top quark. In previous chapter, we know that the couplings of Higgs to fermions are depended on the mass of fermions, so it is reasonable to consider the Yukawa coupling of top quark only. In the SM, we have $a_1 = 1$ and $a_2 = a_3 = 0$. Principally, one can construct operators with other Lorentz structure, but this is beyond the scope of this thesis.

The Higgs-gluon interactions term $\mathcal{L}_{ggh}$ is

$$\mathcal{L}_{ggh} = \frac{g_s^2}{48\pi^2} \left(c_1 \frac{h}{v} + c_2 \frac{h^2}{2v^2} \right) G_{\mu\nu}^a G^{a\,\mu\nu}. \tag{3.4}$$

In the SM, the couplings of Higgs to gluon is absent at tree level, and $c_1 = c_2 = 0$.

The Higgs boson couplings to a pair of physical vector boson fields are defined by

$$
\begin{aligned}
\mathcal{L}_{VH} &= g_{W,a1}\frac{2m_W^2}{v}hW^{+,\mu}W_\mu^- + g_{W,a2}\frac{m_W^2}{v^2}h^2W^\mu W_\mu + g_{W,a3}\frac{m_W^2}{3v^3}h^3W^\mu W_\mu \\
&\quad + g_{Z,a1}\frac{m_Z^2}{v}hZ^\mu Z_\mu + g_{Z,a2}\frac{m_Z^2}{2v^2}h^2Z^\mu Z_\mu + g_{Z,a3}\frac{m_Z^2}{6v^3}h^3Z^\mu Z_\mu + \cdots .
\end{aligned}
\tag{3.5}
$$

The SM is recovered when $g_{W,a1} = g_{W,a2} = g_{Z,a1} = g_{Z,a2} = 1$ and $g_{W,a3} = g_{Z,a3} = 0$. The measurements of $g_{W,a2}$ and $g_{Z,a2}$ involve double Higgs production, while the triple-Higgs production is required to determine $g_{W,a3}$ and $g_{Z,a3}$. It is challenge at current collider experiment. To study them, we need to consider a future high energy collider.

The tensor structure couplings of Higgs to vector boson are defined by

$$
\begin{aligned}
\mathcal{L}_{VVh} &= -\left(g_{W,b1}\frac{h}{v} + g_{W,b2}\frac{h^2}{2v^2} + g_{W,b3}\frac{h^3}{6v^3} + \cdots\right)W_{\mu\nu}^+ W^{-\,\mu\nu} \\
&\quad -\left(g_{A,b1}\frac{h}{2v} + g_{A,b2}\frac{h^2}{4v^2} + g_{A,b3}\frac{h^3}{12v^3} + \cdots\right)A_{\mu\nu}A^{\mu\nu} \\
&\quad -\left(g_{X,b1}\frac{h}{v} + g_{X,b2}\frac{h^2}{2v^2} + g_{X,b3}\frac{h^3}{6v^3} + \cdots\right)A_{\mu\nu}Z^{\mu\nu} \\
&\quad -\left(g_{Z,b1}\frac{h}{2v} + g_{Z,b2}\frac{h^2}{4v^2} + +g_{Z,b3}\frac{h^3}{12v^2} + \cdots\right)Z_{\mu\nu}Z^{\mu\nu}
\end{aligned}
\tag{3.6}
$$

This part is absent in the SM.

The Higgs self-interactions are described by

$$
\mathcal{L}_h = -\lambda_3\frac{m_h^2}{2v}h^3 - \frac{\kappa_5}{2v}h\partial^\mu h\partial_\mu h - \lambda_4\frac{m_h^2}{8v^2}h^4 - \frac{\kappa_6}{4v^2}h^2\partial^\mu h\partial_\mu h.
\tag{3.7}
$$

When $\lambda_3 = \lambda_4 = 1$ and $\kappa_5 = \kappa_6 = 0$, the SM is recovered. The measurement of these couplings is the most challenge part of the collider experiments. It is expected that the 14 TeV LHC can give a weak constraint on λ_3 [30], but cannot give any meaningful constraint on λ_4, κ_5 and κ_6.

The EFT Lagrangian defined by Eq. 3.2 can be translated to other EFT basis or NP models. Two examples are introduced in the following sections. In section 3.2, we introduce a basis of dimension-6 operators, which is called Strongly-Interacting Light Higgs (SILH) basis. The relations between the parameters in Eq. 3.2 and the SILH basis are also obtained. In section 3.3, we connect Eq. 3.2 to a NP models, namely Higgs inflation model.

3.2 The Strongly-Interacting Light Higgs (SILH)

Couplings power counting is not relied on the choice of basis, so we can related Eq. 3.2 to any basis. An example is Strongly-Interacting Light Higgs (SILH) basis. The SILH basis charaterized by two

parameters, the new physics scale m_ρ and a new coupling g_ρ. m_ρ and g_ρ has relation

$$m_\rho = g_\rho f, \tag{3.8}$$

where f is called σ-model scale [29]. The coupling g_ρ is required to be $g_{SM} \lesssim g_\rho \lesssim 4\pi$, where g_{SM} indicates any SM couplings. The upper bound on g_ρ ensures that perturbation theory is valid, since the loop expansion parameter $(g_\rho/4\pi)^2$ is less than unity.

With these definitions, the SILH effective Lagrangian is parameterized as

$$
\begin{aligned}
\mathcal{L}_{\text{SILH}} \;=\; & \frac{c_H}{2f^2}\partial^\mu\left(H^\dagger H\right)\partial_\mu\left(H^\dagger H\right) + \frac{c_T}{2f^2}\left(H^\dagger\overleftrightarrow{D^\mu}H\right)\left(H^\dagger\overleftrightarrow{D}_\mu H\right) - \frac{c_6\lambda}{f^2}\left(H^\dagger H\right)^3 \\
& + \left(\frac{c_y y_f}{f^2}H^\dagger H \bar{\psi}_{f,L}H\psi_{f,R} + \text{h.c.}\right) + \frac{c_g g_s^2}{16\pi^2 f^2}\frac{y_t^2}{g_\rho^2}H^\dagger H G_{\mu\nu}^a G^{a\mu\nu} \\
& + \frac{ic_W g_W}{2m_\rho^2}\left(H^\dagger\sigma^i\overleftrightarrow{D^\mu}H\right)(D^\nu W_{\mu\nu})^i + \frac{ic_B g_W'}{2m_\rho^2}\left(H^\dagger\overleftrightarrow{D^\mu}H\right)(\partial^\nu B_{\mu\nu}) \\
& + \frac{ic_{HW} g_W}{16\pi^2 f^2}(D^\mu H)^\dagger \sigma^i(D^\nu H)W_{\mu\nu}^i + \frac{ic_{HB} g_W'}{16\pi^2 f^2}(D^\mu H)^\dagger(D^\nu H)B_{\mu\nu} \\
& + \frac{c_\gamma g_W'^2}{16\pi^2 f^2}\frac{g_W^2}{g_\rho^2}H^\dagger H B_{\mu\nu}B^{\mu\nu}, \tag{3.9}
\end{aligned}
$$

where coefficients c_i are real numbers of order unity, and $H^\dagger\overleftrightarrow{D}_\mu H \equiv H^\dagger(D_\mu H)-(D_\mu H)^\dagger H$. Eq. 3.9 includes all independent CP-conserving gauge-invariant operators up to dimension six with all Higgs interactions. The other operators such as $H^\dagger H W_{\mu\nu}W^{\mu\nu}$ can be generated by integration by parts from the operators in Eq. 3.9. In the following text, we use $\mathcal{O}_i$ to represent the operator whose coefficient is proportional to c_i.

To find the relation between the SILH Lagrangian and Eq. 3.2, we have to expand the SILH Lagrangian in unitarity gauge and introduce the physical Higgs field. So the operator $\mathcal{O}_H$ induces the following term

$$\mathcal{O}_H = \frac{c_H}{2f^2}\partial^\mu\left(H^\dagger H\right)\partial_\mu\left(H^\dagger H\right) \;\rightarrow\; \frac{c_H}{2f^2}(v+h)^2\partial^\mu h\partial_\mu h. \tag{3.10}$$

In effect, the kinetic term of the Higgs field is modified to

$$\mathcal{L}_{kin}(h) \;=\; \frac{1}{2}\left(1+c_H\xi\right)\partial^\mu h\partial_\mu h, \tag{3.11}$$

where $\xi \equiv v^2/f^2$. This means that the Higgs field should be rescaled by $h \to \zeta_h h$, where $\zeta_h = (1+c_H\xi)^{-1/2}$. Eq. 3.10 induces two further derivative operators

$$\frac{c_H\xi}{v}\zeta_h^3 h\partial^\mu h\partial_\mu h, \tag{3.12}$$

$$\frac{c_H\xi}{2v^2}\zeta_h^4 h^2\partial^\mu h\partial_\mu h, \tag{3.13}$$

which gives the relation

$$\kappa_5 = -2c_H\xi(1 + c_H\xi)^{-3/2}, \tag{3.14}$$

$$\kappa_6 = -2c_H\xi(1 + c_H\xi)^{-2}, \tag{3.15}$$

To find the relations for λ_3 and λ_4, one have to consider the Higgs potential with additional c_6 term

$$\mathcal{V}\left(H^\dagger H\right) = -\mu^2 \left(H^\dagger H\right) + \lambda \left(H^\dagger H\right)^2 + \frac{c_6\lambda}{f^2}\left(H^\dagger H\right)^3 \tag{3.16}$$

In this case the VEV is given by

$$-\mu^2 + 2\lambda v^2 + \frac{3}{4}c_6\xi\lambda v^2 = 0, \tag{3.17}$$

and the corresponding Higgs mass is defined by

$$\frac{1}{2}m_h^2 = -\frac{1}{2}\mu^2 + \frac{3}{2}\lambda v^2 + \frac{15}{8}c_6\xi\lambda v^2. \tag{3.18}$$

After combining Eq. 3.17 and Eq. 3.18 and rescaling the Higgs field, we obtain a modified Higgs mass

$$m_h^2 = 2\lambda v^2 \left(1 + \frac{3}{2}c_6\xi\right)\zeta_h^2. \tag{3.19}$$

With these definitions of Higgs field and Higgs mass, we can write down the h^3 and h^4 terms:

$$\frac{m_h^2}{2v}\zeta\frac{1 + 5c_6\xi/2}{1 + 3c_6\xi/2}h^3, \tag{3.20}$$

$$\frac{m_h^2}{8v^2}\zeta^2\frac{1 + 15c_6\xi/2}{1 + 3c_6\xi/2}h^4. \tag{3.21}$$

So we obtain the relations for λ_3 and λ_4:

$$\lambda_3 = (1 + \frac{5}{2}c_6\xi)(1 + \frac{3}{2}c_6\xi)^{-1}(1 + c_H\xi)^{-1/2}, \tag{3.22}$$

$$\lambda_4 = (1 + \frac{15}{2}c_6\xi)(1 + \frac{3}{2}c_6\xi)^{-1}(1 + c_H\xi)^{-1}. \tag{3.23}$$

In Eq. 3.9, the subset operators $(\mathcal{O}_H, \mathcal{O}_6, \mathcal{O}_T, \mathcal{O}_y)$ are not independent. With the equation of motion (EOM), the operator $\mathcal{O}_T$ can be eliminated [31]. So the contributions of $\mathcal{O}_T$ is not considered in this context.

The Yukawa couplings are modified by the operator $\mathcal{O}_y$, which generates a term

$$\frac{c_y y_f}{f^2}H^\dagger H\bar{\psi}_{f,L}H\psi_{f,R} + \text{h.c.} \quad \rightarrow \quad \frac{c_y y_f}{2\sqrt{2}f^2}(v + h)^3\bar{\psi}_f\psi_f. \tag{3.24}$$

This term modifies the fermion mass to

$$m_f = \frac{y_f v}{\sqrt{2}}\left(1 - \frac{1}{2}c_y\xi\right). \tag{3.25}$$

With this definition, we can obtain the following operators

$$-\frac{m_f}{v}\zeta_h\frac{1 - 3c_y\xi/2}{1 - c_y\xi/2}h\bar{\psi}\psi, \tag{3.26}$$

$$\frac{m_f}{v^2}\zeta_h^2\frac{3c_y\xi/2}{1 - c_y\xi/2}hh\bar{\psi}\psi, \tag{3.27}$$

$$\frac{m_f}{v^3}\zeta_h^3\frac{c_y\xi/2}{1 - c_y\xi/2}hhh\bar{\psi}\psi. \tag{3.28}$$

If only the Yukawa couplings are considered, the a_1, a_2 and a_3 are

$$a_1 = (1 - \frac{3}{2}c_y\xi)(1 - \frac{1}{2}c_y\xi)^{-1}(1 + c_H\xi)^{-1/2}, \tag{3.29}$$

$$a_2 = -3c_y\xi(1 - \frac{1}{2}c_y\xi)^{-1}(1 + c_H\xi)^{-1}, \tag{3.30}$$

$$a_3 = -3c_y\xi(1 - \frac{1}{2}c_y\xi)^{-1}(1 + c_H\xi)^{-3/2}. \tag{3.31}$$

The relations to c_1 and c_2 is derivied from operator $\mathcal{O}_g$. After the ESWB, one can obtain

$$c_1 = c_2 = \frac{1}{4}c_g\xi\frac{y_t^2}{g_\rho^2}, \tag{3.32}$$

By using the equation of motion of $W_{\mu\nu}$ and $B_{\mu\nu}$ [28]

$$(D^\rho W_{\rho\mu})^i = \frac{g_W}{2}\left(H^\dagger i\sigma^i\overset{\leftrightarrow}{D}_\mu H + \bar{\psi}_l\gamma_\mu\sigma^i\psi_l + \bar{\psi}_q\gamma_\mu\sigma^i\psi_q\right), \tag{3.33}$$

$$\partial^\rho B_{\rho\mu} = g_W'Y H^\dagger i\overset{\leftrightarrow}{D}_\mu H + g_W'\sum_f y_\psi\bar{\psi}_f\gamma_\mu\psi_f, \tag{3.34}$$

one can obtain the expressions of the operators with coefficients c_W and c_B

$$\frac{ic_W g_W}{2m_\rho^2}\left(H^\dagger\sigma^i\overset{\leftrightarrow}{D^\mu}H\right)(D^\nu W_{\mu\nu})^i = \frac{ic_W}{m_\rho^2}\frac{g_W^2}{4}\left(H^\dagger\sigma^i\overset{\leftrightarrow}{D}^\mu H\right)\left(-H^\dagger i\sigma^i\overset{\leftrightarrow}{D}_\mu H\right) + ...$$

$$= \frac{c_W}{m_\rho^2}\frac{g_W^2}{4}\left[-\frac{g_W^2}{4\cos^2\theta}Z^\mu Z_\mu(v + h)^4 - \frac{g_W^2}{2}W^{+\mu}W_\mu^-(v + h)^4\right]$$

$$+... \tag{3.35}$$

$$\frac{ic_B g_W'}{2m_\rho^2}\left(H^\dagger\overset{\leftrightarrow}{D^\mu}H\right)(\partial^\nu B_{\mu\nu}) = \frac{ic_B}{m_\rho^2}\frac{g_W'^2}{4}\left(H^\dagger\overset{\leftrightarrow}{D^\mu}H\right)(-H^\dagger i\overset{\leftrightarrow}{D}_\mu H) + ...$$

$$= \frac{c_B}{m_\rho^2}\frac{g_W'^2}{4}\left[-\frac{g_W^2}{4\cos^2\theta}Z^\mu Z_\mu(v + h)^4\right] + ... \tag{3.36}$$

For the operators with coefficients c_{HW} and c_{HB}, two equations are introduced [32]:

$$
\begin{aligned}
2(D^\mu H)^\dagger \sigma^i (D^\nu H) W^i_{\mu\nu} &= H^\dagger \sigma^i \overleftrightarrow{D^\mu} H (D^\nu W^i_{\mu\nu}) - H^\dagger \sigma^i (D^\mu D^\nu H) W^i_{\mu\nu} \\
&\quad -(D^\nu D^\mu H)^\dagger \sigma^i H W^i_{\mu\nu} + \text{total derivative} \\
&= H^\dagger \sigma^i \overleftrightarrow{D^\mu} H (D^\nu W_{\mu\nu})^i + i\frac{g_W}{2} H^\dagger H W^{i\mu\nu} W^i_{\mu\nu} \\
&\quad + i\frac{g'_W}{2} H^\dagger \sigma^i H B^{\mu\nu} W^i_{\mu\nu} + \text{total derivative} \quad\quad (3.37) \\
2(D^\mu H)^\dagger (D^\nu H) B_{\mu\nu} &= H^\dagger \overleftrightarrow{D^\mu} H (\partial^\nu B_{\mu\nu}) - H^\dagger (D^\mu D^\nu H) B_{\mu\nu} \\
&\quad -(D^\nu D^\mu H)^\dagger H B_{\mu\nu} + \text{total derivative} \\
&= H^\dagger \overleftrightarrow{D^\mu} H \partial^\nu B_{\mu\nu} + i\frac{g_W}{2} H^\dagger \sigma^i H W^{i\mu\nu} B_{\mu\nu} \\
&\quad + i\frac{g'_W}{2} H^\dagger H B^{\mu\nu} B_{\mu\nu} + \text{total derivative} \quad\quad (3.38)
\end{aligned}
$$

They are obtained by using relations $D_\mu D_\nu = \frac{1}{2}[D_\mu, D_\nu] + \frac{1}{2}\{D_\mu, D_\nu\}$ and $[D_\mu, D_\nu] = -ig_W \frac{\sigma^i}{2} W^i_{\mu\nu} - ig'_W Y B_{\mu\nu}$. $\{D_\mu, D_\nu\}$ vanishes when it is being contracted with an anti-symmetric tensor $W^i_{\mu\nu}$ or $B_{\mu\nu}$. Expanding $\mathcal{O}_{HW}$ in unitarity gauge, we have

$$
\begin{aligned}
\frac{ic_{HW}g_W}{16\pi^2 f^2}(D^\mu H)^\dagger \sigma^i (D^\nu H) W^i_{\mu\nu} &= \frac{ic_{HW}g_W}{16\pi^2 f^2}\left[\frac{1}{2}\left(H^\dagger \sigma^i \overleftrightarrow{D^\mu} H\right)(D^\nu W_{\mu\nu})^i\right. \\
&\quad \left. -i\frac{g_W}{4} H^\dagger H W^i_{\mu\nu} W^{i\mu\nu} - i\frac{g'_W}{4} H^\dagger \sigma^i H W^i_{\mu\nu} B^{\mu\nu}\right] \\
&= \frac{c_{HW}g_W^2}{64\pi^2 f^2}\left[-\frac{m_Z^2}{v^2}Z^\mu Z_\mu (v+h)^4 - \frac{2m_W^2}{v^2}W^{+\mu}W^-_\mu (v+h)^4\right] \\
&\quad + \frac{c_{HW}g_W^2}{128\pi^2 f^2}(v+h)^2 W^i_{\mu\nu}W^{i\mu\nu} + \frac{c_{HW}g_W g'_W}{64\pi^2 f^2}H^\dagger \sigma^i H W^i_{\mu\nu}B^{\mu\nu} \\
&\quad + ... \quad\quad (3.39)
\end{aligned}
$$

Similarly, $\mathcal{O}_{HB}$ is expanded to

$$
\begin{aligned}
\frac{ic_{HB}g'_W}{16\pi^2 f^2}(D^\mu H)^\dagger (D^\nu H) B_{\mu\nu} &= \frac{ic_{HB}g'_W}{16\pi^2 f^2}\left[\frac{1}{2}\left(H^\dagger \overleftrightarrow{D^\mu} H\right)(\partial^\nu B_{\mu\nu})\right. \\
&\quad \left. -\frac{g'_W}{4}H^\dagger H B_{\mu\nu}B^{\mu\nu} - i\frac{g_W}{4}H^\dagger \sigma^i H W^i_{\mu\nu}B^{\mu\nu}\right] \\
&= \frac{c_{HB}g'^2_W}{64\pi^2 f^2}\left[-\frac{m_Z^2}{v^2}Z^\mu Z_\mu (v+h)^4\right] \\
&\quad + \frac{c_{HB}g'^2_W}{128\pi^2 f^2}(v+h)^2 B_{\mu\nu}B^{\mu\nu} + \frac{c_{HB}g_W g'_W}{64\pi^2 f^2}H^\dagger \sigma^i H W^i_{\mu\nu}B^{\mu\nu} \\
&\quad + ... \quad\quad (3.40)
\end{aligned}
$$

Equation 3.39, 3.40 and operator $\mathcal{O}_\gamma$ modify the kinetic terms of gauge bosons

$$
\begin{aligned}
\mathcal{L}_{kin}(W^\pm, Z, A) \;=\; & -\frac{1}{2}\left(1 + c_{HW}\frac{g_W^2 v^2}{32\pi^2 f^2}\right) W^{+\mu\nu}W^-_{\mu\nu} \\
& -\frac{1}{4}\left[1 + \frac{g_W^2 v^2}{32\pi^2 f^2}\left(c_{HW} + c_{HB}\tan^2\theta - 4c_\gamma\frac{g_W'^2}{g_\rho^2}\sin^2\theta\right)\right] Z_{\mu\nu}Z^{\mu\nu} \\
& -\frac{1}{4}\left[\frac{g_W g_W' v^2}{32\pi^2 f^2}(c_{HW} - c_{HB}) + \frac{g_W g_W' v^2}{16\pi^2 f^2}\left(4c_\gamma\frac{g_W^2}{g_\rho^2}\sin^2\theta\right)\right] Z_{\mu\nu}A^{\mu\nu} \\
& -\frac{1}{4}\left[1 - \frac{g_W^2 v^2}{32\pi^2 f^2}\left(4c_\gamma\frac{g_W'^2}{g_\rho^2}\cos^2\theta\right)\right] A_{\mu\nu}A^{\mu\nu} \qquad (3.41)
\end{aligned}
$$

This means the gauge fields are rescaled by

$$
W_\mu^\pm \;=\; \left(1 + c_{HW}\frac{g_W^2 v^2}{32\pi^2 f^2}\right)^{-\frac{1}{2}} W_\mu'^\pm = \zeta_W W_\mu'^\pm \qquad (3.42)
$$

$$
Z_\mu \;=\; \left[1 + \frac{g_W^2 v^2}{32\pi^2 f^2}\left(c_{HW} + c_{HB}\tan^2\theta - 4c_\gamma\frac{g_W'^2}{g_\rho^2}\sin^2\theta\right)\right]^{-\frac{1}{2}} Z_\mu' = \zeta_Z' Z_\mu' \quad (3.43)
$$

$$
A_\mu \;=\; \left[1 - \frac{g_W^2 v^2}{32\pi^2 f^2}\left(4c_\gamma\frac{g_W'^2}{g_\rho^2}\cos^2\theta\right)\right]^{-\frac{1}{2}} A_\mu' = \zeta_A A_\mu' \qquad (3.44)
$$

So the Eq. 3.41 is rewritten to

$$
\begin{aligned}
\mathcal{L}_{kin}(W'^\pm, Z', A') \;=\; & -\frac{1}{2}W'^{+\mu\nu}W'^-_{\mu\nu} - \frac{1}{4}Z'_{\mu\nu}Z'^{\mu\nu} - \frac{1}{4}A'_{\mu\nu}A'^{\mu\nu} \\
& -\frac{1}{4}y_{ZA}\zeta_A\zeta_Z' Z'_{\mu\nu}A'^{\mu\nu}, \qquad (3.45)
\end{aligned}
$$

where

$$
y_{ZA} \;=\; \left[\frac{g_W g_W' v^2}{32\pi^2 f^2}(c_{HW} - c_{HB}) + \frac{g_W g_W' v^2}{16\pi^2 f^2}\left(4c_\gamma\frac{g_W^2}{g_\rho^2}\sin^2\theta\right)\right]. \qquad (3.46)
$$

To eliminate the ZA mixing term, following linear shift is introduced

$$
A_\mu'' \;=\; A_\mu'' + \frac{y_{ZA}\zeta_A\zeta_Z'}{2} Z_\mu' \qquad (3.47)
$$

$$
Z_\mu'' \;=\; \sqrt{1 + \frac{y_{ZA}^2\zeta_A^2\zeta_Z'^2}{4}}\, Z_\mu' = \zeta_Z^{-1} Z_\mu. \qquad (3.48)
$$

This leads to

$$
A_\mu = \zeta_A A_\mu'' - \frac{y_{ZA}\zeta_A^2\zeta_Z'}{4} Z_\mu'' = \zeta_A A_\mu'' - \zeta_{AZ} Z_\mu'' \qquad (3.49)
$$

In the final result, all electroweak gauge bosons are canonically normalized, and the primes can be omitted from the redefined fields. The factors ζ_h, ζ_W, ζ_Z, ζ_Z', ζ_A and ζ_{AZ} are introduced for convenience.

Eq. 3.35 and Eq. 3.36 also modify the mass terms of gauge boson by

$$
\begin{aligned}
\mathcal{L}_{mass} &= \frac{g_W^2 v^2}{4} \left(1 - c_W \frac{g_W^2 v^2}{2m_\rho^2} - c_{HW} \frac{g_W^2 v^2}{32\pi^2 f^2} \right) \zeta_W^2 W^{+\mu} W_\mu^- \\
&+ \frac{g_W^2 v^2}{8\cos^2\theta} \left(1 - c_W \frac{g_W^2 v^2}{2m_\rho^2} - c_B \frac{g_W'^2 v^2}{2m_\rho^2} - c_{HW} \frac{g_W^2 v^2}{32\pi^2 f^2} - c_{HB} \frac{g_W'^2 v^2}{32\pi^2 f^2} \right) \zeta_Z^2 Z_\mu Z^\mu,
\end{aligned}
$$

(3.50)

It shifts the W mass and Z mass by

$$
m_W^2 = \frac{g_W^2 v^2}{4} \left(1 - c_W \frac{g_W^2 v^2}{2m_\rho^2} - c_{HW} \frac{g_W^2 v^2}{32\pi^2 f^2} \right) \zeta_W^2,
$$

(3.51)

$$
m_Z^2 = \frac{g_W^2 v^2}{4\cos^2\theta} \left(1 - c_W \frac{g_W^2 v^2}{2m_\rho^2} - c_B \frac{g_W'^2 v^2}{2m_\rho^2} - c_{HW} \frac{g_W^2 v^2}{32\pi^2 f^2} - c_{HB} \frac{g_W'^2 v^2}{32\pi^2 f^2} \right) \zeta_Z^2.
$$

(3.52)

After the redefinition of the gauge fields and their mass, the following relations are obtained

$$
g_{W,a1} = \left[1 - \left(c_W \frac{g_W^2 v^2}{m_\rho^2} + c_{HW} \frac{g_W^2 v^2}{16\pi^2 f^2} \right) \right] \zeta_h \zeta_W^2
$$

(3.53)

$$
g_{Z,a1} = \left[1 - \left(c_W \frac{g_W^2 v^2}{m_\rho^2} + c_B \frac{g_W'^2 v^2}{m_\rho^2} + c_{HW} \frac{g_W^2 v^2}{16\pi^2 f^2} + c_{HB} \frac{g_W'^2 v^2}{16\pi^2 f^2} \right) \right] \zeta_h \zeta_Z^2
$$

(3.54)

$$
g_{W,a2} = \left[1 - 3 \left(c_W \frac{g_W^2 v^2}{m_\rho^2} + c_{HW} \frac{g_W^2 v^2}{16\pi^2 f^2} \right) \right] \zeta_h^2 \zeta_W^2
$$

(3.55)

$$
g_{Z,a2} = \left[1 - 3 \left(c_W \frac{g_W^2 v^2}{m_\rho^2} + c_B \frac{g_W'^2 v^2}{m_\rho^2} + c_{HW} \frac{g_W^2 v^2}{16\pi^2 f^2} + c_{HB} \frac{g_W'^2 v^2}{16\pi^2 f^2} \right) \right] \zeta_h^2 \zeta_Z^2
$$

(3.56)

$$
g_{W,a3} = -6 \left(c_W \frac{g_W^2 v^2}{m_\rho^2} + c_{HW} \frac{g_W^2 v^2}{16\pi^2 f^2} \right) \zeta_h^3 \zeta_W^2,
$$

(3.57)

$$
g_{Z,a3} = -6 \left(c_W \frac{g_W^2 v^2}{m_\rho^2} + c_B \frac{g_W'^2 v^2}{m_\rho^2} + c_{HW} \frac{g_W^2 v^2}{16\pi^2 f^2} + c_{HB} \frac{g_W'^2}{16\pi^2 f^2} \right),
$$

(3.58)

$$
g_{W,b1} = c_{HW} \frac{g_W^2 v^2}{32\pi^2 f^2} \zeta_h \zeta_W^2,
$$

(3.59)

$$
g_{W,b2} = c_{HW} \frac{g_W^2 v^2}{32\pi^2 f^2} \zeta_h^2 \zeta_W^2,
$$

(3.60)

$$g_{Z,b1} = \frac{g_W^2 v^2}{32\pi^2 f^2}(c_{HW} + c_{HB}\tan^2\theta)\zeta_h\zeta_Z^2 - c_\gamma \frac{g_W^2 v^2}{8\pi^2 f^2}\frac{g_W'^2}{g_\rho^2}\cos^2\theta\zeta_h\zeta_{AZ}^2$$
$$- \frac{g_W g_W' v^2}{64\pi^2 f^2}\left[(c_{HW} - c_{HB}) + 8c_\gamma \frac{g_W^2}{g_\rho^2}\sin^2\theta\right]\zeta_h\zeta_{AZ}\zeta_Z \tag{3.61}$$

$$g_{Z,b2} = \frac{g_W^2 v^2}{32\pi^2 f^2}(c_{HW} + c_{HB}\tan^2\theta)\zeta_h^2\zeta_Z^2 - c_\gamma \frac{g_W^2 v^2}{8\pi^2 f^2}\frac{g_W'^2}{g_\rho^2}\cos^2\theta\zeta_h^2\zeta_{AZ}^2$$
$$- \frac{g_W g_W' v^2}{64\pi^2 f^2}\left[(c_{HW} - c_{HB}) + 8c_\gamma \frac{g_W^2}{g_\rho^2}\sin^2\theta\right]\zeta_h\zeta_{AZ}\zeta_Z \tag{3.62}$$

$$g_{A,b1} = -c_\gamma \frac{g_W^2 v^2}{8\pi^2 f^2}\frac{g_W'^2}{g_\rho^2}\cos^2\theta\zeta_h\zeta_A^2 \tag{3.63}$$

$$g_{A,b2} = -c_\gamma \frac{g_W^2 v^2}{8\pi^2 f^2}\frac{g_W'^2}{g_\rho^2}\cos^2\theta\zeta_h^2\zeta_A^2 \tag{3.64}$$

$$g_{X,b1} = \frac{gg'v^2}{64\pi^2 f^2}\left[(c_{HW} - c_{HB}) + 8c_\gamma \frac{g^2}{g_\rho^2}\sin^2\theta\right]\zeta_h\zeta_A\zeta_Z$$
$$+ c_\gamma \frac{g^2 v^2}{4\pi^2 f^2}\frac{g'^2}{g_\rho^2}\cos^2\theta\zeta_h\zeta_{AZ}^2 \tag{3.65}$$

$$g_{X,b2} = \frac{gg'v^2}{64\pi^2 f^2}\left[(c_{HW} - c_{HB}) + 8c_\gamma \frac{g^2}{g_\rho^2}\sin^2\theta\right]\zeta_h^2\zeta_A\zeta_Z$$
$$+ c_\gamma \frac{g^2 v^2}{4\pi^2 f^2}\frac{g'^2}{g_\rho^2}\cos^2\theta\zeta_h^2\zeta_{AZ}^2 \tag{3.66}$$

The relations between the parameters of Eq. 3.2 and SILH basis are collected in Table 3.1.

3.3 Higgs-inflation model

In this section, we relate Eq. 3.2 to a specific NP model, namely Higgs-inflation model. The source of this section is our paper [10].

Our universe is almost flat, homogeneous and isotropic, which is often considered as an argument that the SM is not complete. One solution of these issues is inflation [33, 34, 35, 36, 37]. The models of inflation always require an additional scalar, i.e., the inflaton. In many models, the inflaton has a mass around 10^{13} GeV, so it is difficult to discover it in current experiment. The idea of Higgs-inflation model [38, 39] is that Higgs can be treated as inflaton, and couples to gravity by

$$\mathcal{L}_{inflation} = \mathcal{L}_{SM} - \frac{M^2}{2}R - \alpha H^\dagger H R, \tag{3.67}$$

where M is some mass parameter, R is the gravitaional Ricci scalar, and α is a coupling constant.

	SILH
a_1	$(1 - \frac{3}{2}c_y\xi)(1 - \frac{1}{2}c_y\xi)^{-1}\zeta_h$
a_2	$-3c_y\xi(1 - \frac{1}{2}c_y\xi)^{-1}\zeta_h^2$
a_3	$-3c_y\xi(1 - \frac{1}{2}c_y\xi)^{-1}\zeta_h^3$
λ_3	$(1 + \frac{5}{2}c_6\xi)(1 + \frac{3}{2}c_6\xi)^{-1}\zeta_h$
λ_4	$(1 + \frac{15}{2}c_6\xi)(1 + \frac{3}{2}c_6\xi)^{-1}\zeta_h^2$
κ_5	$-2c_H\zeta_h^3$
κ_6	$-2c_H\xi\zeta_h^4$
$g_{W,a1}$	$\left[1 - \left(c_W\frac{g^2v^2}{m_\rho^2} + c_{HW}\frac{g^2v^2}{16\pi^2f^2}\right)\right]\zeta_h\zeta_W^2$
$g_{Z,a1}$	$\left[1 - \left(c_W\frac{g^2v^2}{m_\rho^2} + c_B\frac{g'^2v^2}{m_\rho^2} + c_{HW}\frac{g^2v^2}{16\pi^2f^2} + c_{HB}\frac{g'^2v^2}{16\pi^2f^2}\right)\right]\zeta_h\zeta_Z^2$
$g_{W,a2}$	$\left[1 - 3\left(c_W\frac{g^2v^2}{m_\rho^2} + c_{HW}\frac{g^2v^2}{16\pi^2f^2}\right)\right]\zeta_h^2\zeta_W^2$
$g_{Z,a2}$	$\left[1 - 3\left(c_W\frac{g^2v^2}{m_\rho^2} + c_B\frac{g'^2v^2}{m_\rho^2} + c_{HW}\frac{g^2v^2}{16\pi^2f^2} + c_{HB}\frac{g'^2v^2}{16\pi^2f^2}\right)\right]\zeta_h^2\zeta_Z^2$
$g_{W,a3}$	$-6\left(c_W\frac{g_W^2v^2}{m_\rho^2} + c_{HW}\frac{g_W^2v^2}{16\pi^2f^2}\right)\zeta_h^3\zeta_W^2$
$g_{Z,a3}$	$-6\left(c_W\frac{g_W^2v^2}{m_\rho^2} + c_B\frac{g_W'^2v^2}{m_\rho^2} + c_{HW}\frac{g_W^2v^2}{16\pi^2f^2} + c_{HB}\frac{g_W'^2v^2}{16\pi^2f^2}\right),$
$g_{W,b1}$	$c_{HW}\xi\frac{g_W^2}{32\pi^2}\zeta_h\zeta_W^2$
$g_{W,b2}$	$c_{HW}\xi\frac{g_W^2}{32\pi^2}\zeta_h^2\zeta_W^2$
$g_{Z,b1}$	$\frac{g_W^2}{32\pi^2}(c_{HW} + c_{HB}\tan^2\theta)\xi\zeta_h\zeta_Z^2 - c_\gamma\xi\frac{g_W^2}{8\pi^2}\frac{g_W'^2}{g_\rho^2}\cos^2\theta\zeta_h\zeta_{AZ}^2$ $-\frac{g_Wg_W'}{64\pi^2}\left[(c_{HW} - c_{HB}) + 8c_\gamma\frac{g^2}{g_\rho^2}\sin^2\theta\right]\xi\zeta_h\zeta_{AZ}\zeta_Z$
$g_{Z,b2}$	$\frac{g_W^2}{32\pi^2}(c_{HW} + c_{HB}\tan^2\theta)\xi\zeta_h^2\zeta_Z^2 - c_\gamma\xi\frac{g_W^2}{8\pi^2}\frac{g_W'^2}{g_\rho^2}\cos^2\theta\zeta_h^2\zeta_{AZ}^2$ $-\frac{g_Wg_W'}{64\pi^2}\left[(c_{HW} - c_{HB}) + 8c_\gamma\frac{g^2}{g_\rho^2}\sin^2\theta\right]\xi\zeta_h\zeta_{AZ}\zeta_Z$
$g_{A,b1}$	$-c_\gamma\xi\frac{g_W^2}{8\pi^2}\frac{g_W'^2}{g_\rho^2}\cos^2\theta\zeta_h\zeta_A^2$
$g_{A,b2}$	$-c_\gamma\xi\frac{g_W^2}{8\pi^2}\frac{g_W'^2}{g_\rho^2}\cos^2\theta\zeta_h^2\zeta_A^2$
$g_{X,b1}$	$\frac{g_Wg_W'}{64\pi^2}\left[(c_{HW} - c_{HB}) + 8c_\gamma\frac{g^2}{g_\rho^2}\sin^2\theta\right]\xi\zeta_h\zeta_A\zeta_Z$ $+c_\gamma\xi\frac{g_W^2}{4\pi^2}\frac{g_W'^2}{g_\rho^2}\cos^2\theta\zeta_h\zeta_{AZ}^2$
$g_{X,b2}$	$\frac{g_Wg_W'}{64\pi^2}\left[(c_{HW} - c_{HB}) + 8c_\gamma\frac{g^2}{g_\rho^2}\sin^2\theta\right]\xi\zeta_h^2\zeta_A\zeta_Z$ $+c_\gamma\xi\frac{g_W^2}{4\pi^2}\frac{g_W'^2}{g_\rho^2}\cos^2\theta\zeta_h^2\zeta_{AZ}^2$

Table 3.1: This table shows how the parameters in SILH are related to the parameters in Eq.3.2. The extra ζ_h^n, ζ_W^n, ζ_Z^n, ζ_A^n, ζ_{AZ}^n (which are defined in the Eq. 3.11 and Eq. 3.44~3.49) are the factors from the Higgs or gauge bosons wavefuction normalization. $\xi \equiv v^2/f^2$ is introduced for convenience.

Using the unitarity gauge, the Lagrangian in the Jordan frame can be written as

$$
S_{Jordan} = \int d^4x \sqrt{-g_W} \left\{ -\frac{M^2 + 2\alpha HH^\dagger}{2} R - \frac{1}{4} W^{a\mu\nu} W^a_{\mu\nu} - \frac{1}{4} B^{a\mu\nu} B^a_{\mu\nu} \right.
$$
$$
\left. + D_\mu H^\dagger D^\mu H - \lambda \left(HH^\dagger - \frac{v^2}{2} \right)^2 \right\} . \tag{3.68}
$$

The value of α can vary in the region $1 \ll \sqrt{\alpha} \ll 10^{17}$, corresponding to $M \simeq M_P$, where $M_P = 2.4 \times 10^{18}$ GeV is the Planck scale. To figure out the relations to the parameters of Eq. 3.2, it is necessary to transform the Lagrangian from the Jordan frame to the Einstein frame

$$
\hat{g}_{\mu\nu} = \Omega^2 g_{\mu\nu} , \quad \Omega^2 = 1 + \frac{2\alpha HH^\dagger}{M_P^2} . \tag{3.69}
$$

This transformation leads to a non-minimal kinetic term for the Higgs field. It is convenient to introduce a scalar field

$$
d\chi = \sqrt{\frac{\Omega^2 + 12\alpha^2 HH^\dagger / M_P^2}{\Omega^4}} dh. \tag{3.70}
$$

The action in the Einstein frame is

$$
S_E \supset \int d^4x \sqrt{-\hat{g}_W} \left\{ -\frac{M_P^2}{2} \hat{R} + \partial_\mu \chi \partial^\mu \chi - U(\chi) \right\} \tag{3.71}
$$

where $\hat{R}$ is calculated by using the metric $\hat{g}_{\mu\nu}$. Note that renormalization-group running effect is neglected. The effective Higgs potential is

$$
U(\chi) = \frac{1}{\Omega(\chi)^4} \frac{\lambda}{4} \left(h(\chi)^2 - \frac{v^2}{2} \right)^2 \tag{3.72}
$$

In the context of collider physics, for the small field values $h \simeq \chi$ and $\Omega^2 \simeq 1$, the potential for the field χ is close to that of the initial Higgs field. Inflation physics is described by the large-field behavior of the Higgs field. When the Higgs acts as an inflation, we have $h \gg M_P / \sqrt{\alpha}$ (or $\chi \gg \sqrt{6} M_P$). In this range, we can approximate

$$
h \simeq \frac{M_P}{\sqrt{\alpha}} \exp\left(\frac{\chi}{\sqrt{6} M_P} \right), \quad U(\chi) = \frac{\lambda M_P^4}{4\alpha^2} \left(1 + \exp\left(-\frac{2\chi}{\sqrt{6} M_P} \right) \right)^{-2} \tag{3.73}
$$

The potential is exponentially flat at large h, as appropriate for a model of inflation.

In a collider study, small h field value is the interesting part, and we can replace χ by h again. Pluging Eq. 3.70 into Eq. 3.71 and omitting higher-order terms, also re-instating the Higgs doublet

	Higgs-inflation
λ_3	$(1 + 6\alpha^2 v^2/M_p^2)^{-3/2}$
λ_4	$(1 + 6\alpha^2 v^2/M_p^2)^{-2}$
κ_5	$-12v^2\alpha^2/M_p^2(1 + 6\alpha^2 v^2/M_p^2)^{-3/2}$
κ_6	$-12v^2\alpha^2/M_p^2(1 + 6\alpha^2 v^2/M_p^2)^{-2}$
$g_{W,a1}$	$(1 + 6\alpha^2 v^2/M_p^2)^{-1/2}$
$g_{Z,a1}$	$(1 + 6\alpha^2 v^2/M_p^2)^{-1/2}$
$g_{W,a2}$	$(1 + 6\alpha^2 v^2/M_p^2)^{-1}$
$g_{Z,a2}$	$(1 + 6\alpha^2 v^2/M_p^2)^{-1}$

Table 3.2: This table shows how the parameters in Higgs-inflation model are related to the parameters in Eq.3.2. The factor $(1 + 6\alpha^2 v^2/M_p^2)^{-1/2}$ is induced by the Higgs wavefunction normalization. The other parameters in Eq.3.2 vanish.

notation H, we arrive at

$$
\begin{aligned}
S_E &= \int d^4x \sqrt{-\hat{g}_W}\Bigg\{ -\frac{M_P^2}{2}\hat{R} + \text{gauge interactions} + \frac{D_\mu H D^\mu H}{\Omega^2} + \frac{12\alpha^2}{M_p^2}\frac{H^2 \partial_\mu H \partial^\mu H}{\Omega^4} \\
&\quad -\frac{1}{\Omega^2}\lambda\left(H^2 - \frac{v^2}{2}\right)^2 + \frac{2H^2}{\Omega^2}(\frac{M_W^2}{v^2}W^\mu W_\mu + \frac{M_Z^2}{v^2}Z^\mu Z_\mu)\Bigg\}.
\end{aligned}
\tag{3.74}
$$

So the Higgs-inflation model predicts deviations of Higgs-gauge boson couplings and Higgs self-couplings, and can be related to the parameters in $\mathcal{L}_{Vh}$ and $\mathcal{L}_h$. The relations of parameters are list in Table 3.2. The gauge interactions terms are not relevant to Eq. 3.2. The details of these terms can be found in Ref. [40].

Chapter 4

Multi-Higgs production via gluon-gluon fusion mode

At a hadron collider, the dominant SM process of multi-Higgs production is gluon-gluon fusion (ggF) via a heavy top quark loop. Example feynman diagrams for triple-Higgs production are shown in Fig. 4.1. The feasibility of double-Higgs production at the LHC has become a hot topic [41, 42, 43, 44], since it is an interesting process to probe the Higgs triple self-coupling. Multiple groups have considered a number of decay channels of the Higgs pair, including $WWWW$ [45, 46], $b\bar{b}\gamma\gamma$ [31, 47, 48, 49, 50, 51], $b\bar{b}WW$ [52], $b\bar{b}\tau\tau$ [53, 54, 55], $b\bar{b}\mu\mu$ [47], $WW\gamma\gamma$ [56], and $b\bar{b}b\bar{b}$ [53, 57, 58]. Beyond the LHC, at a future 100 TeV hadron collider, the double-Higgs production rate is enhance significantly [49, 59, 60, 61, 62, 63, 64, 65], allowing for a more accurate measurement of the Higgs triple self-coupling and Higgs potential.

The measurement of quartic Higgs self-coupling involves triple Higgs production. It is very challenging because the cross section of $gg \to hhh$ is only $\mathcal{O}(0.01)$ fb [66, 67] at 14 TeV LHC. The authors of Ref. [68] have considered $pp \to Zhhh$ and $pp \to Whhh$, but the cross section is also tiny. At a 100 TeV hadron collider, triple-Higgs production via ggF is observable in principle [69, 70, 71, 72, 9, 73]. The cross section of $gg \to hhh$ at a 100 TeV hadron collider is estimated around 5 fb if NLO QCD correction is included [69]. Various decay channels of triple Higgs have been investigated, such as $hhh \to b\bar{b}b\bar{b}\gamma\gamma$ [70, 71], $hhh \to b\bar{b}b\bar{b}\tau\tau$ [72, 74] and $hhh \to b\bar{b}WW^*WW^*$ [9]. It is shown that the discovery of this process is strongly depended on the performance of the detector and analysis.

This chapter introduces our work [9]. In this work, we explore the potential for the discovery of the triple-Higgs signal in the $2b2l^{\pm}4j + \not{E}$ decay channel at a 100 TeV hadron collider. We consider both the SM and generic NP contributions, described by the effective Lagrangian, Eq. 3.2. In the SM, we perform a collider simulation. Although the parton-level results are encouraging, the detector-level results indicate that this decay channel will be really challenging. The contributions from effective operators can largely increase the cross section and/or modify the kinematics of the Higgs bosons in the final state. Taking into account the projected constraints from single and double Higgs-boson

production, we propose benchmark points in the NP models for the measurement of the triple-Higgs boson final state at future collider.

4.1 Analysis of the $hhh \to 2b2l^{\pm}4j + \not{E}$ decay channel in the SM

The dominant subprocess of $pp \to hhh$ signal is gluon-gluon fusion, $gg \to hhh$. This process involves one-loop diagrams. The example Feynman diagrams of this process is plotted in Fig. 4.1. To perform the Monte-Carlo (MC) simulation, we compute production matrix element at LO with Mad-Loop/aMC@NLO [75]. The parton distribution functions is taken from CTEQ6l1 [76]. For phase-space evaluation and exclusive event generation, we interface the matrix element with VBFNLO [77, 78, 79]. We are interested in the $hhh \to 2b2l^{\pm}4j + \not{E}$ decay channel, where one Higgs boson decays into a $b\bar{b}$ pair while the two other Higgses decay into WW^*. The semi-virtual W pairs can subsequently decay semileptonically, $h \to WW^* \to l\nu jj$.
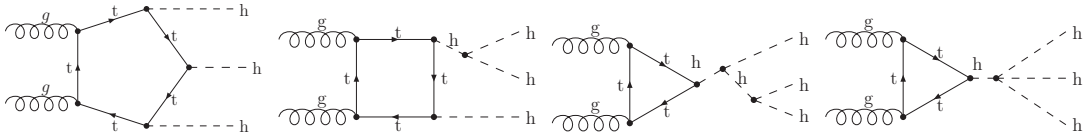
Figure 4.1: The example Feynman diagrams of the process $gg \to hhh$ in the SM.

Background event samples are generated by MadGraph5 [8, 80]. Since we require a $b\bar{b}$ pair, the dominant background is caused by top-quark pairs associated with Higgs or gauge bosons, namely $pp \to h(WW^*)t\bar{t}$ and $pp \to t\bar{t}W^-W^+$. Both classes of processes can lead to the same final state as the signal. To veto further background from Z bosons, we restrict the analysis to same-sign leptons in the final state, l^+l^+ or l^-l^-.

We ignore the background from h+jets, hh+jets and $W^{\pm}W^{\pm}$+jets, because the cross sections of these processes are negligible compared to the $h(WW^*)t\bar{t}$ background. Furthermore, the total cross section of the background $b\bar{b}W^-W^+W^-W^+$ is essentially exhausted by the resonant contribution $t\bar{t}W^-W^+$. Therefore, we approximate the former process by the latter with subsequent top-quark decay, which considerably simplifies the calculation.

Cross sections of signal and backgrounds at 100 TeV are listed in Table 4.1. For the signal, the K-factor of 2.0 is taken from Ref. [70]. For the $h(WW^*)t\bar{t}$ background, we use $K = 1.2$ [81], while the K-factor for $t\bar{t}W^-W^+$ at 100 TeV is chosen as 1.3, which is used in Ref. [63].

If NP contributes to Higgs sector, the process $pp \to hhjj$ can be the background in the SM and NP models. We have three comments on this background:

- In the SM, the $hhjj$ final state receives contributions from the ggF and the VBF, while the former is dominant. Currently, the cross section of loop-induced processes with 2 jets can be calculated by interfacing GoSam [82] or OpenLoops [83] to Madgraph5 or Herwig7 [84]. We use Madgraph5 to compute the cross section of $gg \to hhjj$ at a 100 TeV collider. After

Process	$\sigma \times BR$ (ab)	K-factor	Expected number of events
Signal	10.71	2.0	642
$h(WW^*)t\bar{t}$	2.55×10^5	1.2	9.18×10^6
$t\bar{t}W^-W^+$	3.68×10^4	1.3	1.55×10^6

Table 4.1: Cross sections of signal and background for the $2b2l^{\pm}4j + \not{E}$ final state in the SM. The expected number of events corresponds to 30 ab^{-1} integrated luminosity.

imposing the MLM matching[85] and applying cuts $P_t(j) > 20$ GeV and $\eta(j) < 5$, we obtain an inclusive cross section 620 fb, which is around 128 times larger than the cross section $\sigma(hhh)$ of the signal process. Meanwhile, by using Madgraph5, we find that the cross section of VBF with $\sqrt{s} = 100$ TeV is 34 fb.

- It is known that when the b tagging efficiency is taken as 0.7, the rejection rate of light jets can reach 0.1% or so. Since we required one(two) tagged b jets in our preselection cuts, therefore the background $gg \to hh + 2$jets is suppressed by a factor 10^{-3} (10^{-6}) or so. After imposing b taggings and the decay branching fraction of $h \to b\bar{b}$, we find that the signal cross section $b\bar{b}hh$ is around $0.52(0.29)\,\sigma(hhh)$, while the cross section of background $hh + 2$jets is $0.13(0.13 \times 10^{-3}) \times \sigma(hhh)$ or so. Obviously, when $n_b \geq 2$ is imposed, it is safe to neglect this type of background in the SM.

- In the NP models that we will consider in section 4.2.4, the background process $pp \to hhjj$ can obtain extra contributions from higher dimensional operators. When the cross section is $2 \sim 5$ magnitude orders smaller than the signal process, we can neglect it safely. In the cases when such a background is greatly enhanced or in the cases the signal process $gg \to hhh$ is greatly suppressed by the higher dimensional operators to such a degree that the cross sections of them are comparable, the background of $hhjj$ should be included in the analysis.

Table 4.1 shows that there are 642 signal events in this decay channel for 30 ab^{-1} integrated luminosity, while there are $\sim 10^7$ background events. It is a challenge to observe the triple-Higgs signal in the SM through this channel. The following subsections introduce the selection methods for further suppressing the background and increasing the significance.

4.1.1 Parton-level analysis

The decay of Higgs bosons is performed by the DECAY package provided by MadGraph5. The parton shower effects are neglected in this subsection, and will be discussed in subsection 4.1.2. The transverse momentum (P_t) distributions of the visible particles (b quarks, jets, and leptons) and missing transverse energy (MET) are plotted in Fig. 4.2. In this figure, the objects are sorted by P_t. On the one hand, one can expect that the b quarks are harder than the light quarks, since they are

decayed from a Higgs boson directly. On the other hand, the decay chain $h \to WW^* \to jjl\nu$ leads to soft leptons and light jets, especially when they are coming from the off-shell W bosons.

In Fig. 4.2(b) and Fig. 4.2(c), one can observe that the P_t distributions of the softest leptons and jets have peaks around 10 GeV, which might make it challenging to reconstruct these objects successfully without a detector with high performance. The signal contains only two neutrinos, so the MET should not be too large. We observe that MET peaks around 50 GeV in Fig. 4.2(d).
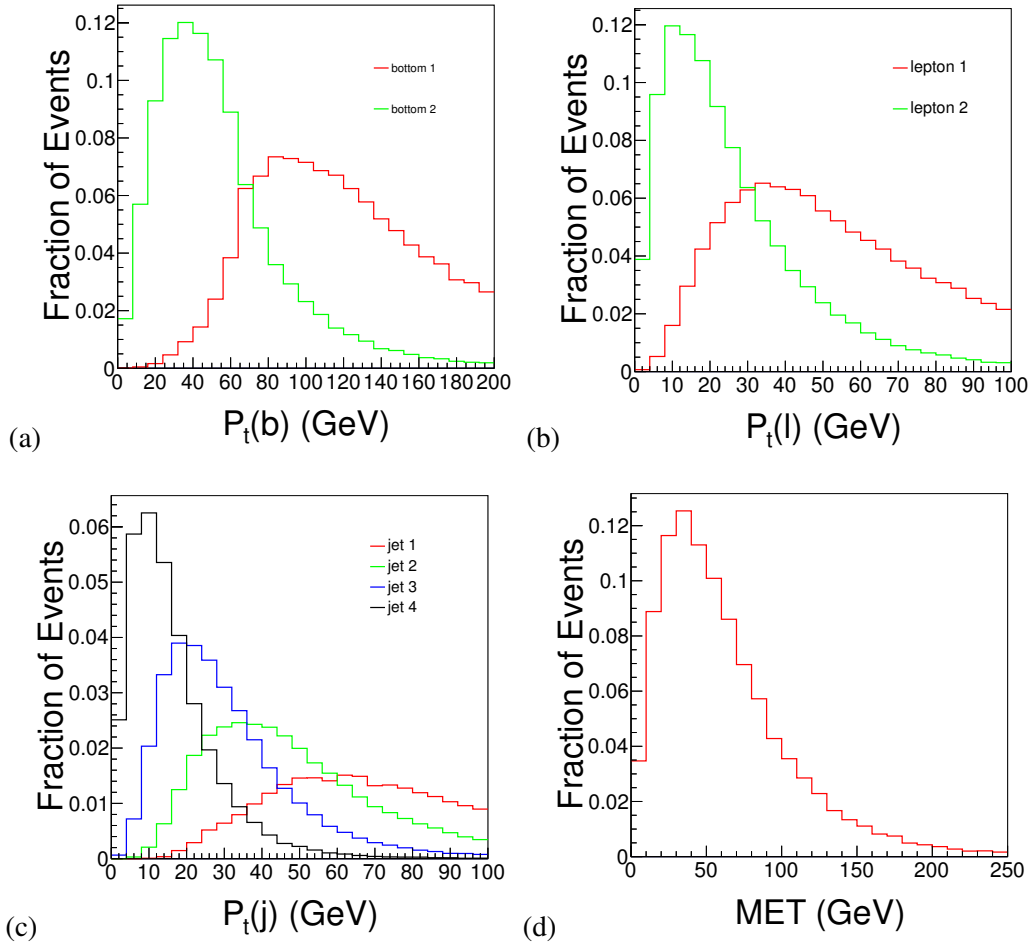
Figure 4.2: Distributions of (a) the transverse momentum of b quarks, (b) the transverse momentum of leptons, (c) the transverse momentum of light quarks (labeled by j), and (d) missing transverse energy in the signal events.

There are two unobservable neutrinos in the final state, and their mothers can be either on-shell or off-shell W bosons. It is not convenient to fully reconstruct the Higgs bosons. So we consider a method of partial reconstruction. In order to extract information of Higgs bosons, it is crucial to combine the decay products correctly. To simplify the problem, we assume that two b quarks are tagged correctly, so only the light quarks can be reassigned and the ambiguity can be reduced to 6-fold.

Methods	The percentage of correctness
$\min[\Delta R_1(l, W_{jj}) + \Delta R_2(l, W_{jj})]$	47.0%
$\min(m_{h1}^{\text{vis}} + m_{h2}^{\text{vis}})$	61.2%
$\min(mT2)$	66.8%
$\min|mT2 - m_h|$	99.98%

Table 4.2: Strategies for determining the correct combinations of (l, j, j) and their percentages of correctness.

To find the correct combination of the visible particles in the final state, we examine the following four strategies at parton level:

1. The decay chain $h \to WW^* \to jjl\nu$ suggests that the lepton and the hadronically decayed W boson should have a small angular separation $\Delta R(l, W_{jj})$. Since there are two Higgs bosons with this decay chain, the sum of $\Delta R_1(l, W_{jj}) + \Delta R_2(l, W_{jj})$ should be minimal. The first strategy is choosing the combination with a minimal of this observable.

2. The semileptonic Higgs invariant masses can be computed from the visible particles. These observables are labeled as $m_{h1}^{\text{vis}}(l, jj)$ and $m_{h2}^{\text{vis}}(l, jj)$. The second strategy is choosing the combination which minimizes their sum.

3. We compute the $mT2$ observable that has been defined in Refs. [86, 87, 88, 89, 90], from the visible particles that originate from semileptonic Higgs decay. The observable can set an upper bound on the Higgs mass, so the third strategy is choosing the combination with the minimal of $mT2$.

4. The forth strategy is choosing the combination with the minimal of $|mT2 - m_h|$, because it is expected that $mT2$ have a value close to the Higgs mass m_h.

These strategies and their associated percentages of correct assignment in the event samples are listed in Table 4.2. In a parton-level analysis, the forth strategy that relies on the quantity $|mT2 - m_h|$ has the best performance, approaching 100% probability for correct particle assignment in the reconstruction.

4.1.2   Detector-level analysis

To obtain the hadronic event samples, we use the parton-shower and hadronization modules of Pythia 6.4 [91]. The jet clustering is performed by the package FASTJET [92] with the anti-k_t algorithm [93]. The cone parameter is set to $R = 0.5$. To veto the large number of soft jets from initial-state radiation, only jets with $P_t > 20$ GeV are accepted.

The number of jets (n_j) and the P_t distributions of the leading 6 jets are shown in Fig. 4.3. Both signal and background produce six quarks at parton level, so the peaks of n_j are around 6 in Fig. 5.2(a).

In Fig. 5.2(b), we observe that the 1st to 4th jet has similar distributions as at parton level, but the 5th and 6th jet P_t distributions have different shapes with respect to their parton-level counterparts.

The reasons of this result are simple. On one hand, the P_t of the softest quark in Fig. 4.2(c) is only around 10 GeV, but most of the low-P_t jets are vetoed by the $P_t > 20$ GeV cut. On the other hand, jets from initial-state radiation can easily be as hard as 20 GeV at a 100 TeV collider. So the 5th and 6th jet are more likely produced by the initial-state radiation rather than the decay of Higgs boson. Fig. 4.3 illustrates the challenge of reconstructing the soft jets generated by the multi-Higgs signal.

(a) (b)
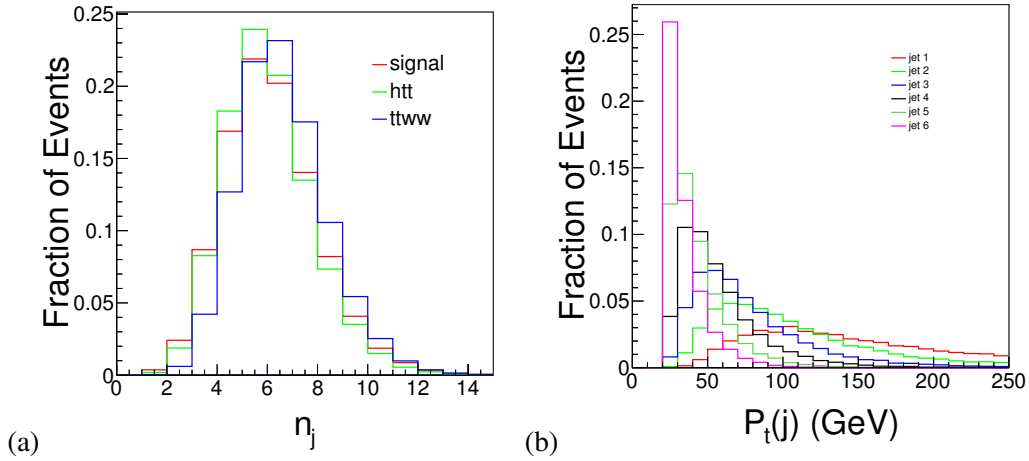
Figure 4.3: Distributions of (a) the number of jets and (b) P_t of the six leading jets of the signal.

Another important problem is the reconstruction of leptons. We assume that a future detector can reconstruct leptons with high efficiency (95% for $P_t > 5$ GeV), so it should be able to find the soft lepton as shown in Fig. 4.2(b). But a detector also need to isolate the leptons from other objects. To find a suitable isolation condition, we investigate the angular separations between two leptons ($\Delta R(l, l)$) and between a lepton and a jet ($\Delta R(l, j)$), respectively. The distributions of the minimums of these observables are displayed in Fig. 4.4. On one hand, $\min \Delta R(l, l)$ tends to have a large value, and only 10% of the events have $\min \Delta R(l, l) < 0.5$. On the other hand, almost 50% of the events have $\min \Delta R(l, j) < 0.2$. This makes it difficult to isolate the leptons from jets.

To study the detector effects, we input the event samples to the package DELPHES [94, 95] to perform a detector simulation. The setup of DELPHES is similar as in Ref. [71], with the following modifications:

1. The b-tagging efficiency is assumed to be a constant $\epsilon_b = 0.7$, and mistagging rates are 0.1 and 0.001 for charm and light jets, respectively. The pseudorapidity for b (c, jet) is required to be $\eta < 5.0$, respectively.

2. As described above, the jets are clustered by FASTJET with a cut $P_t(j) > 20$ GeV.

3. The efficiency of lepton indentification is assumed to be 95% when $P_t(l) > 5$ GeV and $\eta(l) < 5.0$.

(a)   min ΔR(l,l)

(b)   min ΔR(l,j)
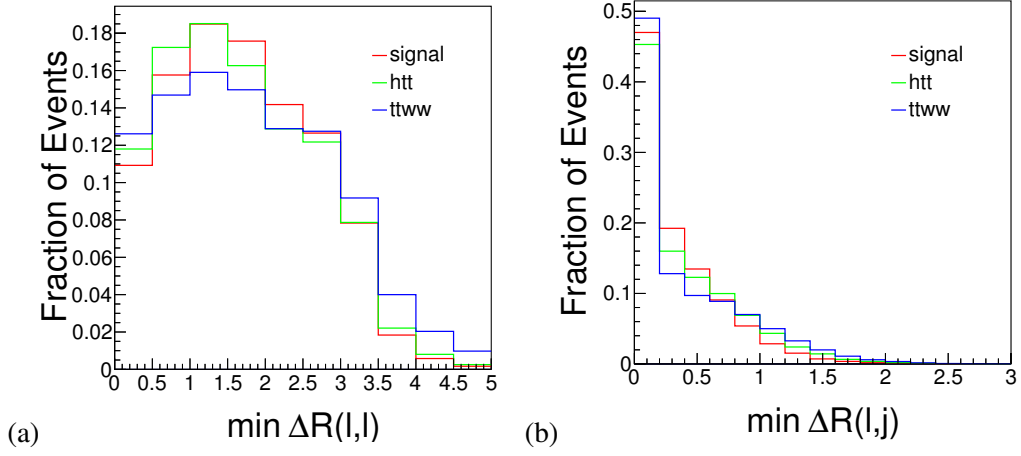
Figure 4.4: Distributions of (a) the minimum angular separation between two leptons, and (b) the minimum angular separation between lepton and jet.

4. Isolated leptons are defined by Ref. [95]

$$
I(l) = \frac{\sum_{i \neq l}^{\Delta R < R, P_t(i) > P_t^{min}} P_t(i)}{P_t(l)},
\tag{4.1}
$$

where l labels a lepton. The sum in the numerator runs over particles with transverse momenta above $P_t^{min} = 0.1$ GeV within a cone with radius $R = 0.5$, except for l. A lepton is said to be isolated if $I(l) < 0.1$.

n_b

n_l
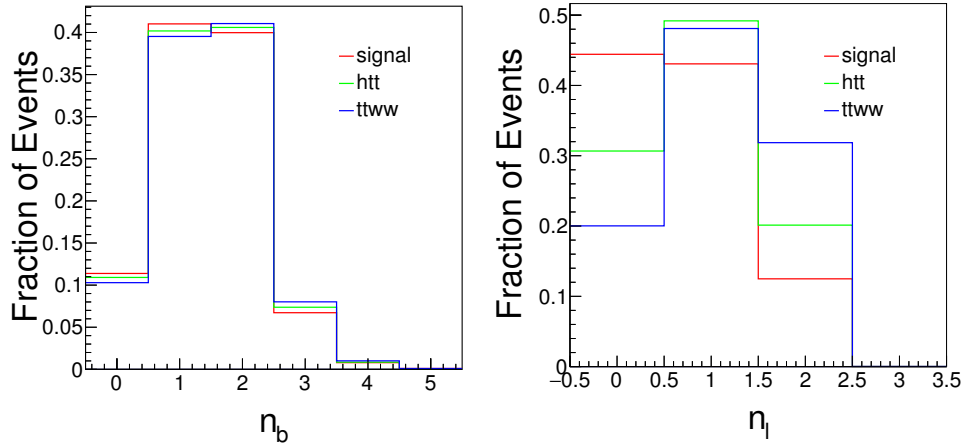
Figure 4.5: Distributions of (a) the number of b-tagging jets and (b) the number of leptons.

Fig. 4.5 displays the distributions of number of b jets and isolated leptons after detector simulation. Both signal and backgrounds include two b jets, which leads to the similarity of the shapes in Fig. 4.5(a). In Fig. 4.5(b), only 10% of the signal events are found to include two leptons, while

20% of $ht\bar{t}$ events and 30% of $t\bar{t}W^+W^-$ events include 2 leptons. It is shown that the small value of $\min \Delta R(l,j)$ makes it difficult to isolate lepton from other objects.
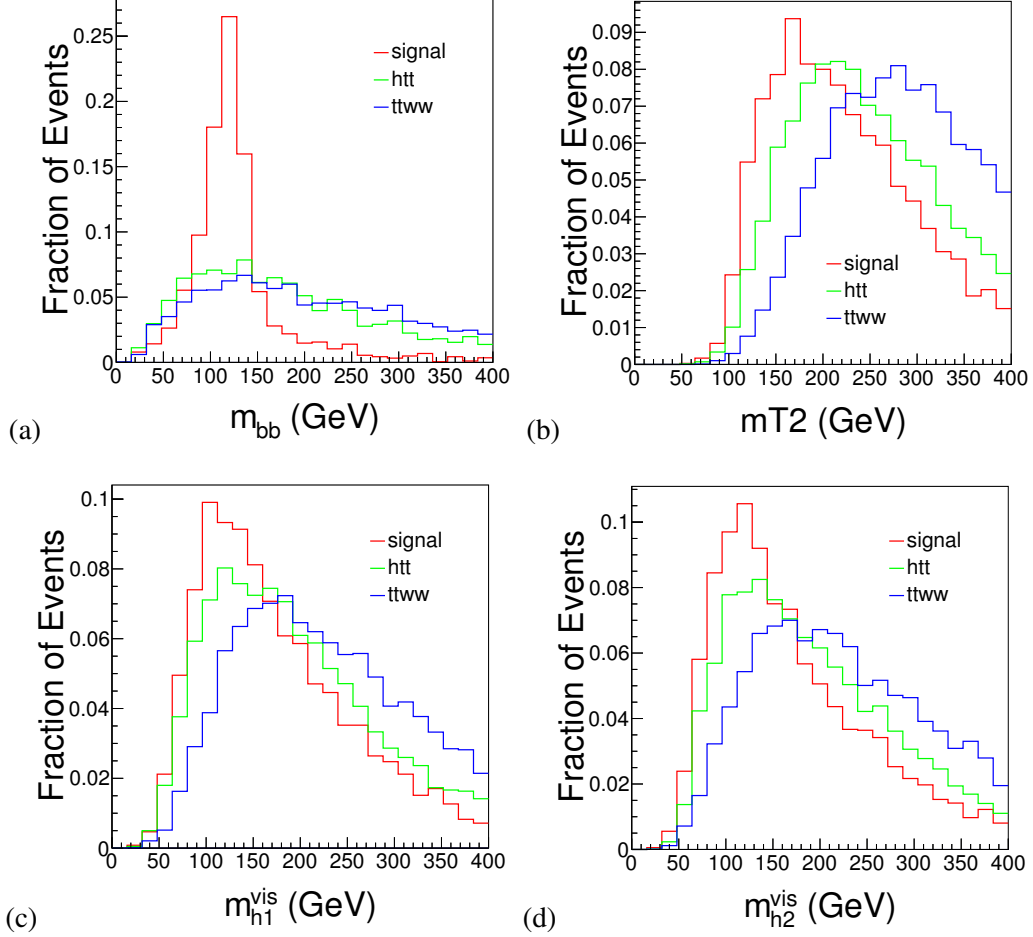
Figure 4.6: Distributions of important observables at detector level: (a) the invariant mass of $b\bar{b}$, (b) the $mT2$ observable, and (c) & (d) the Higgs masses as reconstructed from visible particles.

To suppress the huge background events, we first apply three preselection cuts:

1. The number of b jets is required to be $n_b \geq 1$.

2. To veto background from a Z boson, we require two same-sign leptons, as discussed above, even though it also removes triple-Higgs signal events which decay to opposite-sign leptons.

3. The number of light jets is required to be $n_j \geq 4$.

And then we consider three observables: (1) the invariant mass of a b-jet pair (m_{bb}), (2) the $mT2$ variable, and (3) the invariant masses (m_{h1}^{vis} and m_{h2}^{vis}) reconstructed from the visible objects. The distributions of these observables are displayed in Fig. 4.6. In Fig. 4.6(a), the signal exhibits the expected m_{bb} peak around the Higgs mass, while the background is non-resonant. For the observables

	Signal	$h(WW^*)t\bar{t}$	$t\bar{t}W^-W^+$
Preselection	24	9.73×10^5	2.59×10^6
$mT2 < 484$ GeV	23	9.40×10^5	2.35×10^5
$|m_{bb} - m_h| < 58$ GeV	21	6.73×10^5	1.42×10^5
$m_h^{\text{vis}} < 482$ GeV	21	6.72×10^5	1.42×10^5
S/B	2.56×10^{-5}		
$S/\sqrt{S+B}$	0.0231		

Table 4.3: Efficiencies of cuts as described in the text, for a total integrated luminosity of 30 ab^{-1}..

$mT2$, m_{h1}^{vis}, and m_{h2}^{vis}, they should have a upper bound at the Higgs mass in the SM signal samples. However, Figs. 4.6(b)–4.6(d) show that they tend to have larger values. As discussed above, the reconstruction of the softest jet together with missing lepton isolation lead to this effect.

Nevertheless, we can try to suppress background by applying cuts on the above observables. The efficiencies of each cut are listed in Table 4.3. In the cut-based method, the significance of the signal finally reaches to 0.02. Obviously, it is much worse than that could be expected from the parton-level calculation. In the SM, a discovery of signals of triple-Higgs production through this channel will be extremely challenging.

4.2 Triple-Higgs production in the EFT framework

The observation of triple-Higgs production is challenging in the SM, but the NP contribution may enhance the production rate of this process. In this section, we discuss the measurements of the parameters in Eq. 3.2 at a 100 TeV hadron collider.

In the SM, the process $gg \to hhh$ involves the Higgs-top coupling, Higgs triple and quartic self-coupling. Higgs-gluon couplings can appear either from the underlying theory directly or from loop-diagram renormalization via operator mixing. So the parameters in $\mathcal{L}_t$, $\mathcal{L}_{ggh}$ and $\mathcal{L}_h$ can contribute to this process.

Some parameters in Eq. 3.2 also affect other processes such as $pp \to ht\bar{t}$ and $gg \to hh$. These processes are more easily accessible at 100 TeV hadron collider, and they can give some constraints to the parameters. However, the quartic self-coupling of Higgs bosons is only accessible in triple-Higgs production. Any actual measurement of the EFT parameters involves a fitting procedure that takes all available information into account. An independent measurement of triple-Higgs production can provide essential information for searching NP.
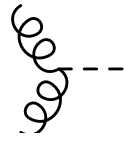
If the triple-Higgs final state become observable, the EFT parameters should modify the amplitudes drastically, at least in the high-energy or high-P_t regions of the phase space. In this case, the unitarity of the amplitudes and the consistency of the EFT may become a problem. For the ggF process, we have to consider the scattering amplitudes of top quarks to multiple Higgs bosons. Though

the effects of strong rescattering have been widely studied in the linear EFT context for vector-boson scattering [96, 97], results for processes involving top quarks and Higgs bosons are absent in the literatures. For the current study, we take the EFT unmodified over the complete parameter space and defer a study of unitarity to future work.
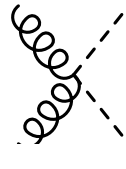
4.2.1   Calculation

This subsection describes the method for the calculation of ggF process with the new parameters introduced by the effective Lagrangian, Eq. 3.2. We first generate a UFO model file [98] with the effective Lagrangian Eq. 3.2. And then we interface the model file with the package Madgraph5 [8, 80] for calculating the loop-induced matrix elements, evaluating phase space and generating event samples. The program reduces the one-loop Feynman integrals to scalar integrals in four dimensions, by using the OPP method [99]. The difference between the D-dimensional and 4-dimensional expressions that arises in the calculation generates additional rational terms [100]. They are identified as R1 terms associated with D-dimensional denominators, and R2 terms associated with D-dimensional numerators. All R1 terms can be generated automatically as a byproduct of the reduction method, while the R2 terms must be calculated manually [101]. We have performed this calculation by using the method of Ref. [102], and supply the results as effective tree-level vertices in the UFO model file.
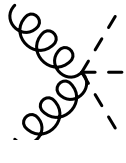
In particular, we obtain the R2 terms that amount to contact interactions of a pair of gluons with one to three Higgs bosons:

$$= -i\frac{g_s^2 m_t^2 \delta^{ab} g_{\mu_1\mu_2}}{8\pi^2 v} a_1 \tag{4.2}$$

$$= -i\frac{g_s^2 m_t^2 \delta^{ab} g_{\mu_1\mu_2}}{8\pi^2 v^2} (a_1^2 + a_2) \tag{4.3}$$

$$= -i\frac{g_s^2 m_t^2 \delta^{ab} g_{\mu_1\mu_2}}{8\pi^2 v^3} (a_3 + 3a_1 a_2) \tag{4.4}$$

The coefficients depend on the EFT parameters a_1, a_2, and a_3. Since these terms are required to restore the exact QCD symmetries in the calculated amplitude, by themselves they manifestly violate gauge invariance. We have verified that the complete renormalized one-loop result does respect gauge invariance, a convenient cross-check of the calculation.

Besides these loop-induced contributions, ggF process also receives contribution from contact interactions between gluons and Higgs bosons that do not exist in the SM. As mentioned above,

the inclusion of such contact interactions is required by loop-induced operator mixing in the EFT, but could also originate from independent BSM contributions. Technically, we implement them as independent R2 terms, so that Madgraph5 will sum them together with loop-induced contribution.

4.2.2 Cross sections of $gg \to hhh$ and Kinematics

The amplitudes of the process $gg \to hhh$ are constructed from the Feynman diagrams in Fig. 4.5. For illustrating the method, we consider the terms that depend on a_1, κ_5, κ_6, λ_3 and λ_4. Complete numerical results are given in Appendix A.

$$\propto a_1^3, \qquad \propto a_1^2 \lambda_3 / a_1^2 \kappa_5,$$

$$\propto a_1 \lambda_3^2 / a_1 \lambda_3 \kappa_5 / a_1 \kappa_5^2, \qquad \propto a_1 \lambda_4 / a_1 \kappa_6. \tag{4.5}$$

The corresponding matrix element can be expanded to

$$
\begin{aligned}
M(gg \to hhh) \propto \quad & f_1 a_1^3 + f_2 a_1^2 \lambda_3 + f_3 a_1^2 \kappa_5 + f_4 a_1 \lambda_3^2 + f_5 a_1 \lambda_3 \kappa_5 \\
+ \quad & f_6 a_1 \kappa_5^2 + f_7 a_1 \lambda_4 + f_8 a_1 \kappa_6 \,,
\end{aligned}
\tag{4.6}
$$

where f_i are form factors, which depend on the external momenta, partly in form of Higgs-boson propagators. After squaring the matrix element and integrating over the phase space, the total cross section can be parameterized as

$$
\begin{aligned}
\sigma(pp \to hhh) = \ & t_1 a_1^6 + t_2 a_1^5 \lambda_3 + t_3 a_1^5 \kappa_5 + t_4 a_1^4 \lambda_3^2 + t_5 a_1^4 \lambda_3 \kappa_5 \\
& + t_6 a_1^4 \kappa_5^2 + t_7 a_1^4 \lambda_4 + t_8 a_1^4 \kappa_6 + t_9 a_1^3 \lambda_3^3 + t_{10} a_1^3 \lambda_3^2 \kappa_5 \\
& + t_{11} a_1^3 \lambda_3 \kappa_5^2 + t_{12} a_1^3 \kappa_5^3 + t_{13} a_1^3 \lambda_3 \lambda_4 + t_{14} a_1^3 \lambda_3 \kappa_6 + t_{15} a_1^3 \kappa_5 \lambda_4 \\
& + t_{16} a_1^3 \kappa_5 \kappa_6 + t_{17} a_1^2 \lambda_3^4 + t_{18} a_1^2 \lambda_3^3 \kappa_5 + t_{19} a_1^2 \lambda_3^2 \kappa_5^2 + t_{20} a_1^2 \lambda_3 \kappa_5^3 \\
& + t_{21} a_1^2 \kappa_5^4 + t_{22} a_1^2 \lambda_3^2 \lambda_4 + t_{23} a_1^2 \lambda_3^2 \kappa_6 + t_{24} a_1^2 \lambda_3 \kappa_5 \lambda_4 + t_{25} a_1^2 \lambda_3 \kappa_5 \kappa_6 \\
& + t_{26} a_1^2 \kappa_5^2 \lambda_4 + t_{27} a_1^2 \kappa_5^2 \kappa_6 + t_{28} a_1^2 \lambda_4^2 + t_{29} a_1^2 \lambda_4 \kappa_6 + t_{30} a_1^2 \kappa_6^2 \,.
\end{aligned}
\tag{4.7}
$$

To determine the form factors $t_1 \ldots t_{30}$, we calculate the total cross section at 480 selected points in the space of parameters $(a_1, \lambda_3, \lambda_4, \kappa_5, \kappa_6)$, then obtain the numerical values of these coefficients $t_1 \ldots t_{30}$ via linear regression. The results are shown in the Table. 4.4. The complete set of results

t_1	t_2	t_3	t_4	t_5	t_6	t_7	t_8	t_9	t_{10}
7.57	-7.79	-13.9	4.33	14.7	12.3	0.13	-0.79	-0.95	-7.63

t_{11}	t_{12}	t_{13}	t_{14}	t_{15}	t_{16}	t_{17}	t_{18}	t_{19}	t_{20}
-18.8	-16.4	-0.63	-3.16	-1.07	-6.47	0.09	1.12	5.61	13.6

t_{21}	t_{22}	t_{23}	t_{24}	t_{25}	t_{26}	t_{27}	t_{28}	t_{29}	t_{30}
17.2	0.12	0.55	0.85	5.38	1.34	14.7	0.04	0.54	3.22

Table 4.4: Numerical values of $t_1 \ldots t_{30}$ for a 100 TeV hadron collider, for use in Eq. (4.7).

that accounts for all effective operators is provided in the Appendix A.

To reduce the coefficients and study the effects of the Higgs self-interaction, we follow the procedure of [31] and focus on a subset of the dimension-6 operators:

$$\mathcal{O}_1 = \frac{f_1}{\Lambda^2}(D^\mu H)^\dagger HH^\dagger(D_\mu H), \tag{4.8}$$

$$\mathcal{O}_2 = \frac{f_2}{2\Lambda^2}\partial^\mu(H^\dagger H)\partial_\mu(H^\dagger H), \tag{4.9}$$

$$\mathcal{O}_3 = \frac{f_3}{3\Lambda^2}(H^\dagger H)^3, \tag{4.10}$$

$$\mathcal{O}_4 = \frac{f_4}{\Lambda^2}(D^\mu H)^\dagger(D_\mu H)(H^\dagger H). \tag{4.11}$$

The operator $\mathcal{O}_1$ can safely be neglected Ref. [103]. As explained in section 3.2, $\mathcal{O}_4$ can be eliminated by EOM. Thus we only need to consider the operators $(\mathcal{O}_2, \mathcal{O}_3)$.

In this case, the subset $(a_1, \lambda_3, \lambda_4, \kappa_5, \kappa_6)$ can be expressed in terms of just two independent parameters:

$$\hat{x} = x_2\zeta_h^2, \tag{4.12}$$

$$\hat{r} = -x_3\zeta_h^2\frac{2v^2}{3m_h^2}, \tag{4.13}$$

where $x_i = f_i v^2/\Lambda^2$ $(i = 2, 3)$. With this definition, the rescaling factor ζ_h can be rewritten as $\zeta_h = (1 - \hat{x})^{1/2}$. The parameters relations are listed in the Table. 4.5.

To study the parameter dependence of $(\hat{r}, \hat{x})$, we parameterize the cross section of $gg \to hhh$ to

$$\begin{aligned} \sigma(pp \to hhh) = \sigma_{SM}^{hhh}(1 - \hat{x})^3(1 &+ \hat{t}_1\hat{x} + \hat{t}_2\hat{r} + \hat{t}_3\hat{x}^2 + \hat{t}_4\hat{x}\hat{r} + \hat{t}_5\hat{r}^2 \\ &+ \hat{t}_6\hat{x}^3 + \hat{t}_7\hat{x}^2\hat{r} + \hat{t}_8\hat{x}\hat{r}^2 + \hat{t}_9\hat{r}^3 \\ &+ \hat{t}_{10}\hat{x}^4 + \hat{t}_{11}\hat{x}^3\hat{r} + \hat{t}_{12}\hat{x}^2\hat{r}^2 + \hat{t}_{13}\hat{x}\hat{r}^3 + \hat{t}_{14}\hat{r}^4) \end{aligned} \tag{4.14}$$

The numerical results for $\hat{t}_1 \ldots \hat{t}_{14}$ are listed in Table 4.6, and the total cross section has the value $\sigma_{SM}^{hhh} = 5.84$ fb. (This includes a K factor of 2.0, following Ref. [69]).

Our operators	Operators in Ref. [31]	Relations
$-\frac{m_t}{v}a_1\bar{t}th$	$-\frac{m_t}{v}\zeta\bar{t}th$	$a_1 = \zeta$
$-\lambda_3\frac{m_h^2}{2v}h^3$	$-\frac{\zeta}{2v}(1+\hat{r})m_h^2 h^3$	$\lambda_3 = \zeta(1+\hat{r})$
$-\lambda_4\frac{m_h^2}{8v^2}h^4$	$-\frac{\zeta^2}{8v^2}(1+6\hat{r})m_h^2 h^4$	$\lambda_4 = \zeta^2(1+6\hat{r})$
$-\frac{1}{2v}\kappa_5 h(\partial h)^2$	$\frac{1}{v}\hat{x}\zeta h(\partial h)^2$	$\kappa_5 = -2\hat{x}\zeta$
$-\frac{\kappa_6}{4v^2}h^2(\partial h)^2$	$\frac{\hat{x}}{2v^2}\zeta^2 h^2(\partial h)^2$	$\kappa_6 = -2\hat{x}\zeta^2$

Table 4.5: Parameter relationship between the convention of Eq. 3.2 and that in Ref. [31].

$\hat{t}_1$	$\hat{t}_2$	$\hat{t}_3$	$\hat{t}_4$	$\hat{t}_5$	$\hat{t}_6$	$\hat{t}_7$	$\hat{t}_8$	$\hat{t}_9$	$\hat{t}_{10}$	$\hat{t}_{11}$	$\hat{t}_{12}$	$\hat{t}_{13}$	$\hat{t}_{14}$
6.02	-1.29	3.51	-2.40	0.48	-32.5	8.07	-0.96	0.05	94.20	-37.20	7.69	-0.77	0.03

Table 4.6: Numerical values of integrated form factors in Eq. 4.14.

Fig. 4.7 presents the cross section dependence on the parameters $(\hat{x}, \hat{r})$. It is shown that the cross section can exceed the SM value by two orders of magnitude for reasonable variations of $(\hat{x}, \hat{r})$. In particular, if $\hat{r}$ is fixed (Fig. 4.7(a)), the cross section increases in the $\hat{x} < 0$ region. In this region, all of the dependent parameters λ_3, λ_4, κ_5, and κ_6 have the same sign, and the derivative couplings can greatly enhance the cross section. In contrast, in the $\hat{x} > 0$ region, the contributions of λ_3 and λ_4 cancel against the terms with κ_5 and κ_6.

The complementary plot Fig. 4.7(b) shows the dependence on $\hat{r}$, with fixed $\hat{x}$. The cross section changes only mildly with $\hat{r}$ as long as $\hat{x}$ is small or positive, and for $\hat{r} > 0$ it actually undershoots the SM value. It is known that the dominant contribution to triple-Higgs production is the diagram with a pentagon top-quark loop [71]. This part does not depend on the Higgs self-couplings which enter the parameter $\hat{r}$. Only if the Higgs self-couplings become sizable and the interference is constructive, one can expect a large enhancement of the cross section.
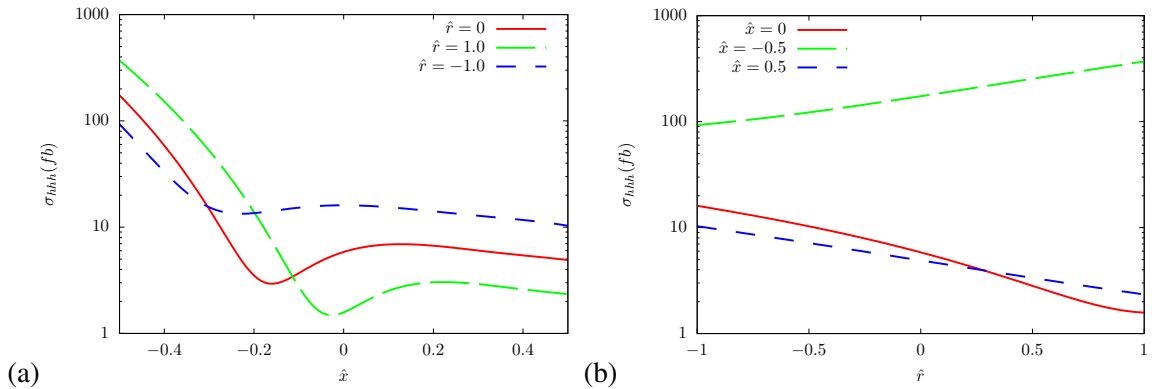
Figure 4.7: Dependence of the cross section on (a) $\hat{x}$ and (b) $\hat{r}$. The other observable is kept fixed, as indicated by the curve labels.

Besides the effects on the total cross section, it is also interesting to study distortions of kinematical distributions. The P_t distributions of the three Higgs bosons are shown in Fig. 4.8(a), Fig. 4.8(b), and Fig. 4.8(c), for three different values of $\hat{x}$: -0.5, 0 and $+0.5$, respectively. We observe that the distributions change significantly with respect to the SM reference value if $\hat{x} = +0.5$, especially in the large P_t region. The distortion happens in the parameter region where the total cross section is not enhanced by a large factor, and it is helpful for the reconstruction of the softest jet in the $2b2l^{\pm}4j + \not{E}$ channel. For $\hat{x} = -0.5$, the distributions do not change that much, but the analysis would benefit from the remarkable enhancement of the cross section in the negative region of $\hat{x}$. We also show the invariant mass distribution of the three Higgs bosons (Fig. 4.8(d)); this is also modified by the derivative operator.
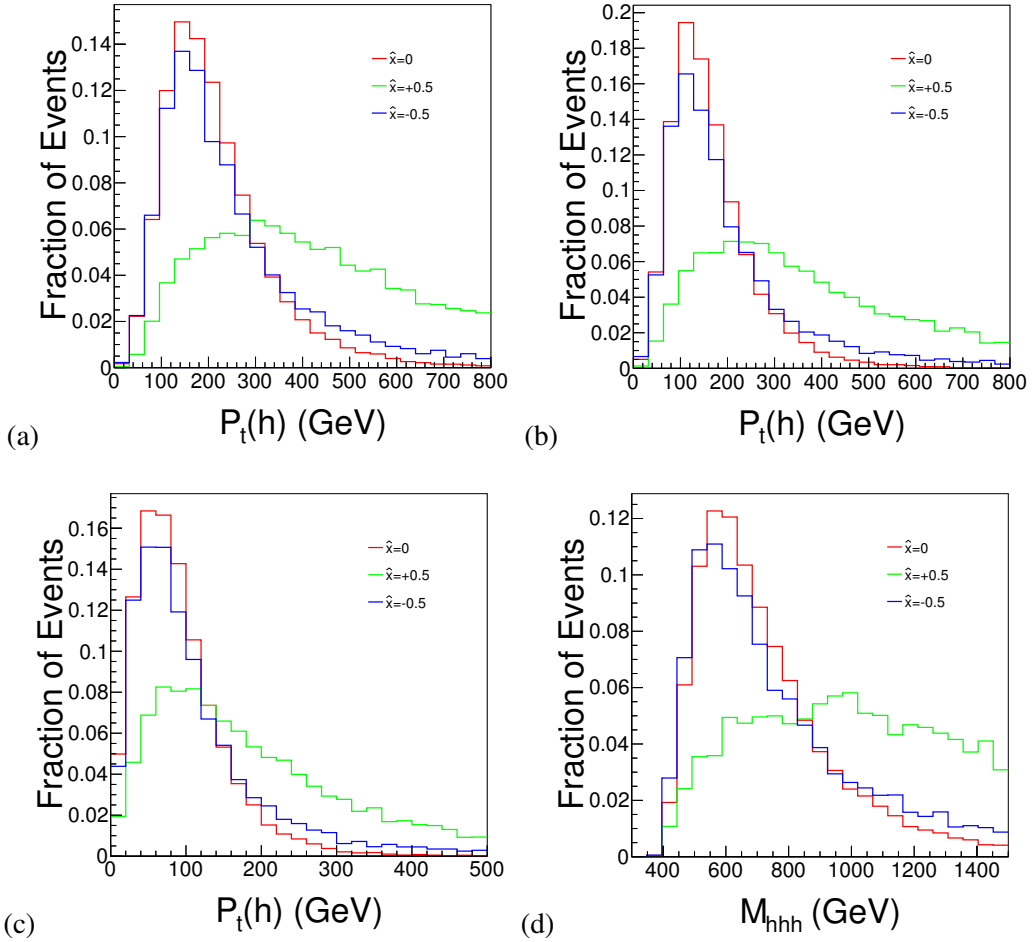
Figure 4.8: P_t distributions of (a) the leading Higgs, (b) the sub-leading Higgs, and (c) the softest Higgs. In (d), we show the distribution of the invariant mass of the triple-Higgs system. We plot results for three values of $\hat{x}$: -0.5, 0 and $+0.5$, where $\hat{r}$ is fixed to zero.

In Fig. 4.9, we show the same observables as in Fig. 4.8; this time $\hat{r}$ is varied and $\hat{x}$ is fixed to zero. The distributions do not actually depend on $\hat{r}$, since the parameter affects only λ_3 and λ_4, while

the the distrubutions are affected by the derivative operator.
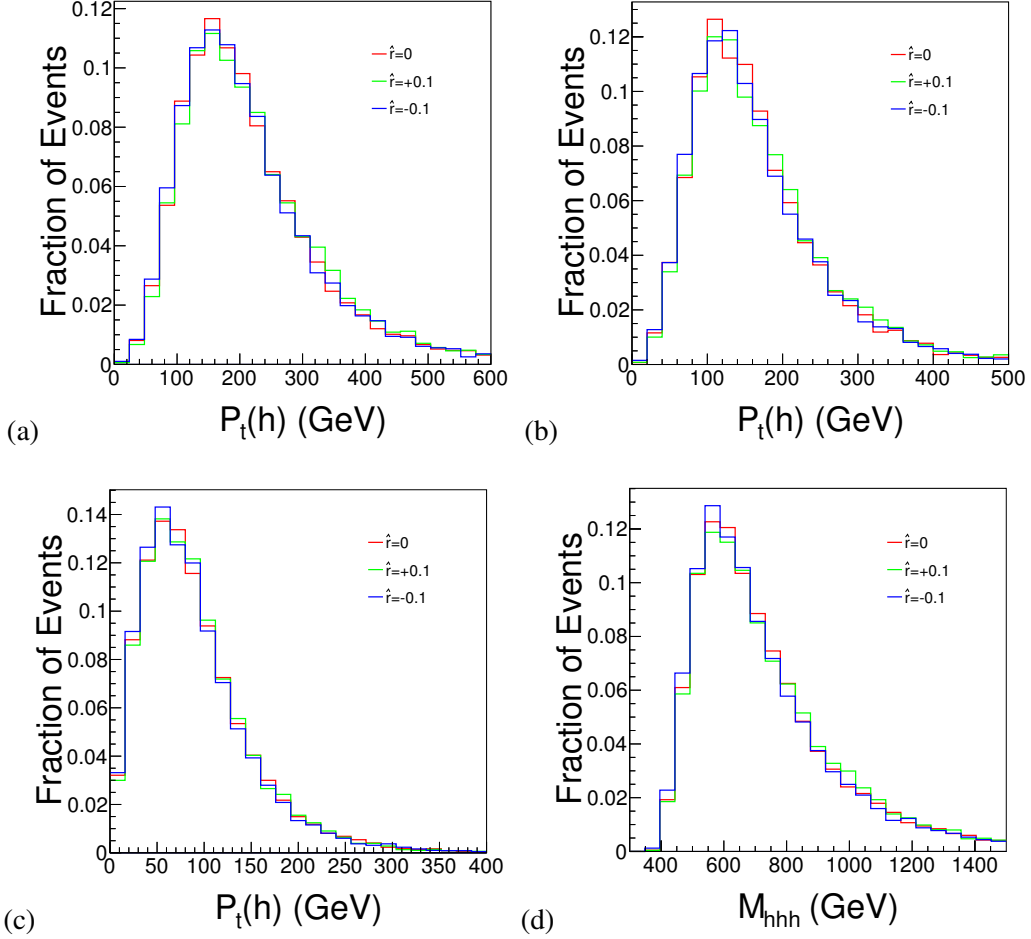
Figure 4.9: P_t distributions of (a) the leading Higgs, (b) the sub-leading Higgs, and (c) the softest Higgs. In (d), we show the distribution of the invariant mass of the triple-Higgs system. We plot results for three values of $\hat{r}$: -0.1, 0 and $+0.1$, where $\hat{x}$ is fixed to zero.

4.2.3 Correlations between $gg \to hhh$ and single and double-Higgs production

The parameters in Eq. 3.2 can not only contribute to triple-Higgs production, but also contribute to other collider processes. The discussion in Chapter 3 suggests that in typical strongly-interacting models, all parameters would receive NP contributions. We can expect that a measurement or exclusion limit on the triple-Higgs process would add information to current Higgs-physics data, and all results should be combined in searching NP. Therefore, in this subsection we study correlations between $gg \to hhh$ and $gg \to h$ and $gg \to hh$. The parameters that contribute to single, double, and triple Higgs production are listed in the Table. 4.7. We consider the following questions:

- To what extent can a_1 and c_1 be determined by measuring $gg \to h$ at the 14 TeV LHC and at a

	$gg \to h$	$gg \to hh$	$gg \to hhh$
Parameters	a_1, c_1	a_1, c_1	a_1, c_1
involved	-	$a_2, c_2, \lambda_3, \kappa_5$	$a_2, c_2, \lambda_3, \kappa_5$
	-	-	a_3, λ_4, κ_6

Table 4.7: Parameters that contribute to the particular Higgs-production processes.

Process	$\sigma(14\,TeV)$ (fb)	err.[th]	err.[exp]	$\sigma(100\,TeV)$ (fb)	err.[th]	err. [exp]
$gg \to h$	4.968×10^4	$+7.5\%$ -9.0%	$\pm 1\%$	8.02×10^5	$+7.5\%$ -9.0%	$\pm 0.1\%$
$gg \to hh$	45.05	$+7.3\%$ -8.4%	$< 120 fb$	1749	$+5.7\%$ -6.6%	$\pm 5\%$
$gg \to hhh$	0.0892	$+8.0\%$ -6.8%	$-$	4.82	$+4.1\%$ -3.7%	$< 30 fb$

Table 4.8: Cross sections of the processes $gg \to h$, $gg \to hh$ and $gg \to hhh$ at 14 TeV and 100 TeV hadron colliders, respectively. The 14 TeV cross section of $gg \to h$ is taken from Ref. [105]; the other values are taken from Ref. [64]. The cross sections for $gg \to h$ and $gg \to hh$ are the NNLO results, while the cross sections for $gg \to hhh$ are the NLO results.

100 TeV collider?

- To what extent can $a_2, c_2, \lambda_3, \kappa_5$ be determined by measuring $gg \to hh$ at the 14 TeV LHC and at a 100 TeV Collider?

- To what extent can a_3, λ_4, κ_6 be determined from $gg \to hhh$ at a 100 TeV collider, including other channels of Higgs bosons?

Table 4.8 lists the cross sections of $gg \to h$, $gg \to hh$ and $gg \to hhh$ with theoretical and projected experimental uncertainties. The theoretical uncertainties are obtained by summing the squared uncertainties in parton distribution function (PDF), renormalisation scales, and α_s, based on current knowledge. For the process $gg \to h$, the experimental uncertainties are mainly statistical ones which pertain to the Higgs decay $h \to \gamma\gamma$. The projected experimental bound for $gg \to hh$ at the LHC is taken from the studies of the $b\bar{b}\gamma\gamma$ final state [31] and $3\ell 2j$+MET [62]. The experimental bound for $gg \to hhh$ is obtained from the analysis of $4b2\gamma$ final states [71] at 100 TeV. These estimates are derived from phenomenological studies; full simulation and experience gained in the analysis of actual data may change the conclusions significantly, such as in the expectations for the observation of Higgs-pair production at the LHC [104].

We first consider Higgs-pair production in ggF. Analogy to the triple-Higgs production, the dependence of the total cross section on the EFT parameters can be written as

$$\begin{aligned}
\sigma(pp \to hh) = & f_1 a_1^4 + f_2 a_1^3 \lambda_3 + f_3 a_1^3 \kappa_5 + f_4 a_1^2 \lambda_3^2 + f_5 a_1^2 \lambda_3 \kappa_5 \\
& + f_6 a_1^2 \kappa_5^2 + f_7 a_1^2 a_2 + f_8 a_1 \lambda_3 a_2 + f_9 a_1 \kappa_5 a_2 + f_{10} a_2^2 .
\end{aligned} \tag{4.15}$$

f_1	f_2	f_3	f_4	f_5	f_6	f_7	f_8	f_9	f_{10}
1.56	-0.94	-2.14	0.18	0.69	0.87	-3.34	1.01	2.77	2.26

Table 4.9: Numerical results for $f_1 - f_{10}$ (in pb) at a 100 TeV hadron collider.

$\hat{f}_1$	$\hat{f}_2$	$\hat{f}_3$	$\hat{f}_4$	$\hat{f}_5$
-3.63	-0.72	4.32	1.72	0.23

Table 4.10: Numerical results for $\hat{f}_1 - \hat{f}_5$ at a 100 TeV hadron collider.

The numerical values for the form factors $f_1 - f_{10}$ at a 100 TeV hadron collider are listed in Table 4.9.

By substituting $(a_1, \lambda_3, \lambda_4, \kappa_5)$ into $(\hat{r}, \hat{x})$ according to Table 4.5, we obtain

$$\sigma(pp \to hh) = \sigma_{SM}^{hh}(1 - \hat{x})^2(1 + \hat{f}_1\hat{x} + \hat{f}_2\hat{r} + \hat{f}_3\hat{x}^2 + \hat{f}_4\hat{x}\hat{r} + \hat{f}_5\hat{r}^2), \tag{4.16}$$

where $\sigma_{SM}^{hh} = 1.75$ pb (a NNLO K factor of 2.17 [106] is included.). Table 4.10 lists the numerical results for $\hat{f}_i$.

For the single Higgs process, $gg \to h$, Fig. 4.10 shows projections on the bounds of a_1 and c_1 at the LHC (14 TeV) and at a 100 TeV collider, respectively. Assuming that a measurement result is close to the SM prediction, the allowed ranges for a_1 and c_1 are highly correlated and are confined to be two narrow bands, one of which containing the SM reference point. The other band includes a mirror solution $a_1 = -1$, $c_1 = 0$. To distinguish these solutions, we can examine the kinematics of the Higgs boson in the final state, and add the measurement of $gg \to hh$, which will be explained later.

At the 14 TeV LHC, both theoretical and experimental (statistical) uncertainties are relevant and have to be taken into account. At a 100 TeV collider, the statistical uncertainties are expected to be less than 0.1%, so the main uncertainties will come from theory. Compared with the LHC bounds, the projected accuracy of a_1 and c_1 will improve by a factor 2 at a 100 TeV collider.

Fig. 4.11 shows the expected bounds in the a_1-c_1 plane for both the LHC 14 TeV and a 100 TeV collider. Combining the measurement of $gg \to h$ and $gg \to hh$, the a_1-c_1 plane is cut down to a limited region, even for the LHC 14 TeV. At a 100 TeV collider, the degenerate solutions for both $gg \to h$ and $gg \to hh$ seperate into four small regions, and it becomes possible to exclude the mirror solution. We calculate the cross sections of $gg \to h$, $gg \to hh$ and $gg \to hhh$ in these four regions, and the results of four bechmark points are listed in the Table. 4.11. It is interesting that the second point has a production rate for the process $gg \to hhh$ that is large enough to be observed.

We now consider the other parameters that enter $gg \to hh$. Fig. 4.12 shows the expected LHC bounds of those parameters in four planes, namely a_2-λ_3, c_1-λ_3, c_2-λ_3, and κ_5-λ_3. All bounds are
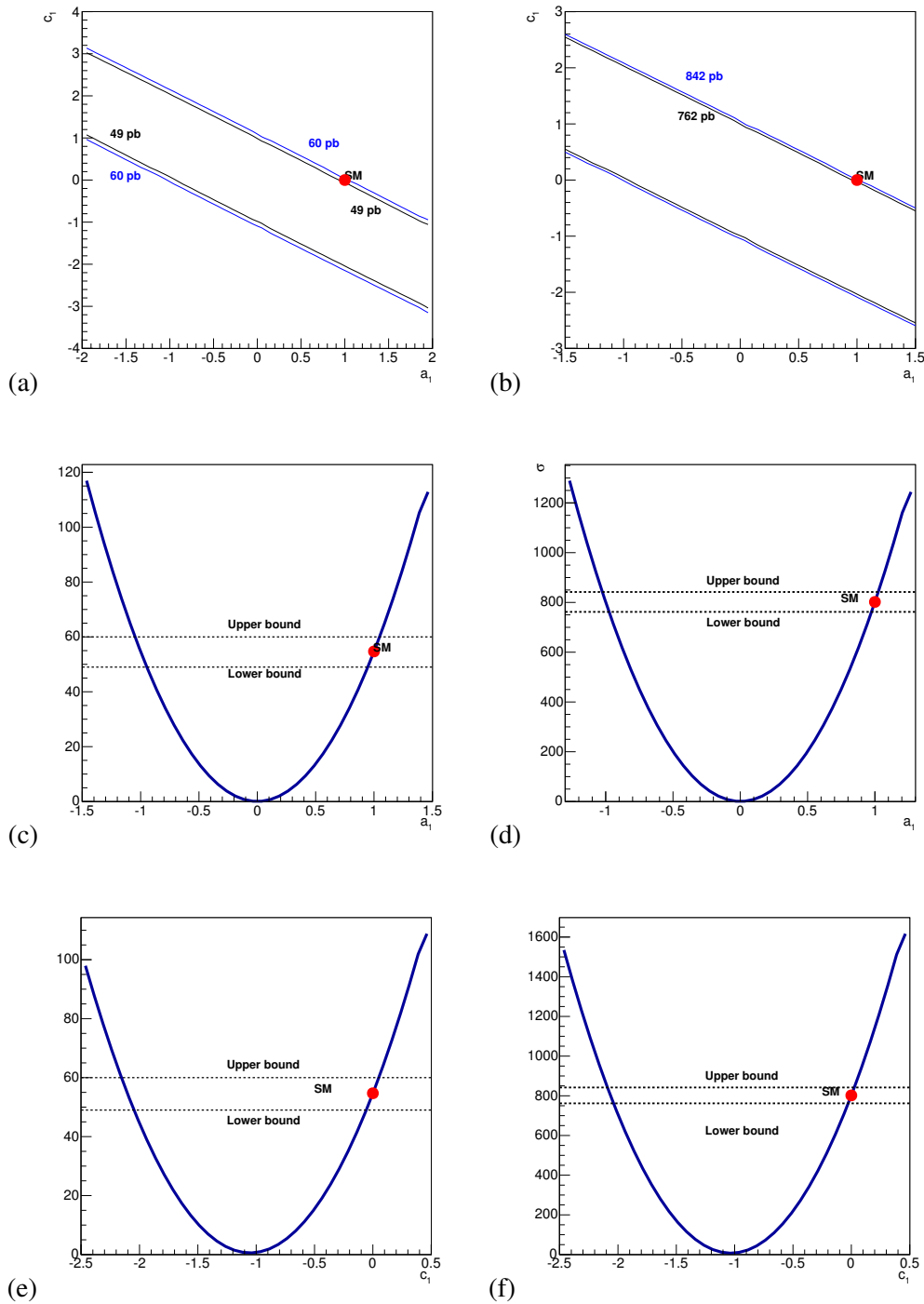
Figure 4.10: Upper row: correlations between a_1 and c_1 extracted from the process $gg \to h$ for the LHC 14 TeV (a) and for a 100 TeV pp collider (b), respectively. Middle row: individual bounds on a_1 (c) and c_1 (e) for the LHC 14 TeV (the total uncertainties are assumed to be 10%), respectively. Lower row: the analogous results for a 100 TeV pp collider (the total uncertainties are assumed to be 5%).
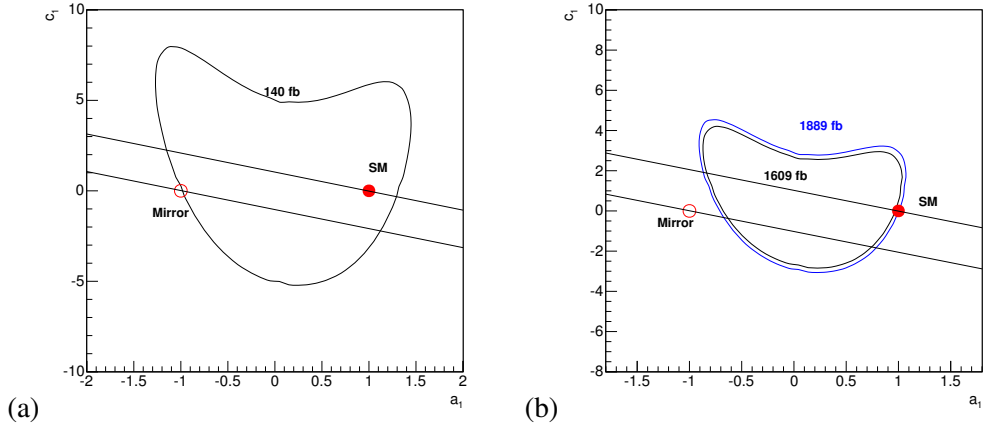
Figure 4.11: Projected exclusion bounds in a_1-c_1 plane extracted from the process $gg \to hh$ for both (a) the LHC 14 TeV and (b) a 100 TeV collider. In each plot, the straight lines indicate the solutions for the cross section of $gg \to h$, assuming a measurement consistemt with the SM. The mirror region of the SM point, the solution with $a_1 = -1$ and $c_1 = 0$, is denoted by a circle, respectively.

No.	a_1	c_1	$\sigma(gg \to h)$ [pb]	$\sigma(gg \to hh)$ [fb]	$\sigma(gg \to hhh)$ [fb]
1	0.99	-0.01	771	1710	5.90
2	-0.86	1.94	839.6	1685	29.7
3	0.78	-1.82	763	1747	6.23
4	-0.66	-0.37	817.8	1690	5.74

Table 4.11: Four representative points in the four parameter regions and the corresponding cross sections for Higgs production at a 100 TeV collider.

obtained by requiring the cross section of $gg \to hh$ to be smaller than 140 fb, so the points inside the exclusion bounds is allowed by the LHC 14 TeV data, if no deviation from the SM is detected. The SM reference points are also shown. Because we are interested in the correlations between two parameters, the remaining parameters are set to their SM values.

Similarly, the bounds from the $gg \to hh$ data at 100 TeV are plotted in Fig. 4.13. Combining theoretical and experimental uncertainties, we assume that the cross section of $gg \to hh$ can be measured to a precision of 8%. The allowed parameter regions shrink considerably and become pinched between two contours, in each plot. Comparing Fig. 4.12 with Fig. 4.13, it is obviously that a 100 TeV collider can significantly improve the precision on a_2, c_2, κ_5, and λ_3.

We also individually project out single-parameter bounds for each of $(a_2, c_2, \kappa_5, \lambda_3)$, as shown in Fig. 4.14. We find that the parameters a_2, κ_5, and λ_3 can be determined with a precision close to 10%. The two-fold ambiguities in the solutions can be removed by using the kinematics of final states, as demonstrated in Ref. [62]. We also find that the parameter c_2 can be determined within the range $[-0.1, 0.4]$.
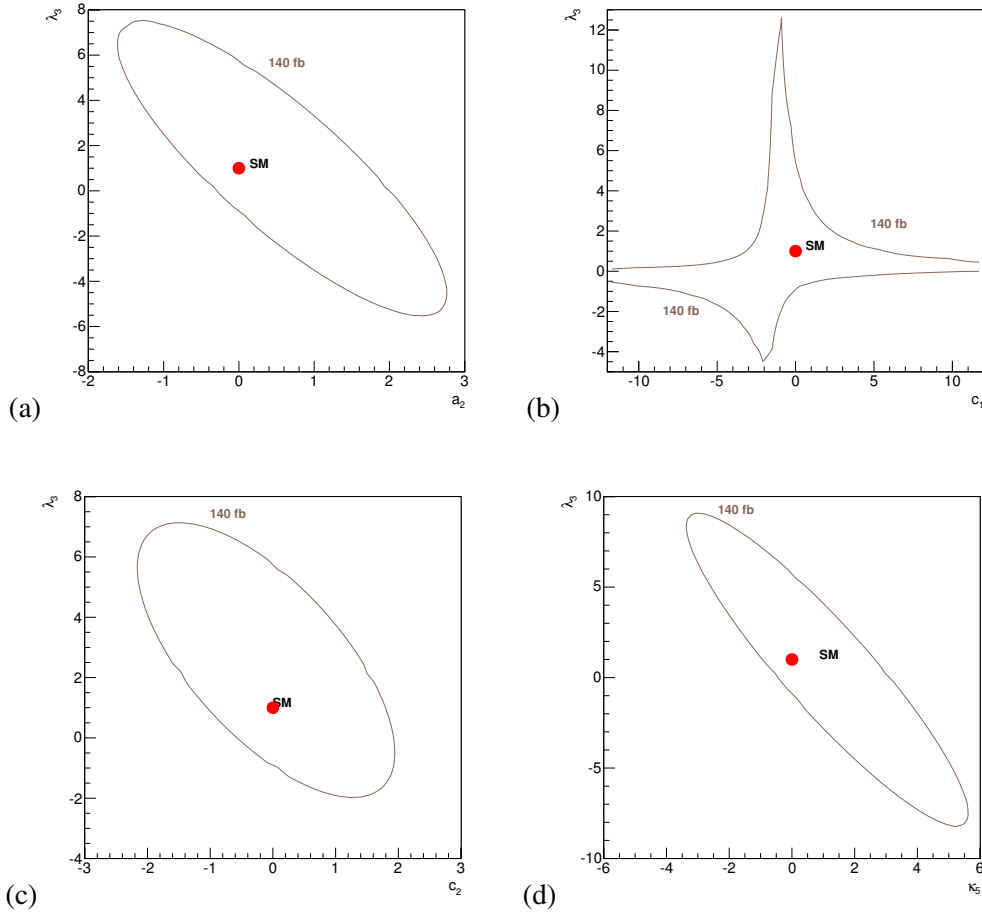
Figure 4.12: Projected exclusion bounds in two-parameter planes between $(a_2, c_1, c_2, \kappa_5)$ and λ_3, extracted from the process $gg \rightarrow hh$ at the LHC 14 TeV. If the coefficient values are equal to the SM prediction, parameter values inside the contours are still allowed by the measurement. The exclusion bounds correpond to a limit of 140 fb for the cross section.

Finally, we consider the remaining parameters that only enter the process $gg \rightarrow hhh$. They are a_3, κ_6 and λ_4. We present two-dimensional bounds for all pairs of these parameters in Figs. 4.15(a)– 4.15(c). The corresponding one-dimensional bounds are given in Figs. 4.15(b)–4.15(d). In this study, we find that the parameter a_3 can be constrained to the range [-0.8,1.2], and the parameter κ_6 can be constrained to the range [-2.3, 1.5]. λ_4 is the most difficult parameter to measure. It can only be determined within a quite wide range [-13,20], as already in Ref. [71].

These results have to be combined with the parameter exclusion regions derived from $gg \rightarrow hh$. In Fig. 4.16, we show the correlations between a_3 and the parameters that enter $gg \rightarrow hh$ (a_2, c_2, κ_5, λ_3). In these plots, we combine the bounds from Higgs-pair production, presented in Fig. 4.14, and the exclusion limits from triple-Higgs production. The SM prediction is included in the plots for reference. Clearly, constraints from $gg \rightarrow hhh$ are weak, but they are nevertheless sensitive to a
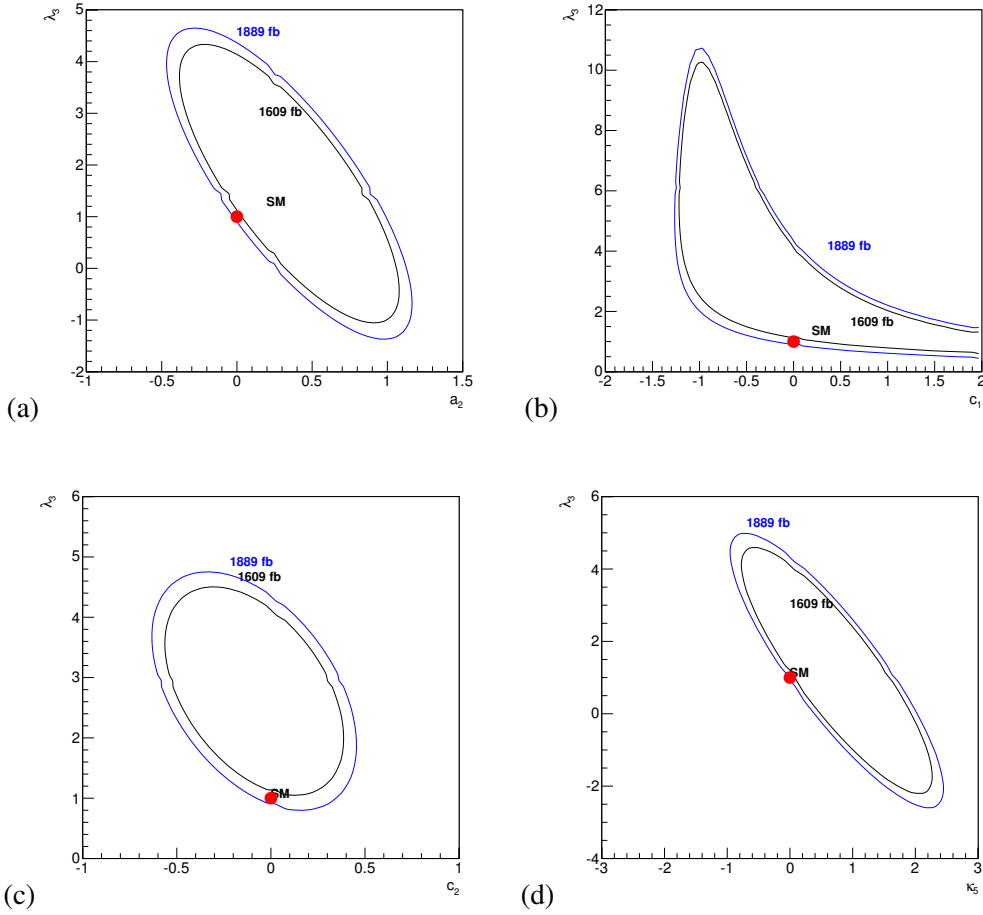
Figure 4.13: Projected exclusion bounds in two-parameter planes between (a_2, c_1, c_2, κ_5) and λ_3, extracted from the process $gg \rightarrow hh$ a 100 TeV pp collider. If the coefficient values are equal to the SM prediction, parameter values between the two contours are still allowed by the measurement. The exclusion bounds correspond to a total error of 8% on $\sigma(gg \rightarrow hh)$, theoretical and experimental uncertainties combined.

special combination of parameters and thus cut off part of the two-parameter exclusion regions. As an example, we indicate that adding in $gg \rightarrow hhh$ can help in resolving a two-fold ambiguity in the κ_5-a_3 plane, cf. Fig. 4.16(c).

Similarly, in Fig. 4.17, we show the correlations between κ_6 and parameters set (a_2, c_2, κ_5, λ_3). In Fig. 4.18, we show the correlations between λ_4 and the same parameters. In the κ_5-λ_4 plane (Fig. 4.18(c)), including triple-Higgs production it becomes possible to separate the $\kappa_5 = 0$ and $\kappa_5 \neq 0$ regions.
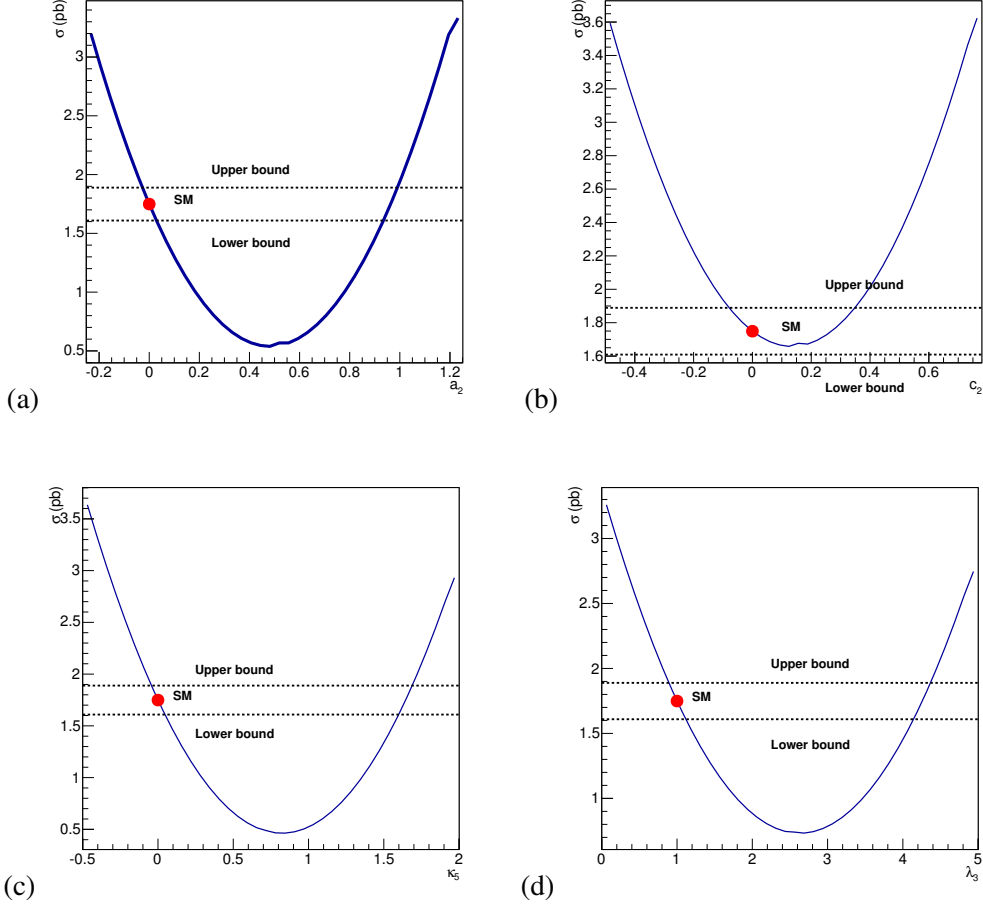
Figure 4.14: Projected one-parameter exclusion bounds for a_2, c_2, κ_5 and λ_3, extracted from the process $gg \to hh$. If the coefficient values are equal to the SM prediction, parameter values between the upper and lower bounds are allowed by the measurement. The exclusion bounds correspond to a total error of 8% on $\sigma(gg \to hh)$, theoretical and experimental uncertainties combined.

4.2.4   Analysis for models

In this subsection, we adapt the above results to the NP scenarios, which are introduced in Chapter 3. As we have discussed in the Chapter 3, the parameters in these models can be related to the parameters of Eq. 3.2. In particular, for a model with a small parameters space, we can recast the analysis to give a expected bounds to this model, by using the relations in 3.1 or 3.2.

4.2.4.1   Strongly-interacting Higgs models

In the generic dimension-six SILH Lagrangian, there are four free parameters relevant to the multi-Higgs production, denoted by $C_y = c_y\xi$, $C_H = c_H\xi$, $C_6 = c_6\xi$, and c_1. In this subsection, we also consider two more specific composite Higgs models [29, 107], known as MCHM4 and MCHM5,
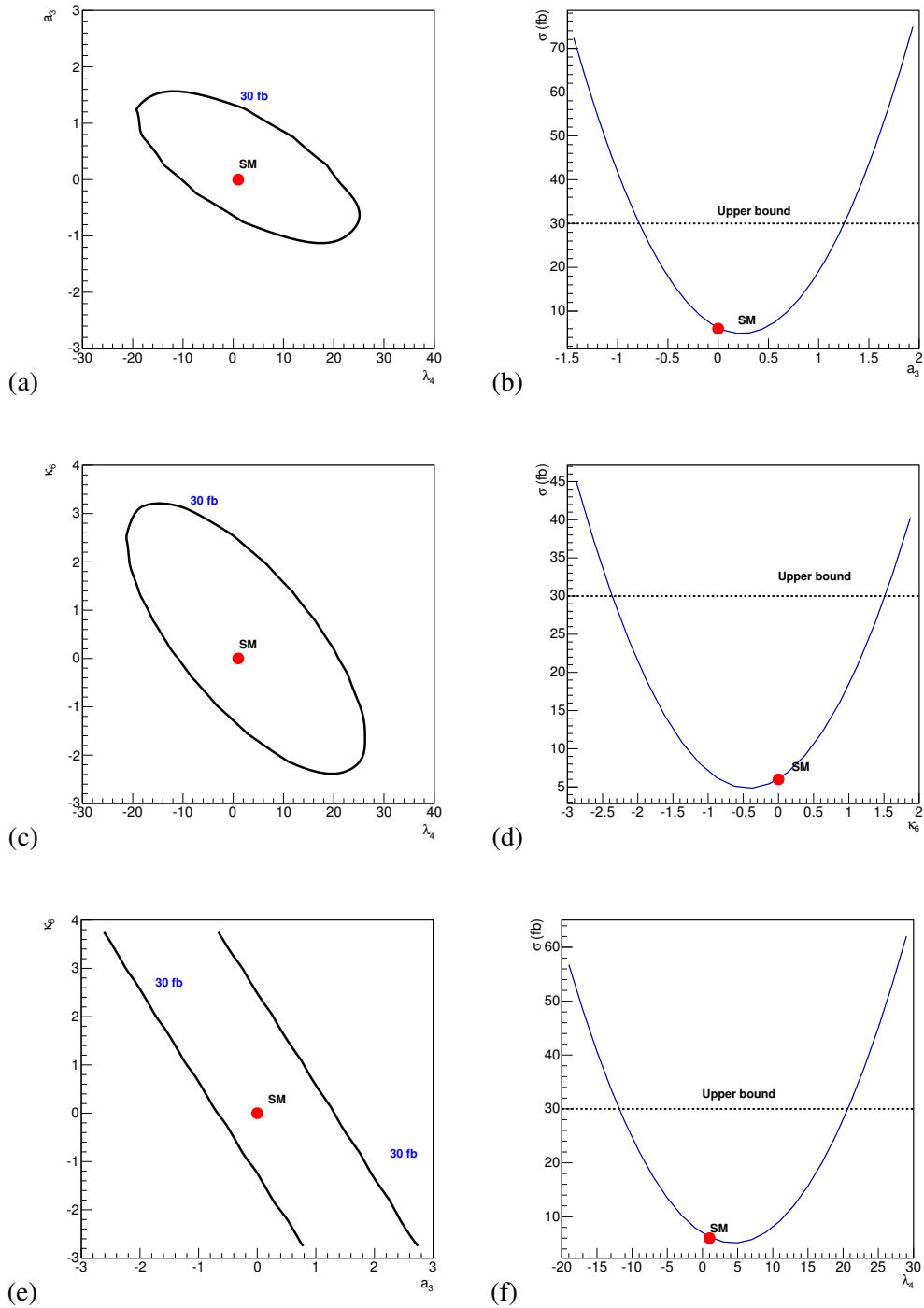
Figure 4.15: Projected two-parameter (left) and one-parameter (right) exclusion bounds, extracted from the process $gg \rightarrow hhh$. The left column shows the two-parameter planes a_3-λ_4, κ_6-λ_4, and a_3-κ_6, while the right column displays a_3, κ_6, and λ_4.
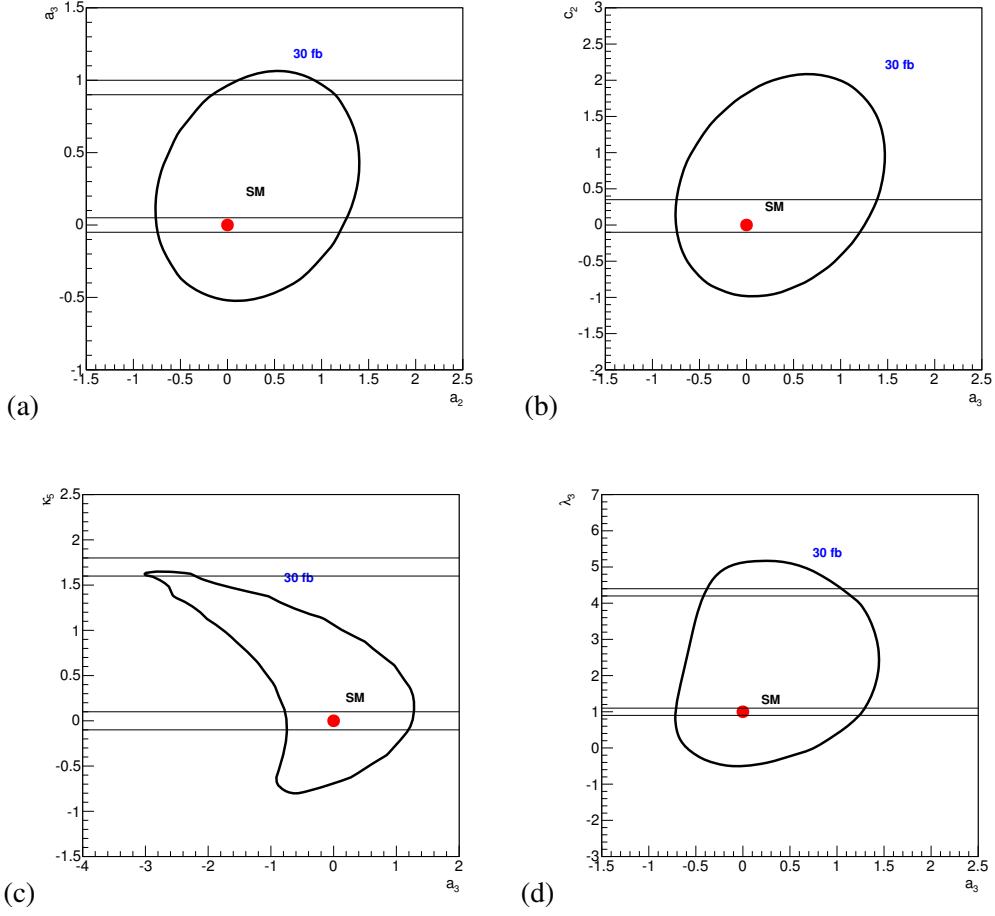
Figure 4.16: Projected two-parameter exclusion bounds, extracted from the process $gg \to hhh$. The straight-line pairs indicate the exclusion bounds extracted from $gg \to hh$. The plots show two-parameter correlations between a_3 and a_2, c_2, κ_5, and λ_3.

respectively. Both of them result in the SILH Lagrangian as their low-energy EFT. They contain extra fermions, which are in representations 4 and 5 of an assumed global $SO(5)$ symmetry, respectively. In these specific models, the SILH coefficient values are [108]

$$\text{MCHM4:} \quad c_H = 1, \quad c_y = 0, \quad c_6 = 1, \tag{4.17}$$

$$\text{MCHM5:} \quad c_H = 1, \quad c_y = 1, \quad c_6 = 0. \tag{4.18}$$

In these models, there are only two independent parameters, c_1 and ξ. We apply the above analysis to these parameters and conclude that at a 100 TeV collider, data from $gg \to h$ and $gg \to hh$ can significantly constrain the allowed parameter space. These bounds are demonstrated by Figs. 4.19(a)– 4.19(b). We expect that data from $gg \to h$ will result in an exclusion region bounded by two lines in the $\xi - c_1$ plane, while data from $gg \to hh$ will further reduce the allowed parameter space to two
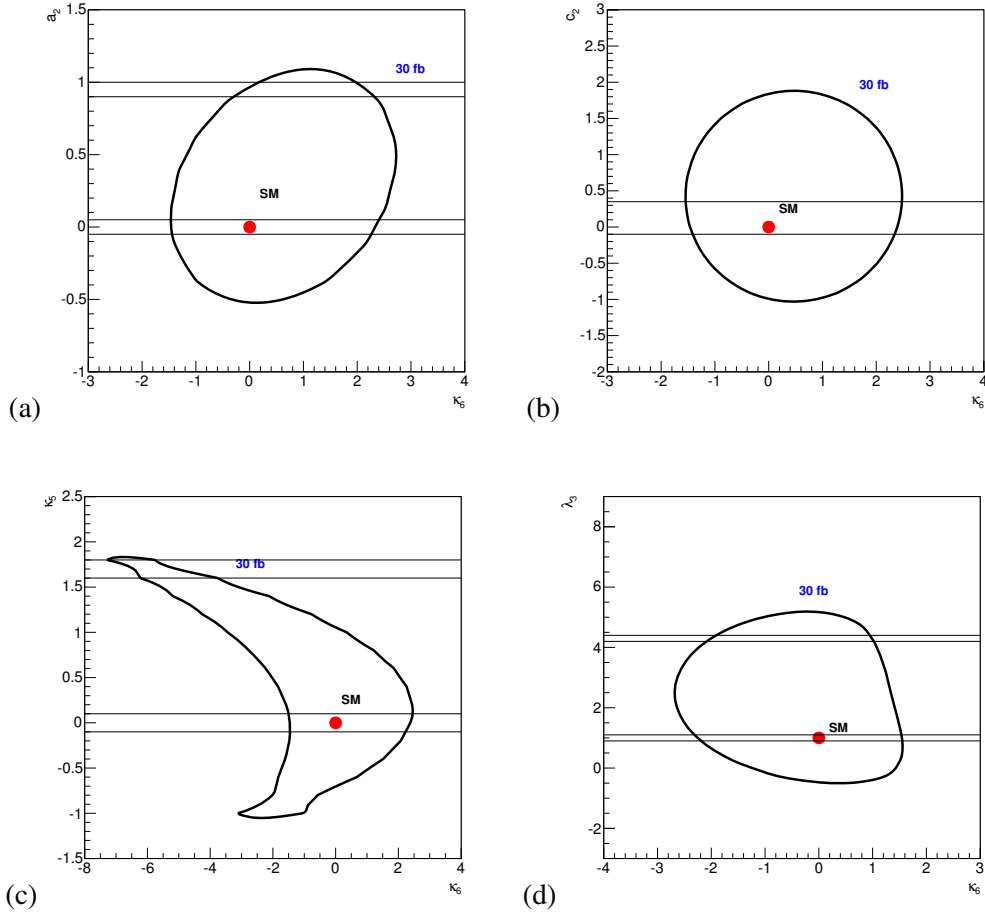
Figure 4.17: Projected two-parameter exclusion bounds, extracted from the process $gg \to hhh$. The straight-line pairs indicate the exclusion bounds extracted from $gg \to hh$. The plots show two-parameter correlations between κ_6 and a_2, c_2, κ_5, and λ_3.

small spots in the plane.

To illustrate the constraints from triple-Higgs production, we consider two benchmark points for MCHM4 and MCHM5 in Table 4.12. For both benchmark points we obtain a large cross section for the $gg \to hhh$ process, actually 80 and 55 times larger than the SM prediction, respectively. These benchmark points can not only be detected, but also be distinguished from each other at a 100 TeV collider, assuming that the threshold cross section value of $gg \to hhh$ for being sensitive to new physics is 30 fb or smaller [71].

4.2.4.2 The Gravity-Higgs Model

The Gravity-Higgs model has only two free parameters, $\hat{x}$ and $\hat{r}$. The analysis is straightforward, because single-Higgs production $gg \to h$ depends only on parameter $\hat{x}$, while double-Higgs production
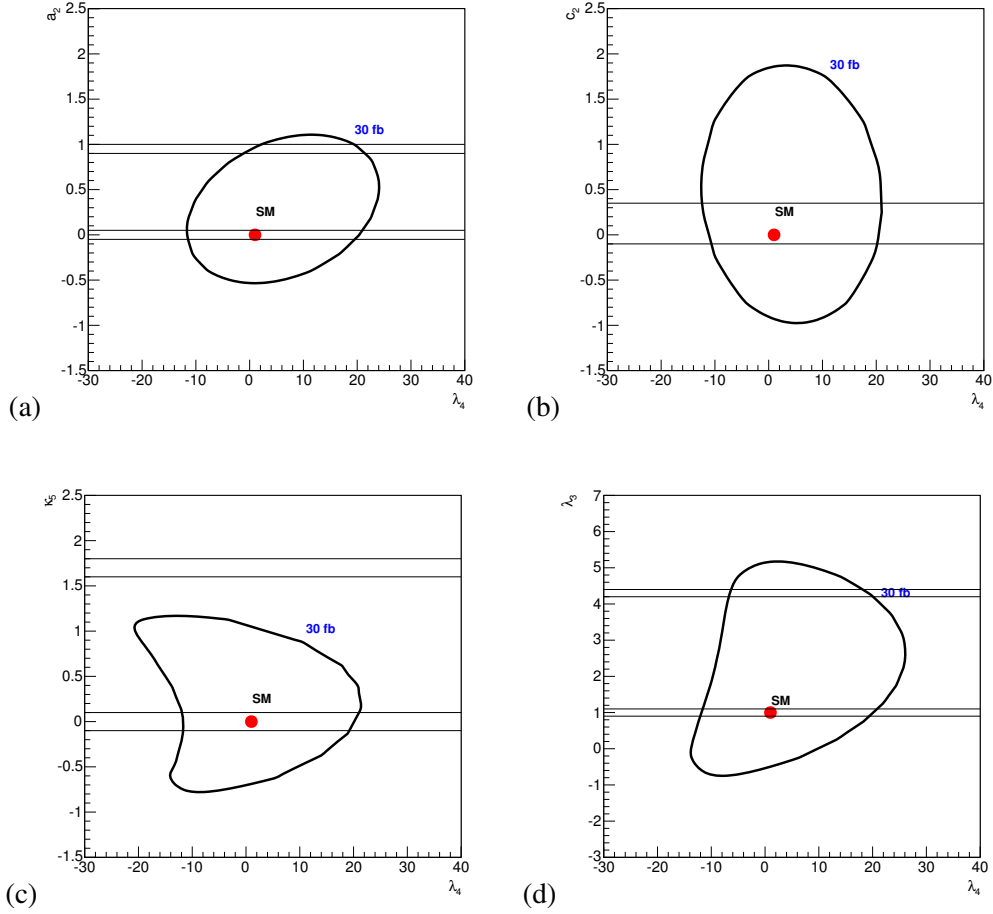
Figure 4.18: Projected two-parameter exclusion bounds, extracted from the process $gg \to hhh$. The straight-line pairs indicate the exclusion bounds extracted from $gg \to hh$. The plots show two-parameter correlations between λ_4 and a_2, c_2, κ_5, and λ_3.

No.	ξ	c_1	$\sigma(gg \to h)[pb]$	$\sigma(gg \to hh)$ [fb]	$\sigma(gg \to hhh)$ [fb]
MCHM4	0.97	0.48	764	1618	321
MCHM5	-0.20	-0.30	817	1854	122
GHM	$\hat{x} = 0.02$	$\hat{r} = 3.2$	816	1786	37.78

Table 4.12: Three representative points for the models MCHM4, MCHM5, and GHM, respectively, and the corresponding cross sections for Higgs production.
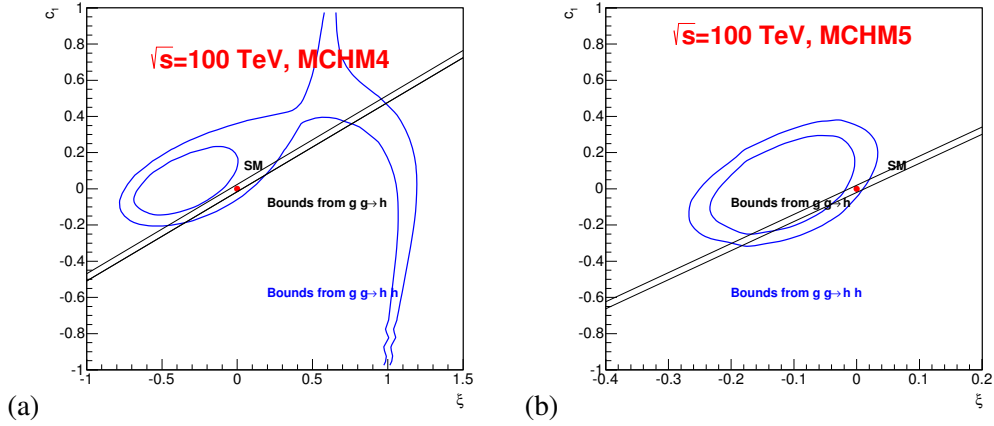
Figure 4.19: Projected two-parameter exclusion bounds in the $\xi - c_1$ plane, extracted from the processes $gg \to h$ and $gg \to hh$ at a 100 TeV collider for the models MCHM4 and MCHM5, respectively.

constrains the second parameter $\hat{r}$. The cross section of $gg \to hhh$ is completely determined once $\hat{x}$ and $\hat{r}$ are detected.

The expected LHC exclusion contours in the $\hat{x} - \hat{r}$ plane are depicted in Fig. 4.20(a). From the process $gg \to h$ we obtain a narrow band, and then the result from $gg \to hh$ further shrink the allowed region. The latter constrains the parameter $\hat{r}$ down to the range $[-1.8, 5.0]$ if we assume that parameter space with a cross section of $\sigma(gg \to hh)$ larger than 120 fb can be excluded safely.
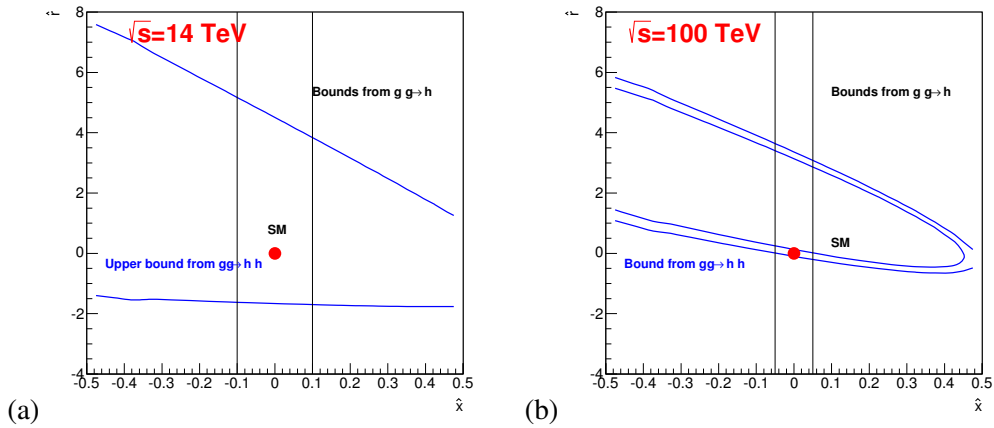
Figure 4.20: Comparison of the projected exclusion bounds on $\hat{x} - \hat{r}$ from the LHC 14 TeV (left) and a 100 TeV collider (right).

Fig. 4.20(b) shows the analogous results for a 100 TeV collider. The measurements of $gg \to h$ and $gg \to hh$ will further constrains the parameters in a small region. From these measurements alone, the value of $\hat{r}$ is extracted with a two-fold ambiguity. However, for the solution with the larger value of $\hat{r}$ ($\hat{r} \approx 3$), the cross section of $gg \to hhh$ is 5 times larger than the region near SM prediction, due

to the λ_3^4 dependence in the cross section. An benchmark point is listed in Table 4.12. A measurement of triple-Higgs production could therefore eliminate one of the solutions.

Chapter 5

Multi-Higgs production via vector boson fusion mode

The subdominant process of multi-Higgs production in hadron collisions is so-called vector-boson-fusion (VBF) [109], $VV \to hh$ and $VV \to hhh$ ($V = W^{\pm}, Z$), where the vector bosons are effectively radiated from incoming quarks. In addition to its dependence on Higgs self-couplings, this process is also sensitive to the $hhVV$ couplings, which is another SM interaction that has not been accessible by current experiment data. At the LHC, hVV coupling is determined by the measurement of the decay branching ratios of $h \to WW^*$ and $h \to ZZ^*$. The current LHC data show that these branching ratios are consistent to the SM predictions [17, 18]. By constrast, there are no significant constraints from data on $hhVV$ direct couplings.

The VBF mode of double-Higgs production at hadron colliders has been widely studied [110, 111, 112, 113, 114]. Comparing with ggF process, the NLO QCD correction is less important in VBF process. It is found that the cross section is enhanced by $\sim 7\%$ [115, 116]. In the high-luminosity LHC (HL-LHC) with 3000 fb^{-1} at 14 TeV, the $hhVV$ interaction is expected to be constrained to 20%. A 100 TeV hadron collider has the potential to reduce the uncertainty down to 1% [113]. The $hhWW$ coupling is also accessible in the $W^{\pm}W^{\pm}h$ final state. In Ref. [117] it is found that this particular final state can constrain this coupling to $O(100\%)$ at the HL-LHC, which is reduced to 20% at a 100 TeV collider.

In analogy to double-Higgs production, the triple-Higgs final state and thus the quartic Higgs self-coupling can also be examined in the VBF mode. The VBF topology is able to improve the signal-to-background ratio considerably, since two forward jets can suppress the QCD activity in the central region. This process is also sensitive to a $hhhVV$ interaction which does not exist in the SM but should be expected for a strongly interacting Higgs sector [118]. Furthermore, an anomalous hVV coupling would have a strong impact on triple Higgs production in VBF mode [119].

In this chapter, we study the multi-Higgs production in the VBF mode at the LHC and at future proton-proton colliders, focusing on the prospects for measurements at 27 TeV and at 100 TeV. As we have done in Chapter 4, we study the NP effects by using the EFT Lagrangian 3.2. The total cross

51

sections of $pp \to VV \to h$, $pp \to VV \to hh$, and $pp \to VV \to hhh$ are computed numerically, with appropriate VBF cuts for 14 TeV, 27 TeV, and 100 TeV respectively. The results describe the potential for constraining NP in the Higgs sector at the LHC and at future hadron colliders. We also derive theoretical constraints on the parameter space from the unitarity of $2 \to n$ scattering amplitudes and apply the results to $VV \to hh$ and hhh processes. This chapter is based on Ref. [10].

5.1 Constraints on parameters from the unitarity of S matrix

The importance of unitarity in quantum mechanics and quantum field theory has been emphasized in early literature. In the context of relativistic quantum field theory, unitarity is a constraint on the $\mathcal{S}$ operator as the most generic dynamic observable. The basic idea, which is formulated as the optical theorem, and its most elementary application to spin-less $2 \to 2$ scattering are textbook knowledge. However, the concrete formulation for high-energy $2 \to n$ scattering in the context of the SM and its extensions is not as familiar as the $2 \to 2$ case. In this section, we discuss the unitarity conditions without the restriction to elastic scattering, and apply the generic formalism to the processes that we are interested in. Further details of the derivation are given in Appendix B. The goal is to determine energy-dependent constraints on the free parameters of the EFT Lagrangian 3.2.

As introduced in Chapter 3, an EFT with higher-dimensional operators in a local Lagrangian is a method to generate and parameterize a low-energy expansion of the scattering amplitudes for unknown high-energy dynamics. A valid quantum field theory underlying any physics beyond the SM will result in a unitary scattering matrix, but this need not hold for the approximation generated by the corresponding EFT. In fact, a term of dimension d in the Lagrangian generically generates uncancelled factors that are proportional to E^{d-4}, where E is the overall energy scale in a scattering process [120].

The unitarity requirement for a complete $\mathcal{S}$ matrix, evaluated for the set of $m \to n$ scattering amplitudes, relates the forward $n \to n$ elastic scattering amplitude to the interference of all $m \to n$ scattering amplitudes, integrated over phase space. In a simplified treatment where we neglect all $n, m > 2$, we can use angular-momentum conservation to simplify the scattering matrix to a finite $N \times N$ matrix which may be diagonalized in terms of partial-wave amplitudes, cf., e.g., Ref. [121]. This relation implies a strict upper bound on each partial wave, which can be exploited to derive energy-dependent constraints on the parameters of an EFT. For parameter values which violate those constraints, the EFT is invalid as a useful approximation, independent of the true underlying theory.

If we include $2 \to n$ scattering with $n > 2$, we may apply similar methods and obtain comparatively simple constraints if we introduce extra assumptions [122, 123, 124] or neglect spins [125]. Extending these ideas, we consider the generic formalism in its consequences for $VV \to hh$ and $VV \to hhh$, and express the results in the form of inequalities for the EFT parameters.

5.1.1 General unitarity constraints

Unitarity is equivaltent to the conservation of probability in a quantum theory. The scattering of observable particles is described by a $\mathcal{S}$ operator, which satisfies $\mathcal{S}^\dagger \mathcal{S} = 1$. Its nontrivial part is defined by $\mathcal{S} = 1 + i\mathcal{T}$, where the $\mathcal{T}$ satisfies the universal relation

$$-i(\mathcal{T} - \mathcal{T}^\dagger) = \mathcal{T}^\dagger \mathcal{T} \tag{5.1}$$

We are interested in unitarity conditions for matrix elements between asymptotic states which contains a finite number n_a of particles with well-defined masses. We use $|\alpha, \Phi_a\rangle$ to represent a multi-particle state with n_a particles, where Φ_a is a shorthand for the kinematical configuration of n_a on-shell momenta (the phase-space point), and α denotes the set of discrete quantum numbers such as helicity and color. Furthermore, the total momentum of a multi-particle state a is labeled as p_a. With this notation, the manifold of configurations (α, Φ_a) becomes a compact manifold for each fixed n_a.

Because of the momentum conservation, the matrix elements of the scattering amplitude operator $\mathcal{M}$ between the initial state $|\alpha, \Phi_a\rangle$ and the final state $|\beta, \Phi_b\rangle$ can be written as

$$\langle \beta, \Phi_b | \mathcal{T} | \alpha, \Phi_a \rangle = (2\pi)^4 \delta^{(4)}(p_a - p_b) \langle \beta, \Phi_b | \mathcal{M} | \alpha, \Phi_a \rangle. \tag{5.2}$$

We can express the matrix elements of the left-handed side of Eq. (5.1) and insert a complete set of multi-particle states $|\gamma, \Phi_c\rangle$ to the right-handed side, and obtain

$$-i \left[\langle \beta, \Phi_b | \mathcal{M} | \alpha, \Phi_a \rangle - \langle \alpha, \Phi_a | \mathcal{M} | \beta, \Phi_a \rangle^* \right]$$
$$= \sum_\gamma \int \mathrm{d}\Phi_c \, \langle \gamma, \Phi_c | \mathcal{M} | \beta, \Phi_b \rangle^* \langle \gamma, \Phi_c | \mathcal{M} | \alpha, \Phi_a \rangle \tag{5.3}$$

where $\mathrm{d}\Phi_c$ denotes the phase-space element of the intermediate states. The momentum conservation requires $p_c = p_a = p_b$.

For convenience, we introduce a bijective mapping between the unit hypercube in $d_a = 3n_a - 4$ dimensions, $\{x_a \in \mathbb{R}^{d_a}; \ 0 < (x_a)_i < 1\}$ and the manifold $\{\Phi_a\}$, for each fixed n_a. For instance, we may factorize phase space as a tree consisting of $n_a - 1$ momentum splittings of type $1 \to 2$, with p_a at the root. There are $2(n_a - 1)$ angular variables and $n_a - 2$ invariant-mass variables. This mapping introduces a Jacobian $J_a(x_a) = \mathrm{d}\Phi_a/\mathrm{d}x_a$, which should incorporate appropriate symmetry factors. This construction corresponds to a common method of evaluating phase-space integrals. If we introduce amplitude functions which include the Jacobian factors as follows,

$$M_{\beta\alpha}(x_b, x_a) = J_b^{1/2}(x_b) \langle \beta, \Phi_b(x_b) | \mathcal{M} | \alpha, \Phi_a(x_a) \rangle J_a^{1/2}(x_a) \tag{5.4}$$

Eq. (5.1) can be rewritten to

$$-i\left[M^{\beta\alpha*}(x_b, x_a) - M^{\alpha\beta}(x_a, x_b)\right] = \sum_\gamma \int \mathrm{d}x_c\, M^{\gamma\beta*}(x_c, x_b)\, M^{\gamma\alpha}(x_c, x_a) \qquad (5.5)$$

If massless particles are involved, the sum over intermediate states is infinite. The matrix elements contain non-integrable infrared, collinear, and Coulomb singularities, so the integrals do not converge. To deal with this issue, one method is to introduce some version of phase-space slicing and sum over nearly degenerate states, which introduces indefinite particle numbers [126, 127]. However, we are interested in the production of neutral massive bosons. Photons, quarks and gluons are acting as spectators which are treated in standard QED and QCD perturbation theory. We may ignore this complication and assume that all relevant states are massive. The sum over intermediate states then is a finite sum, the matrix elements and the Jacobians are finite, and the integration manifold (the union of the unit hypercubes for all (n_a, α) is compact.

In this case, it is possible to introduce a scalar product of square-integrable functions on the integration manifold and to find a complete basis of functions which are mutually orthonormal with respect to this scalar product. For instance, choosing the canonical scalar product, we could take a straightforward Fourier expansion. A more physical choice could involve spherical harmonics for the normalized angular variables and an arbitrary basis for the invariant-mass variables. In the two-particle case where there are no free invariant masses, it becomes the standard partial-wave expansion. We note that for each particle combination a, we may choose a different kind of expansion for the corresponding phase space $\Phi_a(x_a)$.

For simplicity, we adopt the following canonical scalar product and a corresponding orthonormal basis $\{H_A^\alpha(x_a)\}$ on each α phase space,

$$\int \mathrm{d}x_a\, H_A^{\alpha*}(x_a)\, H_B^\alpha(x_a) = \delta_{AB}, \qquad (5.6)$$

where A is an appropriate (multi-)index which labels the basis functions. The amplitudes can be expanded as

$$M^{\beta\alpha}(x_b, x_a) = 2\sum_{AB} a_{AB}^{\alpha\beta} H_A^\alpha(x_a)\, H_B^{\beta*}(x_b). \qquad (5.7)$$

So the scattering is expressed in terms of an actual matrix with elements $a_{AB}^{\alpha\beta}$. (The factor 2 is introduced for the consistency with the standard two-particle partial-wave expansion.) Explicitly, the coefficients are

$$a_{AB}^{\alpha\beta} = \frac{1}{2}\int \mathrm{d}x_a\, \mathrm{d}x_b\, H_A^{\alpha*}(x_a)\, H_B^\beta(x_b)\, M^{\beta\alpha}(x_b, x_a). \qquad (5.8)$$

They take complex values and depend only on the total momentum, $a_{AB}^{\alpha\beta} = a_{AB}^{\alpha\beta}(p_a)$, where $p_a = p_b$. If we choose a phase-space parameterisation which preserves Lorentz invariance, the coefficients

depend only on $s = p_a^2$.

We now obtain a discrete version of Eq. (5.5) [128, 129]:

$$-i(a_{AB}^{\alpha\beta} - a_{BA}^{\beta\alpha*}) = 2\sum_{\gamma}\sum_{C} a_{AC}^{\alpha\gamma} a_{BC}^{\beta\gamma*}, \tag{5.9}$$

where all coefficients are finite and the sums are convergent if the simplifications regarding massless states are applied, as described above.

Eq. (5.9) decribes all unitarity relations of the scattering matrix in question. To derive constraints on individual amplitudes, we need a positivity condition. We may diagonalize the scattering matrix and obtain exact relations for superpositions of states. Alternatively, we may derive less comprehensive but phenomenologically more useful relations by focusing on diagonal matrix elements, i.e., $\alpha = \beta$ and $A = B$,

$$-i(a_{AA}^{\alpha\alpha} - a_{AA}^{\alpha\alpha*}) = 2\sum_{\gamma}\sum_{C} |a_{AC}^{\alpha\gamma}|^2 \tag{5.10}$$

$$= 2|a_{AA}^{\alpha\alpha}|^2 + 2\sum_{C\neq A} |a_{AC}^{\alpha\alpha}|^2 + 2\sum_{\gamma\neq\alpha}\sum_{C} |a_{AC}^{\alpha\gamma}|^2 \tag{5.11}$$

To cast this in the intuitive geometry of the Argand circle, we rewrite the diagonal amplitude in terms of its real and imaginary parts:

$$|\text{Re}\, a_{AA}^{\alpha\alpha}|^2 + |\text{Im}\, a_{AA}^{\alpha\alpha} - \frac{1}{2}|^2 + \sum_{C\neq A} |a_{AC}^{\alpha\alpha}|^2 + \sum_{\gamma\neq\alpha}\sum_{C} |a_{AC}^{\alpha\gamma}|^2 = \frac{1}{4} \tag{5.12}$$

This means that each complex-valued elastic amplitude $a_{AA}^{\alpha\alpha}(s)$ must lie on a circle with radius r around $i/2$, where the elastic radius $r = 1/2$ is reduced by the total contribution of all inelastic channels.

The exact relation (5.12) yields strict upper bounds for the elastic amplitude as well as for the total inelastic contribution, which trivially translates into a bound for each individual final state in this representation. We obtain

$$
\begin{aligned}
|\text{Re}\, a_{AA}^{\alpha\alpha}|^2 &\leq \frac{1}{4} \\
|\text{Im}\, a_{AA}^{\alpha\alpha} - \frac{1}{2}|^2 &\leq \frac{1}{4} \\
\sum_{C\neq A} |a_{AC}^{\alpha\alpha}|^2 &\leq \frac{1}{4} \\
\sum_{\gamma\neq\alpha}\sum_{C} |a_{AC}^{\alpha\gamma}|^2 &\leq \frac{1}{4}
\end{aligned}
\tag{5.13}
$$

Examples for the application of these bounds, referring also to the treatments in Refs. [121, 122, 123, 125], can be found in Appendix B.

The last inequality in Eq. (5.13) gives the unitarity constraints on inelastic scattering, and we note that it is independent of the basis H^γ. To see this, we define the coefficients $b_A^{\alpha\gamma}$:

$$b_A^{\alpha\gamma} \equiv \frac{1}{4} \int \mathrm{d}x_a \mathrm{d}x_b \mathrm{d}x_c H_A^{\alpha*}(x_a) H_A^{\alpha}(x_b) M^{\gamma\alpha*}(x_c, x_b) M^{\gamma\alpha}(x_c, x_a), \qquad (5.14)$$

which is clearly independent of H^γ. Using the expansion in Eq. (5.7), we find

$$b_A^{\alpha\gamma} = \sum_C |a_{AC}^{\alpha\gamma}|^2 \geq 0 \qquad (5.15)$$

Finally, the unitarity constraint for inelastic scattering can be written as

$$\sum_{\gamma \neq \alpha} b_A^{\alpha\gamma} \leq \frac{1}{4} \qquad (5.16)$$

5.1.2 Unitarity Constraints from $VV \to hh$

In this subsection, we apply the generic formalism to the scattering process $W^+W^- \to hh$. We assume that the on-shell approximation is justified for the purpose of deriving unitarity bounds, which means that incoming vector bosons are on-shell with a pair invariant mass $M(WW) = M(hh) = \hat{s}$. (In the actual process, the incoming propagators are space-like with a virtuality of $O(m_W)$.)

The $W^+W^- \to hh$ scattering is an inelastic channel. As described above, the unitarity bounds can be expressed by b-coefficients

$$b_A^{W^+W^- \to hh}(\hat{s}) \equiv \sum_C |a_{AC}^{W^+W^- \to hh}(\hat{s})|^2 \leq \frac{1}{4}, \qquad (5.17)$$

where A and C are (multi-)indices for the initial-state and final-state basis, respectively. In this process, the initial-state particles carry spin as well as momentum, while the final-state phase space manifold is trivially given by the unit sphere, for fixed energy $\sqrt{\hat{s}}$.
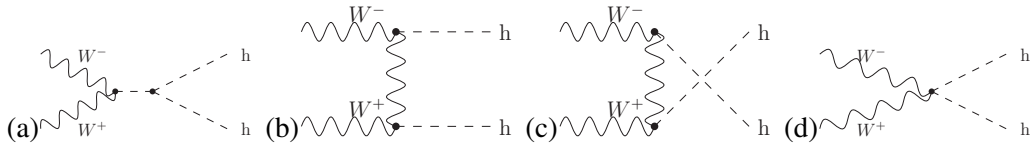
Figure 5.1: Four types of Feynman diagrams are shown which contribute to the processes $W^+W^- \to hh$.

In the SM, there are four Feynman diagrams which contribute to the $W^+W^- \to hh$ process, as shown in Fig. 5.1. So we can seperate the amplitudes to four parts:

$$M(W^+W^- \to hh) = M_s + M_t + M_u + M_4. \qquad (5.18)$$

We refer to these as the s-channel, t-channel, u-channel, and contact-interaction amplitudes, respectively.

In the high energy limit $s \gg m_W^2, m_h^2$, the leading contribution in the EFT is proportional to s. So we expand the amplitudes by the rescaled energy $\sqrt{s/v^2}$ as a dimensionless expansion parameter

$$M(W^+ W^- \to hh) = \sum_{i=0}^{+\infty} m_i (\frac{\sqrt{s}}{v})^{2-i}, \qquad (5.19)$$

where m_i are the coefficients in the expansion. In Table 5.1 we list the prefactors of the leading contribution for each amplitude in one of the four independent helicity modes. The amplitudes of all other helicity modes are related to the four modes in the table. All leading contributions are independent of the kinematics, except the $+-$ of the t/u-channel, so the table entries translate directly into bounds for amplitude coefficients once a suitable basis has been chosen. We also observe that only the $++$, $+-$, and 00 modes lead to amplitudes rising proportional to s, so we may focus on these modes while considering unitarity bounds. For the $+0$ mode, its leading contribution is proportional to $g_{W,a1} g_{W,b1} \sqrt{s/v^2}$. If $g_{W,a1}$ is well constrained via the 00 mode and does not deviate grossly from its SM value, the $+0$ mode leads to a bound on $g_{W,b1}$ which has the same s dependence but is weaker than the constraint that we get from the $+-$ amplitude.

helicity configuration	$++$	$+-$	00	$+0$
s-channel	$\frac{1}{2}\kappa_5 g_{W,b1}$	0	$\frac{1}{2}\kappa_5 g_{W,a1}$	0
t, u-channel	$2g_{W,b1}^2$	$\mathcal{O}(g_{W,b1}^2)$	$-g_{W,a1}^2$	0
contact interaction	$g_{W,b2}$	0	$g_{W,a2}$	0

Table 5.1: The leading energy contribution m_0 in four independent helicity matrix element for $VV \to hh$ are shown. In this table, $\mathcal{O}(g_{W,b2}^2)$ means such contribution is non-zero but depends on phase-space configuration, and proportional to the coupling constants $g_{W,b2}^2$.

Angular-momentum conservation directs the choice of phase-space basis. The final state is described by a straightforward partial-wave expansion. For the initial state, we should couple helicity with orbital angular momentum to total angular momentum j, and adopt the Wigner D-matrix formalism which is introduced in Appendix B. We can derive individual bounds for amplitude coefficients $b_j(h_1 h_2)$,

$$b_j(h_1 h_2) \le \frac{1}{4}, \qquad \text{where } h_i = + - 0. \qquad (5.20)$$

Finally, we obtain the strongest bounds on the EFT parameters:

$$b_0(00) = \frac{s^2}{512\pi^2 v^4}|g_{W,a2} - g_{W,a1}^2 + \frac{1}{2}\kappa_5 g_{W,a1}|^2 \leq \frac{1}{4} \tag{5.21}$$

$$b_0(++) = \frac{s^2}{512\pi^2 v^4}|g_{W,b2} + 2g_{W,b1}^2 + \frac{1}{2}\kappa_5 g_{W,b1}|^2 \leq \frac{1}{4} \tag{5.22}$$

$$b_2(+-) = \frac{s^2}{3072\pi^2 v^4}g_{W,b1}^4 \leq \frac{1}{4} \tag{5.23}$$

In particular, the $+-$ mode gives a bound on $g_{W,b1}$, i.e., the transversal interaction $hW_T^+ W_T^-$, which is independent of the other EFT parameters.

5.1.3   Unitarity Constraints from $VV \to hhh$
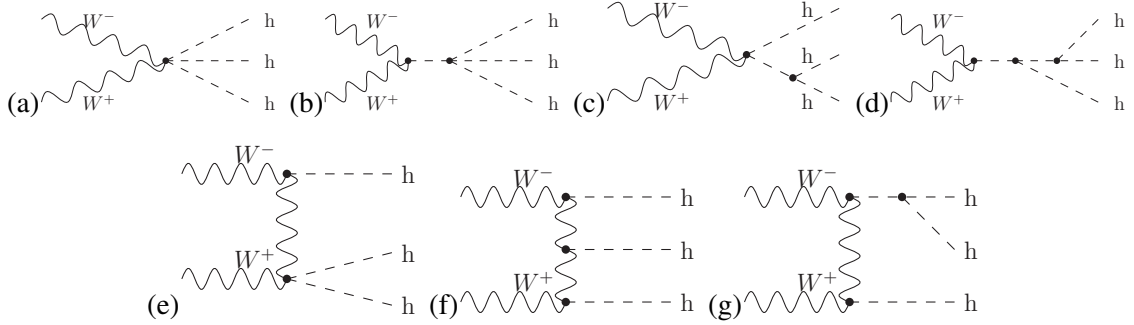
Figure 5.2: Seven types of Feynman diagrams are shown which contribute to the processes $W^+ W^- \to hhh$.

In the SM, the helicity amplitudes of $W^+ W^- \to hhh$ processes correspond to seven types of Feynman diagrams, as shown in Fig. 5.2. Analogy to $W^+ W^- \to hh$, in the high energy limit, the amplitude can be expanded as a series in powers of $\sqrt{s/v^2}$

$$M(W^+ W^- \to hhh) = \sum_{i=0}^{+\infty} m_i v^{-1}(\frac{\sqrt{s}}{v})^{2-i} \tag{5.24}$$

The leading term m_0 are listed in Table 5.2, for each helicity combination. If a coefficient is phase-space dependent, we denote it as $\mathcal{O}(C)$, where C is a combination of the anomalous couplings. Table 5.2 also shows that the $+0$ helicity mode does not contribute to m_0. The unitarity bounds of this mode result from the m_1 terms and are weaker than the remaining ones, as long as $g_{W,a1}, g_{W,a2}, \kappa_5$ are not far from their respective SM values.

Since this is also an inelastic channel, the unitarity bounds on the b-coefficients are

$$b_A^{W^+ W^- \to hhh}(\hat{s}) \leq \frac{1}{4}. \tag{5.25}$$

	++	+−	00	+0
a	$g_{W,b3}$	0	$g_{W,a3}$	0
b	$\frac{1}{2}g_{W,b1}\kappa_6$	0	$\frac{1}{2}g_{W,a1}\kappa_6$	0
c	$\frac{3}{2}g_{W,b2}\kappa_5$	0	$\frac{3}{2}g_{W,a1}\kappa_5$	0
d	$g_{W,b1}\kappa_5^2$	0	$g_{W,a1}\kappa_5^2$	0
e	$6g_{W,b1}g_{W,b2}$	$\mathcal{O}(g_{W,b1}g_{W,b2})$	$-4g_{W,a1}g_{W,b1}$	0
f	$\mathcal{O}(g_{W,b1}^3)$	$\mathcal{O}(g_{W,b1}^3)$	$4g_{W,a1}^3$	0
g	$3g_{W,b1}^2\kappa_5$	$\mathcal{O}(g_{W,b1}^2\kappa_5)$	$-2g_{W,a1}^2\kappa_5$	0

Table 5.2: The leading contribution m_0 at high energy limit for seven types of Feynman diagrams to the amplitudes are tabulated.

The b-coefficients are independent of the phase-space parameterisation and the basis functions for the triple-Higgs system, and only depend on the phase-space parameterisation and the basis functions for the W-boson pair. As discussed in Appendix B, after choosing the Wigner D-matrix as the basis for the W^+W^- state, the b-coefficients are diagonal. We can denoted them as $b_j(h_1 h_2)$, where j represents the total angular momentum, and $h_i = + - 0$ are the helicities of the two W bosons. We calculate the (reduced) b-coefficients directly by using Eq. (5.14). Although the result is independent of the phase-space parameterisation for the triple-Higgs system, an explicit expression is required for phase-space integration. We adopt the form given in App. B.4. We give the results for the three helicity modes below:

1. For the 00 helicity mode, the amplitude is independent of phase-space parameters. The optimal choice is given in Appendix B. Since the initial state is a two-particles state, the Wigner D-matrix as a basis yields this optimal bound,

$$b_0(00) = \frac{s^3}{49152\pi^4 v^6}|g_{W,a3} + \frac{1}{2}g_{W,a1}\kappa_6 + \frac{3}{2}g_{W,a2}\kappa_5 + g_{W,a1}\kappa_5^2$$
$$- 4g_{W,a1}g_{W,a2} + 4g_{W,a1}^3 - 2g_{W,a1}^2\kappa_5|^2 \le \frac{1}{4} \tag{5.26}$$

2. For the ++ helicity mode, the type-f contribution is phase-space dependent, and it yields a non-zero b_j for $j > 0$. However, we have checked that the dependence is of minor importance, and the bounds from $b_j \le \frac{1}{4}$ with $j > 0$ turn out to be much weaker than the bounds from $W^+W^- \to hh$. Therefore, we only consider the bound on b_0,

$$b_0(++) = \frac{s^3}{49152\pi^4 v^6}(|g_{W,b3} + \frac{1}{2}g_{W,b1}\kappa_6 + \frac{3}{2}g_{W,b2}\kappa_5 + g_{W,b1}\kappa_5^2$$
$$+ 6g_{W,b1}g_{W,b2} + f_1 g_{W,b1}^3 - 3g_{W,b1}^2\kappa_5|^2 + f_2 g_{W,b1}^6) \le \frac{1}{4} \tag{5.27}$$

where $f_1 = 7.49994 \pm 0.00005$ and $f_2 = 0.0658 \pm 0.0006$ are computed by numerical integration. The negligible f_2 reflects the fact that the dependence of $g_{W,b1}^3$ on phase-space is

Cuts	$\sqrt{s} = 14$ TeV	$\sqrt{s} = 27$ TeV	$\sqrt{s} = 100$ TeV
$P_t(j)$	> 20 GeV	> 20 GeV	> 30 GeV
$\Delta R(j,j)$	> 0.8	> 0.8	> 0.8
$|\eta(j)|$	< 5.0	< 5.0	< 8.0
$\Delta\eta(j,j)$	> 3.6	> 3.6	> 4.0
$M(j,j)$	> 500 GeV	> 500 GeV	> 800 GeV

Table 5.3: Acceptance cuts used for the calculation of VBF Higgs production in pp collision (VBF cuts), for three different collider energies.

small.

3. For the $+-$ helicity mode, only b_j with $j = 2, 4, \ldots$ are non-zero, and the leading term is b_2, which is given by

$$b_2(+-) = \frac{s^3}{49152\sqrt{6}\pi^4 v^6} \left| g_{W,b1} g_{W,b2} + 2g_{W,b1}^3 + \frac{1}{2} g_{W,b1}^2 \kappa_5 \right|^2 \leq \frac{1}{4} \qquad (5.28)$$

5.2 Multi-Higgs production via VBF processes with dimension-6 operators

To investigate the sensitivity of LHC and future colliders to NP effects in multi-Higgs production, we compute the cross sections for the processes $pp \to hhjj$ and $pp \to hhhjj$ including the full dependence on the parameters in Lagrangian 3.2. To extract the VBF contribution and suppress the $Z \to jj$ contribution, we apply standard VBF cuts, which are listed in Table (5.3). We compute results for the pp collider with c.m. energy 14 TeV LHC (the HL-LHC), 27 TeV (the HE-LHC), and 100 TeV.

For the numerical calculations, we implement the Lagrangian 3.2 to automatic Monte-Carlo integration and simulation packages WHIZARD 2.3 [7] and Madgraph 5 [8]. On one hand, we construct an appropriate UFO file and interface it with Madgraph 5. On the other hand, since WHIZARD does not support five-point vertices of the form needed for the EFT calculation, we introduced an auxiliary field S with a Lagrangian

$$\mathcal{L}_S = \frac{1}{2}(\partial_\mu S)^2 - \frac{1}{2}M^2 S^2 - g_{Shhh}(\partial^2 S)h^3 + g_{w,a3}\frac{2m_W^2}{v^3}SW^\mu W_\mu - \frac{g_{w,b3}}{v^3}SW^{\mu\nu}W_\mu \quad (5.29)$$

So S only couple to triple-Higgs or W pair, and a Feynman diagram as shown in Fig. 5.3 contributes to the triple Higgs production process. When $M = 0$ and $g_{Shhh} = -1$, $g_{w,a3}$ and $g_{w,b3}$ become equivalent to the parameters in Eq. 3.2, and the resulting amplitude expression is identical to the one that follows from using (3.2) directly. We have cross-checked numerical results from both imple-

Process	$\sigma(14\text{TeV})$ [fb]	$\sigma(27\text{TeV})$ [fb]	$\sigma(100\text{TeV})$ [fb]
$pp \to hjj$	1.64×10^3	4.87×10^3	2.60×10^4
$pp \to hhjj$	1.10	4.32	41.2
$pp \to hhhjj$	2.73×10^{-4}	1.73×10^{-3}	4.50×10^{-2}

Table 5.4: SM values for the cross sections of the processes $pp \to hjj$, $pp \to hhjj$ and $pp \to hhhjj$ with VBF cuts, at three different collider energies.

mentations against each other. As another cross-check, we have validated selected results against the package VBFNLO [78, 79], with good agreement.
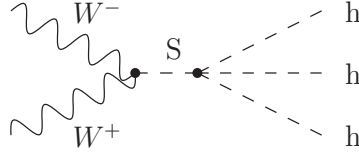
Figure 5.3: Triple-Higgs production diagram with a five-point vertex $WWhhh$ effectively generated by an auxiliary field S.

For the pure SM, the cross sections after VBF cuts are listed in Table 5.4. All numerical results are computed at leading order in the strong and electroweak perturbative expansions.

It is expected that the $q \to Wq'$ splitting force the remnant jets in VBF process to a back-to-back configuration, with high energy and moment. The VBF cuts in Table 5.3 can select the events in this region and reject the jets from Z decay. Due to the finite mass of the vector bosons, the VBF contribution is maximised for transverse momenta of the order of the W mass. In the numerical calculation, we apply cut $P_t(j) > 20$ GeV for 14 and 27 TeV, and 30 GeV for 100 TeV, respectively.

Regarding the transition from LHC kinematics to a 100 TeV collider, our numerical results show that the forward jets can acquire significantly larger rapidity than that at LHC (Fig. 5.4). Simularly, the produced Higgs bosons are distributed over a broader η range (Fig. 5.5). Therefore, we assume a better rapidity coverage for the detector at 100 TeV and have adapted our cuts in Table 5.3 accordingly.

5.2.1 Higgs pair production

For the on-shell process $W^+W^- \to hh$, we can express the amplitude by the EFT parameters

$$\mathcal{M}(W^+W^- \to hh) = \mathcal{M}_s + \mathcal{M}_t + \mathcal{M}_u + \mathcal{M}_4 , \tag{5.30}$$

$$\mathcal{M}_s = S_1 g_{W,a1}\lambda_3 + S_2 g_{w,b1}\lambda_3 + S_3 g_{W,a1}\kappa_5 + S_4 g_{W,b1}\kappa_5 , \tag{5.31}$$

$$\mathcal{M}_t = T_1 g_{W,a1}^2 + T_2 g_{W,a1}g_{W,b1} + T_3 g_{W,b1}^2 , \tag{5.32}$$

$$\mathcal{M}_u = U_1 g_{W,a1}^2 + U_2 g_{W,a1}g_{W,b1} + U_3 g_{W,b1}^2 , \tag{5.33}$$

$$\mathcal{M}_4 = X_1 g_{W,a2} + X_2 g_{W,b2} , \tag{5.34}$$
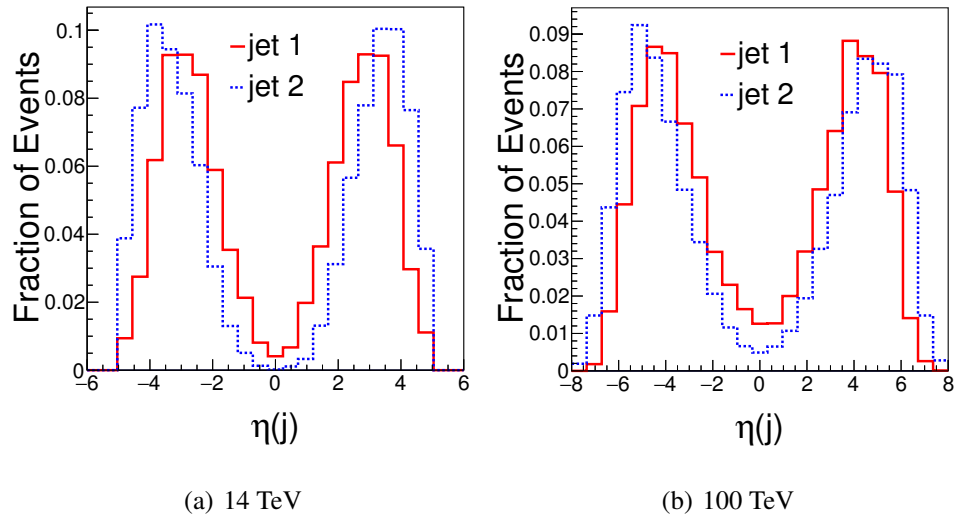
(a) 14 TeV

(b) 100 TeV

Figure 5.4: Rapidity distribution (η) of the forward tagging jets at (a) 14 TeV and (b) 100 TeV. Jet 1 (2) labels the harder (softer) jet, respectively.
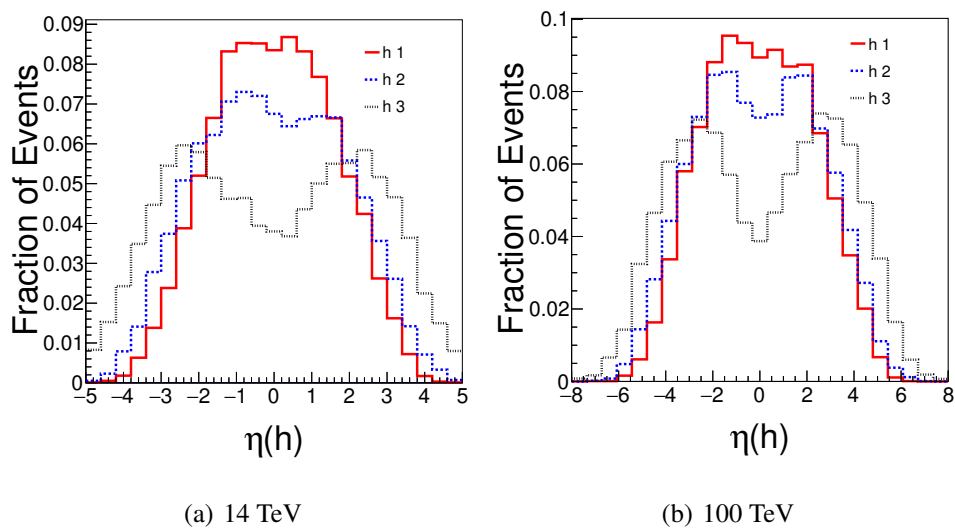
(a) 14 TeV

(b) 100 TeV

Figure 5.5: Rapidity distribution (η) of the Higgs bosons at (a) 14 TeV and (b) 100 TeV. h 1, 2, 3 labels the Higgs particles from hardest to softest one.

Where we have used the breakdown in terms of 4 types of Feynman diagrams in Fig. 5.1. The coefficients S_i, T_i, U_i, and X_i describe the expansion in terms of anomalous couplings. They include the SM parts and account for the polarisation wave functions of vector bosons, external momenta, propagators of internal particles, and the SM interactions.

The full process $pp \rightarrow hhjj$ can be expande by a similar way, with new coefficients which incorporate the integration over the PDF of incoming partons and the complete phase space for off-shell intermediate vector bosons. The total cross section can be written as

$$\sigma(pp \rightarrow VVjj \rightarrow hhjj) = \sum_i F_i^{hh} A^{i,hh} \, , \tag{5.35}$$

where $A^{i,hh}$ denotes second-order polynomials of the parameters $g_{V,a1}$, $g_{V,b1}$, λ_3, κ_5, $g_{V,a2}$ and $g_{V,b2}$. The prefactors F_i^{hh} are the integrated form factors and can be computed numerically.

To simplify the expression, we consider the phenomenological information from expected precision data. For the WWh vertex, it should be strongly constrained by data from the Higgs decay to WW as well as VBF single-Higgs production. Higgs factories such as the CEPC, the ILC, or the CLIC collider allow for an absolute model-independent measurement of the WWh interaction with high precision. With this expectation we can fix $g_{W,a1}$ and $g_{W,b1}$ to their SM values. Furthermore, we assume the custodial-symmetry relations $g_{W,a_2} = g_{Z,a_2}$ and $g_{W,b_2} = g_{Z,b_2}$ whenever contributions of Z boson are considered. Finally, we can express the cross section as

$$\begin{aligned} \sigma(pp \rightarrow hhjj) \quad = \quad & K_0 + K_1 g_{W,a2} + K_2 g_{W,a2}^2 + K_3 g_{W,b2} + K_4 g_{W,a2} g_{W,b2} + K_5 g_{W,b2}^2 \\ & + K_6 \kappa_5 + K_7 g_{W,a2} \kappa_5 + K_8 g_{W,b2} \kappa_5 + K_9 \kappa_5^2 + K_{10} \lambda_3 \\ & + K_{11} g_{W,a2} \lambda_3 + K_{12} g_{W,b2} \lambda_3 + K_{13} \kappa_5 \lambda_3 + K_{14} \lambda_3^2 \end{aligned} \tag{5.36}$$

In Chapter 4, we know that the parameters λ_3 and κ_5 are accessible in the ggF process $gg \rightarrow hh$, which may be measured with greater precision than the VBF mode. In fact, VBF data will primarily constrain $g_{W,a2}$ and $g_{W,b2}$, i.e., the anomalous contact interactions of a longitudinal or transversal W pair with a Higgs pair, respectively. The numerical calculation has been performed with Madgraph 5, and the results of the coefficients $K_0 - K_{14}$ are listed in Table 5.5.

By using the cross section expression (5.36), we can derive the bounds on the EFT parameters which can be achieved at the LHC and a future hadron collider. Fig. 5.6 shows the dependence of the cross section on the two parameters $g_{W,a2}$ and $g_{W,b2}$, respectively, for energy of 14 TeV, 27 TeV, and 100 TeV. One parameter is varied at a time, while the other parameters are set to their SM value. The SM value is marked in each plot, and it is close to the minimum of the cross section in all cases. In the LHC (HE-LHC) plots, the horizontal lines indicate cross section values 10 fb and 30 fb (5/15 fb), respectively. These values may be expected as realistic bounds if no signal is observed. In the 100 TeV plots, we show the bounds that result from constraining the cross section to ± 10 %. (This is a conservative estimate; the study in Ref. [113] argues that a precision of 1% could be achieved.)

	K_0	K_1	K_2	K_3	K_4	K_5	K_6	K_7
14 TeV	23.37	-33.33	12.68	-0.88	1.97	106.8	-19.73	14.65
27 TeV	109.1	- 167.2	68.1	-5.27	10.5	1135.2	-94.96	74.48
100 TeV	1760	-3085	1401	-35.75	108.5	54070	-1630	1461

	K_8	K_9	K_{10}	K_{11}	K_{12}	K_{13}	K_{14}	
14 TeV	1.16	4.27	-6.39	4.00	0.43	2.70	0.73	
27 TeV	7.32	19.40	-23.4	14.99	1.74	10.04	2.61	
100 TeV	71.2	384.6	-175.1	121.2	10.33	76.91	16.3	

Table 5.5: Coefficients $K_0 - K_{14}$ (in fb) in the expression (5.36) for $pp \rightarrow hhjj$ at three different collider energies.

The sensitivity to NP results from putting upper bounds on the cross section. It is clearly that the sensitivity increases considerably between the LHC and the HE-LHC. At 100 TeV, we expect this process can be measured within the SM region.

The unitarity bounds for these parameters are shown on the horizontal axis, for each plot. We have chosen the values 3 TeV, 5 TeV, and 14.5 TeV for the effective energy value that enters the inequalities (5.26-5.27), and apply to a collider energy of 14 TeV, 27 TeV, and 100 TeV, respectively. It is expected that the cross section of any realistis model curves outside those bounds will flatten out in order to remain consistent with the optical theorem. This constraining the cross section is not meaningful unless the experimental resolution reaches a certain threshold. Clearly, we can obtain a crude estimation for the unitarity bounds by inserting a fixed cutoff value Λ. An appropriate framework for dealing with this problem has been described in Refs. [96, 130, 131].

In Fig. 5.7, we show projections for the correlated bounds in planes g_{W,a_2}-g_{W,b_2} and g_{W,a_2}-λ_3. The measurement of double-Higgs production in VBF mode at the 14 TeV LHC can determine g_{W,a_2} and g_{W,b_2} with similar precision, while the parameter λ_3 is only weakly constrained. Increasing the energy to 27 TeV and to 100 TeV, the precision improves as expected. The gain in sensitivity is particularly striking for g_{W,b_2}. This property is evident from the huge value of K_5 in Table 5.5. We note that g_{W,b_2} contributes to the coupling of a Higgs pair to transversal W gauge bosons. The emission of W bosons with transverse polarization from jets is unsuppressed at asymptotic energy, while the coupling to longitudinally polarized Ws involves a W mass-mixing interaction and therefore becomes subleading.

The ultimate precision on the parameters depends on the detector power and the experimental analysis, which we do not discuss the details in this context. For $g_{W,a2}$ and $g_{W,b2}$, we can read off that the sensitivities are ± 10 % from Fig. 5.7. If a boosted-Higgs analysis can constrain the cross section to ± 3 fb and thus $g_{W,a2}$ to 1 % precision [113], a constraint on $g_{W,b2}$ of the order ± 0.008 can be obtained analogously. This is within the range of the loop-induced interaction strength for this vertex.

The numerical results also reflect the strong gauge cancellation which occurs between individual terms of Eq. (5.36) in the SM limit. Some of coefficients K_i, such as K_1, K_2, K_3, are one order of
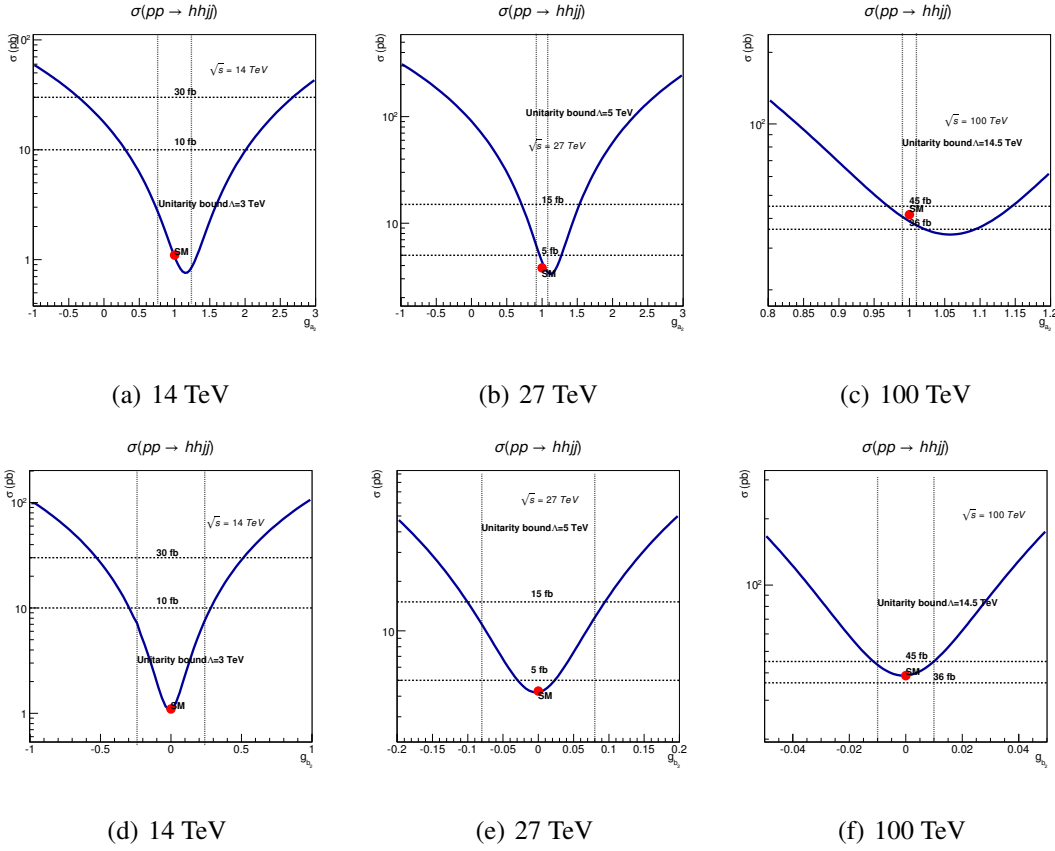
Figure 5.6: Total cross section after VBF cuts for the process $pp \to hhjj$ as a function of the $WWhh$ couplings g_{a_2} (upper row) and g_{b_2} (lower row), for three different collider energies. The vertical lines are unitarity bounds, which are derived from Eqs. (5.26-5.27) by inserting a specific value for the UV cutoff Λ_{UV} as marked in the figures.

magnitude larger than the cross section in the SM. Furthermore, in our conventions, all linear terms, i.e. terms $K_1 \, g_{W,a_2}$, $K_3 g_{W,b_3}$, $K_6 \kappa_5$, and $K_{10} \lambda_3$, are negative. The sign of these interference terms is retained when the collision energy increases from 14 TeV to 100 TeV.
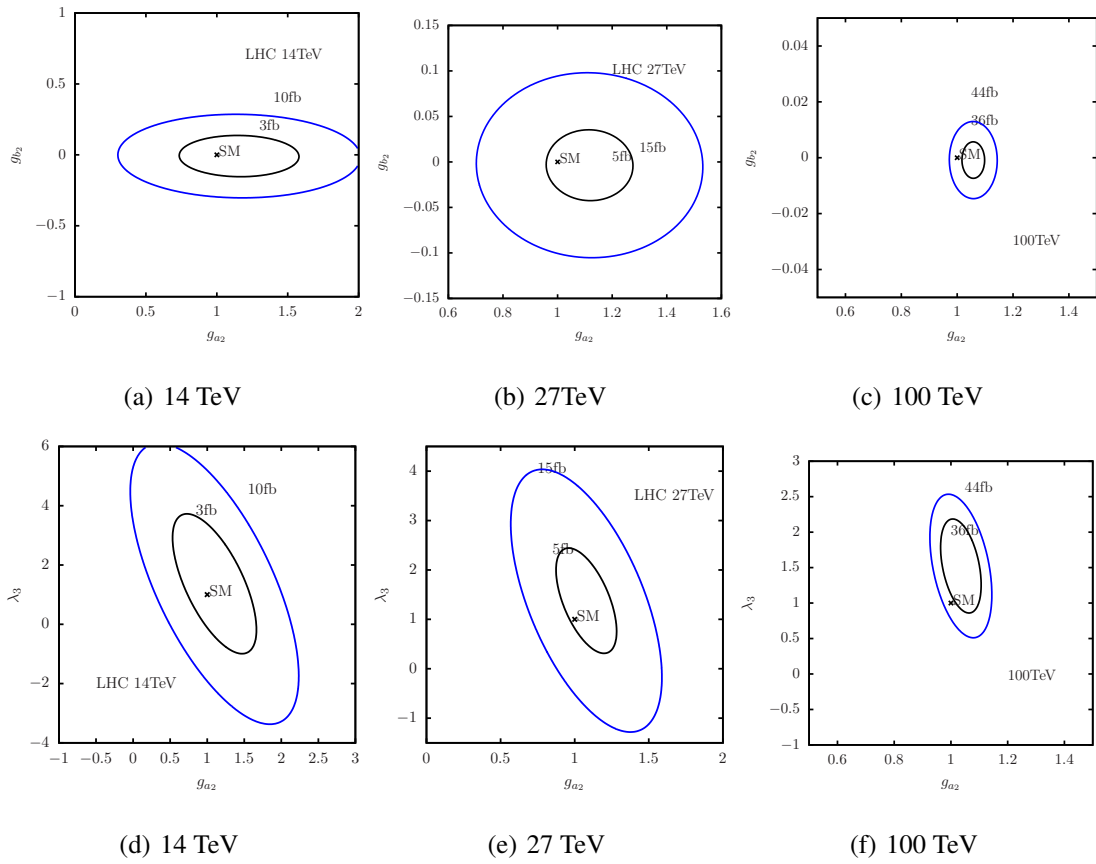
Figure 5.7: Projections for correlated bounds in the planes g_{a_2}-g_{b_2}, g_{a_2}-λ_3, from the process $pp \rightarrow hhjj$ at three different collider energies.

5.2.2 Triple Higgs production

For the $hhhjj$ final state, the breakdown of the amplitude in terms of Feynman diagrams, Fig. 5.2, is expressed as:

$$\mathcal{M}(W^+W^- \to hhh) = \mathcal{M}_1 + \mathcal{M}_2 + \mathcal{M}_3 + \mathcal{M}_4 + \mathcal{M}_5 + \mathcal{M}_6 + \mathcal{M}_7 \tag{5.37}$$

$$\mathcal{M}_1 = A_1 g_{W,a1} \lambda_3^2 + A_2 g_{W,a1} \lambda_3 \kappa_5 + A_3 g_{W,a1} \kappa_5^2 + A_4 g_{W,b1} \lambda_3^2$$
$$+ A_5 g_{W,b1} \lambda_3 \kappa_5 + A_6 g_{W,b1} \kappa_5^2 \tag{5.38}$$

$$\mathcal{M}_2 = B_1 g_{W,a1} \lambda_4 + B_2 g_{W,a1} \kappa_6 + B_3 g_{W,b1} \lambda_4 + B_4 g_{W,b1} \kappa_6 , \tag{5.39}$$

$$\mathcal{M}_3 = C_1 g_{W,a2} \lambda_3 + C_2 g_{W,a2} \kappa_5 + C_3 g_{W,b2} \lambda_3 + C_4 g_{W,b2} \kappa_5 \tag{5.40}$$

$$\mathcal{M}_4 = D_1 g_{W,a1}^2 \lambda_3 + D_2 g_{W,a1}^2 \kappa_5 + D_3 g_{W,a1} g_{W,b1} \lambda_3$$
$$+ D_4 g_{W,a1} g_{W,b1} \kappa_5 + D_5 g_{W,b1}^2 \lambda_3 + D_6 g_{W,b1}^2 \kappa_5 \tag{5.41}$$

$$\mathcal{M}_5 = E_1 g_{W,a1} g_{W,a2} + E_2 g_{W,a1} g_{W,b2}$$
$$+ E_3 g_{W,a2} g_{W,b1} + E_4 g_{W,b2} g_{W,b1} \tag{5.42}$$

$$\mathcal{M}_6 = F_1 g_{W,a1}^3 + F_2 g_{W,a1}^2 g_{W,b1} + F_3 g_{W,a1} g_{W,b1}^2 + F_4 g_{W,b1}^3 \tag{5.43}$$

$$\mathcal{M}_7 = G_1 g_{W,a3} + G_2 g_{W,b3} \tag{5.44}$$

As we have done for double-Higgs production process, the cross section of the full process $pp \to VVjj \to hhhjj$ can be expressed as

$$\sigma(pp \to VVjj \to hhhjj) = \sum_i F_i^{hhh} A^{i,hhh}. \tag{5.45}$$

To simplify the analysis, we assume that $g_{W,a1}, g_{W,a2}, \lambda_3$ and $g_{W,b1}, g_{W_b2}, \kappa_5$ are known from the measurements of single-Higgs and double-Higgs production to sufficient precision. We set their values to their SM values within this section. Considering the parameters that only contribute to triple-Higgs process, the cross section of the full process can be parameterized as

$$\sigma(pp \to VVjj \to hhhjj) = C_0 + C_1 g_{W,a3} + C_2 g_{W,a3}^2 + C_3 g_{W,b3} + C_4 g_{W,a3} g_{W,b3} + C_5 g_{W,b3}^2$$
$$+ C_6 \kappa_6 + C_7 g_{W,a3} \kappa_6 + C_8 g_{W,b3} \kappa_6 + C_9 \kappa_6^2 + C_{10} \lambda_4$$
$$+ C_{11} g_{W,a3} \lambda_4 + C_{12} g_{W,b3} \lambda_4 + C_{13} \kappa_6 \lambda_4 + C_{14} \lambda_4^2 \tag{5.46}$$

The coefficients C_i are computed numerically by WHIZARD. The results are listed in Table 5.6.

The numerical results allow us to derive the projected bounds on these parameters. The dependence of the cross section on g_{W,a_3} and g_{W,b_3} are shown in Fig. 5.8, for the 100 TeV collider. For reference, these plots also include the unitarity bounds derived from Eqs. (5.26-5.27), by choosing an effective energy of $s = \Lambda^2 = (9 \text{ TeV})^2$. Since the SM cross section of the triple-Higgs process $pp \to hhhjj$ is very small (4.50×10^{-2} fb), experimental data may not provide a measurement, but an upper bound on the cross section, as well as exclusion limits for the anomalous couplings, should
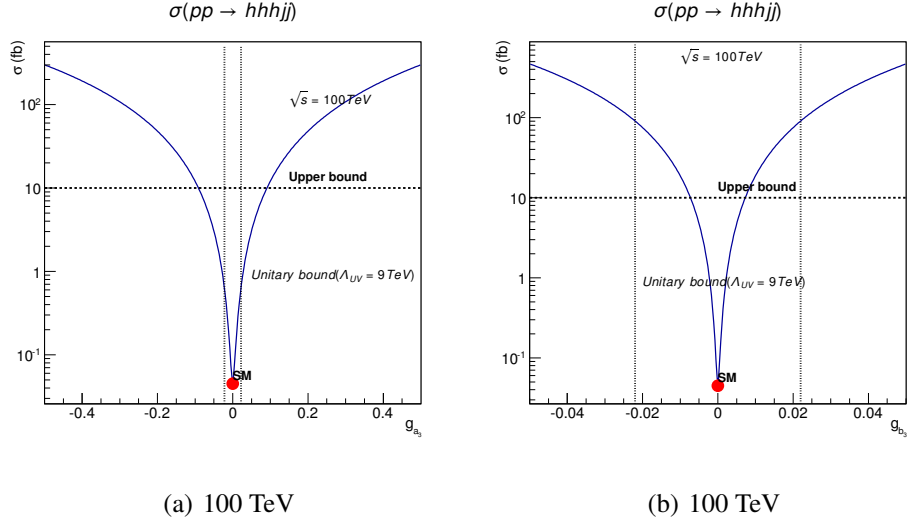
(a) 100 TeV　　　　　　　　　　　(b) 100 TeV

Figure 5.8: Total cross section after VBF cuts for the process $pp \rightarrow hhhjj$ as a function of the $WWhhh$ couplings g_{a_3} and g_{b_3}, for a 100 TeV collider. The vertical lines are unitarity bounds, which are derived from Eqs. (5.26-5.27) by assuming the UV cutoff $\Lambda_{UV} = 9$ TeV.

	C_0	C_1	C_2	C_3	C_4
14 TeV	6.18×10^{-4}	-9.42×10^{-3}	1.99×10^{-1}	-6.57×10^{-4}	2.11×10^{-2}
27 TeV	3.29×10^{-3}	-7.44×10^{-2}	2.974	-1.57×10^{-2}	3.02×10^{-1}
100 TeV	4.26×10^{-2}	-1.74	6.01×10^{2}	-1.96	1.09×10^{2}
	C_5	C_6	C_7	C_8	C_9
14 TeV	4.80	-5.18×10^{-3}	2.05×10^{-1}	1.15×10^{-2}	5.30×10^{-2}
27 TeV	1.74×10^{2}	-3.92×10^{-2}	3.02	2.09×10^{-1}	7.66×10^{-1}
100 TeV	9.36×10^{4}	-1.13	6.08×10^{2}	1.82×10^{1}	1.53×10^{2}
	C_{10}	C_{11}	C_{12}	C_{13}	C_{14}
14 TeV	-6.19×10^{-4}	9.38×10^{-3}	5.91×10^{-4}	5.03×10^{-2}	2.60×10^{-4}
27 TeV	-2.99×10^{-3}	6.44×10^{-2}	8.99×10^{-3}	3.38×10^{-2}	1.23×10^{-3}
100 TeV	-3.33×10^{-2}	1.88	1.29	9.75×10^{-1}	1.47×10^{-2}

Table 5.6: Coefficients $C_0 - C_{14}$ (in fb) in the expression (5.46) for the process $pp \rightarrow hhhjj$ at three different collider energies.

be obtained. Assuming an experimental sensitivity to a cross section of 10 fb, it is found that in the 00 mode, the result already exceeds the unitarity bound for the chosen effective energy. The measurement of triple-Higgs production process may not give meaningful constraint on $g_{W,a3}$. By contrast, for the ++ mode which probes the parameter $g_{W,b3}$, the measurement can provide a constraint. As discussed above, a more quantitative statement near the margin of unitarity saturation would require leaving the straightforward EFT approximation [96, 130, 131]. This is beyond the scope of the present study.

EFT projections for correlated bounds in terms of g_{W,a_3}-g_{W,b_3} and g_{W,a_3}-λ_4 can be found in Fig. 5.9. Obviously, the coupling to transversal W bosons g_{W,b_3} can be constrained more strongly than the other couplings. The reason is that the numerical result of C_5 in Table (5.6) is around 20 times larger than C_2, and C_2 is around 4 times larger. As described in the double-Higgs case, the emission of transverse gauge bosons from the incoming partons at high energy is unsuppressed. In fact, comparing the 14 TeV LHC to a 100 TeV collider, the enhancement factors of the coefficients of C_5 and C_9 are 2×10^4 and 3×10^3, respectively. The leading on-shell amplitudes grow proportional to s^3, eqs. (5.26-5.27). The terms that depend on λ_4 are subleading.

For a sensitivity limit of 10 fb at 100 TeV, Fig. 5.9(c) and Fig. 5.9(d) show that the parameter g_{W,b_3} can be bounded to around 2%, while g_{W,a_3} is constrained to around 20%. This has to be understood with the caveat of unitarity constraints, as discussed above. The parameter λ_4 is also constrained in Fig. 5.9(d), but this constraint is not expected to be improve on the measurement of $gg \to hhh$. For 27 TeV, the expected bounds are accordingly weaker.

5.2.3 Multi-Higgs boson production with a strongly-interacting Higgs sector

In the previous sections, we assume that the parameters in Eq. 3.2 can be determined precisely, and their values are close to the SM predictions. We can derive the bounds on models with strongly-interacting Higgs sector.

Composite Higgs models allow the hVV couplings ($g_{W,a1}$ and $g_{W,a2}$) and the Higgs self-couplings (λ_3, λ_4) deviate from their SM values sizablely. In this subsection, we consider a model where these couplings take arbitrary values, but the other parameters are fixed to their respective SM values, $g_{a_3} = g_{b_1} = g_{b_2} = g_{b_3} = \xi_5 = \xi_6 = 0$, to simplify the interpretation. Data from the measurements of multi-Higgs production can be a supplementary to the Higgs property obtained from lower-order processes. This model corresponds to the truncated EFT in the SILH Lagrangian (3.9), without restricting the parameters to small values. The Higgs inflation model which is introduced in Sec. 3.3 leads to an effective model of this class.

The tree-level cross section for $pp \to hhjj$ is parameterized as

$$
\begin{aligned}
\sigma(pp \to VVjj \to hhjj) &= D_0 g_{W,a1}^4 + D_1 g_{W,a1}^2 g_{W,a2} + D_2 g_{W,a2}^2 \\
&+ D_3 g_{W,a1}^3 \lambda_3 + D_4 g_{W,a1} g_{W,a2} \lambda_3 \\
&+ D_5 g_{W,a1}^2 \lambda_3^2,
\end{aligned} \tag{5.47}
$$

where D_i can be computed numerically, and we have made use of the structure of the tree-level amplitude to limit the powers of the couplings that can appear.

(a) 27 TeV

(b) 27 TeV
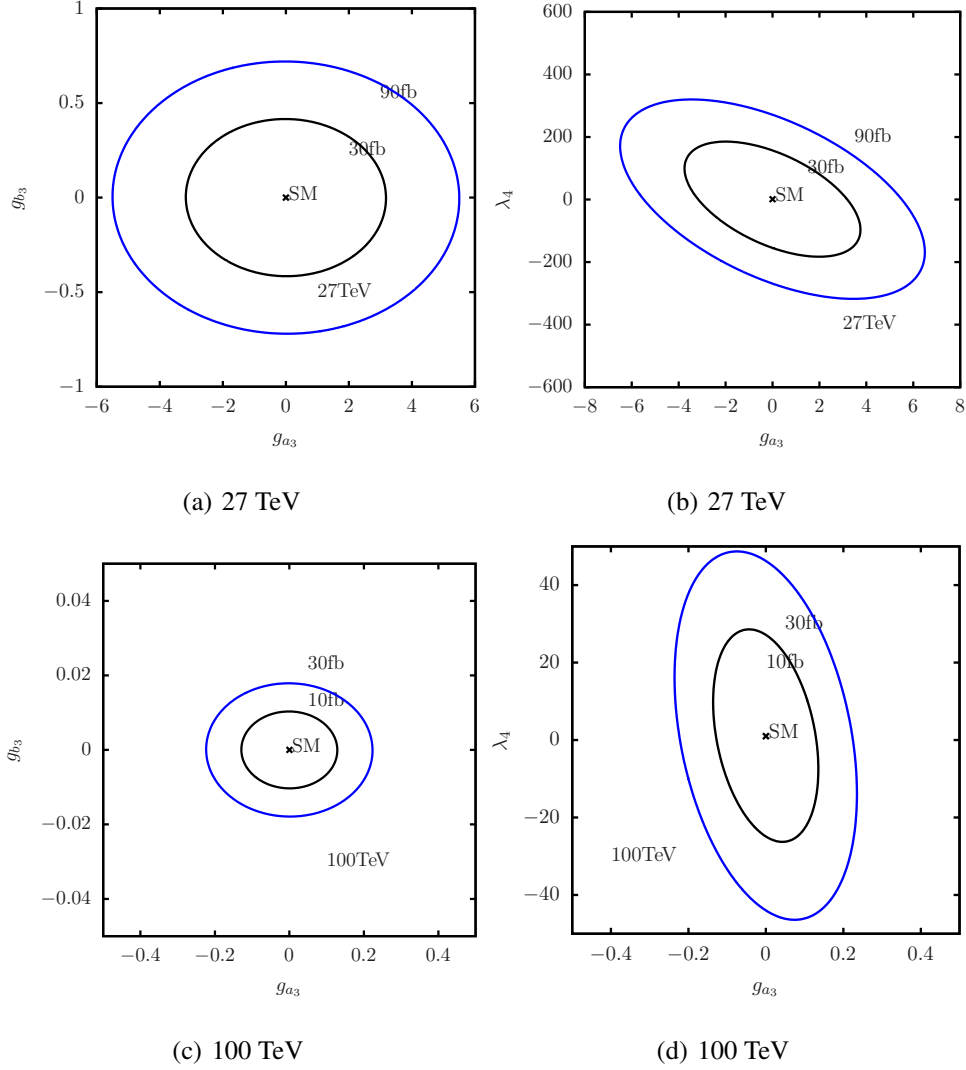
(c) 100 TeV

(d) 100 TeV

Figure 5.9: Projections for correlated bounds in the planes g_{a_3}-g_{b_3}, g_{a_3}-λ_4, from the process $pp \to hhhjj$ at 27 TeV and 100 TeV colliders.

Similarly, the cross section for $pp \to hhhjj$ is parameterized as

$$
\begin{aligned}
\sigma(pp \to VVjj \to hhhjj) = \ & T_0 g_{W,a1}^6 + T_1 g_{W,a1}^4 g_{W,a2} + T_2 g_{W,a1}^2 g_{W,a2}^2 \\
& + \ T_3 g_{W,a1}^5 \lambda_3 + T_4 g_{W,a1}^3 g_{W,a2} \lambda_3 + T_5 g_{W,a1} g_{W,a2}^2 \lambda_3 \\
& + \ T_6 g_{W,a1}^4 \lambda_3^2 + T_7 g_{W,a1}^2 g_{W,a2} \lambda_3^2 + T_8 g_{W,a2}^2 \lambda_3^2 \\
& + \ T_9 g_{W,a1}^3 \lambda_3^3 + T_{10} g_{W,a1} g_{W,a2} \lambda_3^3 \\
& + \ T_{11} g_{W,a1}^2 \lambda_3^4 \\
& + \ T_{12} g_{W,a1}^4 \lambda_4 + T_{13} g_{W,a1}^2 g_{W,a2} \lambda_4 \\
& + \ T_{14} g_{W,a1}^3 \lambda_3 \lambda_4 + T_{15} g_{W,a1} g_{W,a2} \lambda_3 \lambda_4 \\
& + \ T_{16} g_{W,a1}^2 \lambda_3^2 \lambda_4 \\
& + \ T_{17} g_{W,a1}^2 \lambda_4^2 \ .
\end{aligned}
\tag{5.48}
$$

As before, the coefficients D_i and T_i are computed numerically by WHIZARD. The results are list in Table 5.7 and Table 5.8, respectively. The numerical values are large and rise rapidly with energy. In Table 5.7, we observe a cancellation among D_0, D_1, and D_2. These coefficients are independent of λ_3. Another cancellation occurs between D_3 and D_4. Cancellations between terms also occur in Table 5.8. In the SM limit, all terms proportional to positive powers of s must be vanish.

To eliminate such partial cancellations, we choose another method to parameterize the cross section. Defining $\delta g_2 = \frac{g_2}{g_1^2} - 1$, we can express the cross section in the following form

$$
\begin{aligned}
\sigma(pp \to VVjj \to hhhjj) &= g_{W,a1}^6(T_0' + T_1'\delta g_{W,a2} + T_2\delta g_{W,a2}^2) \\
&+ g_{W,a1}^5\lambda_3(T_3' + T_4'\delta g_{W,a2} + T_5\delta g_{W,a2}^2) \\
&+ g_{W,a1}^4\lambda_3^2(T_6' + T_7'\delta g_{W,a2} + T_8\delta g_{W,a2}^2) \\
&+ g_{W,a1}^3\lambda_3^3(T_9' + T_{10}\delta g_{W,a2}) \\
&+ g_{W,a1}^2\lambda_3^4 T_{11} \\
&+ g_{W,a1}^4\lambda_4(T_{12}' + T_{13}\delta g_{W,a2}) \\
&+ g_{W,a1}^3\lambda_3\lambda_4(T_{14}' + T_{15}\delta g_{W,a2}) \\
&+ g_{W,a1}^2\lambda_3^2\lambda_4 T_{16} \\
&+ g_{W,a1}^2\lambda_4^2 T_{17} \ .
\end{aligned}
\tag{5.49}
$$

It is not necessary to assume the δg values to be small.

The numerical results of the primed coefficients are given in Table 5.9. The cancellations that we absorb by redefining the coefficients are numerically relevant. Cancellation that occur between (T_0, T_1, T_2) yields T_0', while the cancellation between (T_1, T_2) yields T_1'. At the energy of the LHC, the original coefficient T_2 is 8×10^2 larger than T_0'. At 100 TeV collider, the cancellation removes a factor of 4.5×10^4, due to the s^3 enhancement of T_2. Similar cancellations occur for (T_3, T_4, T_5), (T_6, T_7, T_8), (T_9, T_{10}), (T_{12}, T_{13}) and (T_{14}, T_{15}). Furthermore, we also observe that T_2 is 25 times larger than T_1' at 14 TeV, and 600 times larger than T_1' at 100 TeV.

From Eq. 5.26 and Eq. 5.27, we know that the amplitudes of the process $pp \to hhhjj$ are proportional to s^3. So the enhancement of the ratio of leading coefficients $T_0 - T_2$ at a 100 TeV and the LHC 14TeV is around 3000, which is one order magnitude larger than that of $D_0 - D_2$ in the process $pp \to hhjj$, as demonstrated in Tables 5.7 and 5.8, respectively. The coefficients $T_3 - T_5$ represent the subdominant contribution, which is one order of magnitude smaller than $T_0 - T_2$.

These results demonstrate the exceptional behavior of the SM as a gauge theory. All positive powers of s in the amplitude cancel and disappear in the SM limit. For phenomenological estimates at ultra-high energies, it is important to split off the SM part in such amplitudes and cross sections, even if the deviation from the SM is not small.

As a final result for this model, Fig. 5.10 shows the contours of constant cross section for $pp \to hhjj$ at the LHC and a 100 TeV collider in the $g_{a_1} - g_{a_2}$ plane, respectively. Similarly, in Fig. 5.11

$\sqrt{s}$	D_0	D_1	D_2	D_3	D_4	D_5
14 TeV	24.05	-34.29	13.01	-6.56	4.14	0.75
27 TeV	112.02	-171.54	69.58	-23.84	15.57	2.56
100 TeV	1854.13	- 3237.30	1466.21	-192.03	132.68	18.10

Table 5.7: Coefficients $D_0 - D_5$ (in fb) in the expression (5.47) for the process $pp \to hhjj$ at three different collider energies.

	T_0	T_1	T_2	T_3	T_4	T_5
14 TeV	3.81	-7.47	3.66	-0.84	1.41	-0.58
27 TeV	5.17×10^1	$- 1.02 \times 10^2$	5.08×10^1	-5.99	1.04×10^1	-4.48
100 TeV	1.00×10^4	$- 2.00 \times 10^4$	1.00×10^4	-2.02×10^2	3.70×10^2	-1.69×10^2

	T_6	T_7	T_8	T_9	T_{10}	T_{11}
14 TeV	0.11	-0.14	3.83×10^{-2}	-9.19×10^{-3}	5.81×10^{-3}	3.53×10^{-4}
27 TeV	5.89×10^{-1}	-7.66×10^{-1}	2.28×10^{-1}	-3.97×10^{-2}	2.59×10^{-2}	1.40×10^{-3}
100 TeV	7.66	- 10.12	2.99	-0.40	2.74×10^{-1}	1.24×10^{-2}

	T_{12}	T_{13}	T_{14}	T_{15}	T_{16}	T_{17}
14 TeV	4.43×10^{-2}	$- 4.25 \times 10^{-2}$	-9.03×10^{-3}	6.01×10^{-3}	5.38×10^{-4}	2.60×10^{-4}
27 TeV	2.88×10^{-1}	-2.80×10^{-1}	-4.40×10^{-2}	3.03×10^{-2}	2.28×10^{-3}	1.24×10^{-3}
100 TeV	7.68	- 7.58	-0.53	0.38	2.20×10^{-2}	1.47×10^{-2}

Table 5.8: Coefficients $T_0 - T_{17}$ (in fb) in the expression (5.48) for the process $pp \to hhhjj$ at three different collider energies.

we show the exclusion regions in the $g_{a_1} - g_{a_2}$ and $g_{a_1} - \lambda_3$ planes that can be derived from a cross section measurement for $pp \to hhhjj$. We note that there are two points in parameter space whose cross sections are as small as the SM prediction: the first point corresponds to $g_{a_1} \sim 0$; the second point corresponds to the case $g_{a_1}^2 - g_{a_2} \sim 0$. The first point is inconsistent with the observation of single-Higgs boson production in VBF, so only the second one is allowed.

For the specific case of the Higgs-inflation model, we compare the ratio of cross sections of $pp \to hhjj$ and $pp \to hhhjj$ to their SM prediction at the LHC and a 100 TeV collider. The result may be expressed in terms of $\hat{x} = 6\xi^2 v^2/M_p^2$, which is shown in Fig. 5.12.

5.3   Discussion for the backgrounds

An precise determination of the parameters of Eq. 3.2 involves a detail signal-background analysis. In this section we briefly review the phenomenology of the dominant final states that need to be analyzed in an experiment.

	T'_0	T'_1	T'_3	T'_4
14 TeV	4.96×10^{-3}	-1.45×10^{-1}	-1.34×10^{-2}	2.43×10^{-1}
100 TeV	2.25×10^{-1}	-1.64×10^{1}	-5.88×10^{-1}	3.14×10^{1}
Ratio	45.36	113.10	43.88	129.22
	T'_6	T'_7	T'_9	T'_{14}
14 TeV	1.12×10^{-2}	-6.34×10^{-2}	-3.38×10^{-3}	-3.02×10^{-3}
100 TeV	5.24×10^{-1}	-4.14	-1.28×10^{-1}	1.51×10^{-1}
Ratio	46.79	65.30	37.87	50.00

Table 5.9: Redefined coefficients $T'_0 - T'_{17}$ (in fb) in the expression (5.49) for the process $pp \rightarrow hhhjj$ at two different collider energies.

The decay channels of a triple-Higgs state have been considered in Ref. [71]. In particular, the decay channels $hhh \rightarrow b\bar{b}b\bar{b}\gamma\gamma$ and $hhh \rightarrow b\bar{b}WW^*WW^*$ have been studied for the ggF process [70, 71, 9]. For concreteness, we focus on three final states: $6b$, $4b2\tau$, and $4b2W$. We discuss their signal and background, referring to SM values of branching ratios and cross sections at 100 TeV collider.

The $6b$ final state, $hhh \rightarrow b\bar{b}b\bar{b}b\bar{b}$, has a branching ratio 20.30%. One of the main background for this final state is $pp \rightarrow ht\bar{t}$, which can decay to $4b$+jets. After applying the VBF cuts, we find that the $\sigma \times BR$ of this background is 3.48×10^4 ab at 100 TeV collider. It is challenging to further reduce this background by standard b-tagging techniques. The $pp \rightarrow ht\bar{t}jj$ background may become dominant after applying the VBF cuts. In this case, we consider the invisible decay of Higgs and the top quarks decay to $b\bar{b}$+jets. Current data show that the branching ratio of the invisible Higgs decay is smaller than 24% [11]. We calculate the cross section of this process by Madgraph5. After the VBF cuts, the maximized $\sigma \times BR$ of this background is 1.06×10^6 ab. Assuming the b-tagging effecience is 70% and the mistagging rate is 10%, this background can be further reduced by two orders of magnitude. Because of the invisible decay of Higgs, a large missing energy should be observed. Applying a missing energy cut can further reduce this background. In a realistic collider experiment, parton shower effects and pileup may lead to hard jets radiation from the signal. In this case, we have to consider the $h \rightarrow b\bar{b}$ decay of the $pp \rightarrow ht\bar{t}jj$ background. This is a complicate problem because it depends on the power of the future detector and a full detector simulation is necessasry, which is beyond the scope of current work.

Similarly, for the $4b2\tau$ final state, the process $pp \rightarrow ht\bar{t}$ is also the main background, whose branching ratio is 7.16%. This can be suppressed by using $3b$-tagging and τ-tagging techniques.

The channel $hhh \rightarrow b\bar{b}b\bar{b}WW^*$ has the largest branching ratio [71]. The preferred decay channels of the WW^* system are the semi-leptonic and fully-leptonic decays, whose branching ratios are 3.21% and 1.01%, respectively. Assuming that at a 100 TeV collider with an integrated luminosity of 30 ab^{-1}, we obtain 44 and 14 signal events, respectively. The dominant backgrounds of this channel include $pp \rightarrow ht\bar{t}$+jets, $pp \rightarrow Zt\bar{t}$+jets, $pp \rightarrow b\bar{b}t\bar{t}$+jets, etc. VBF cuts reduce these backgrounds by two orders of magnitude, but they are still six orders of magnitude larger than the signal.
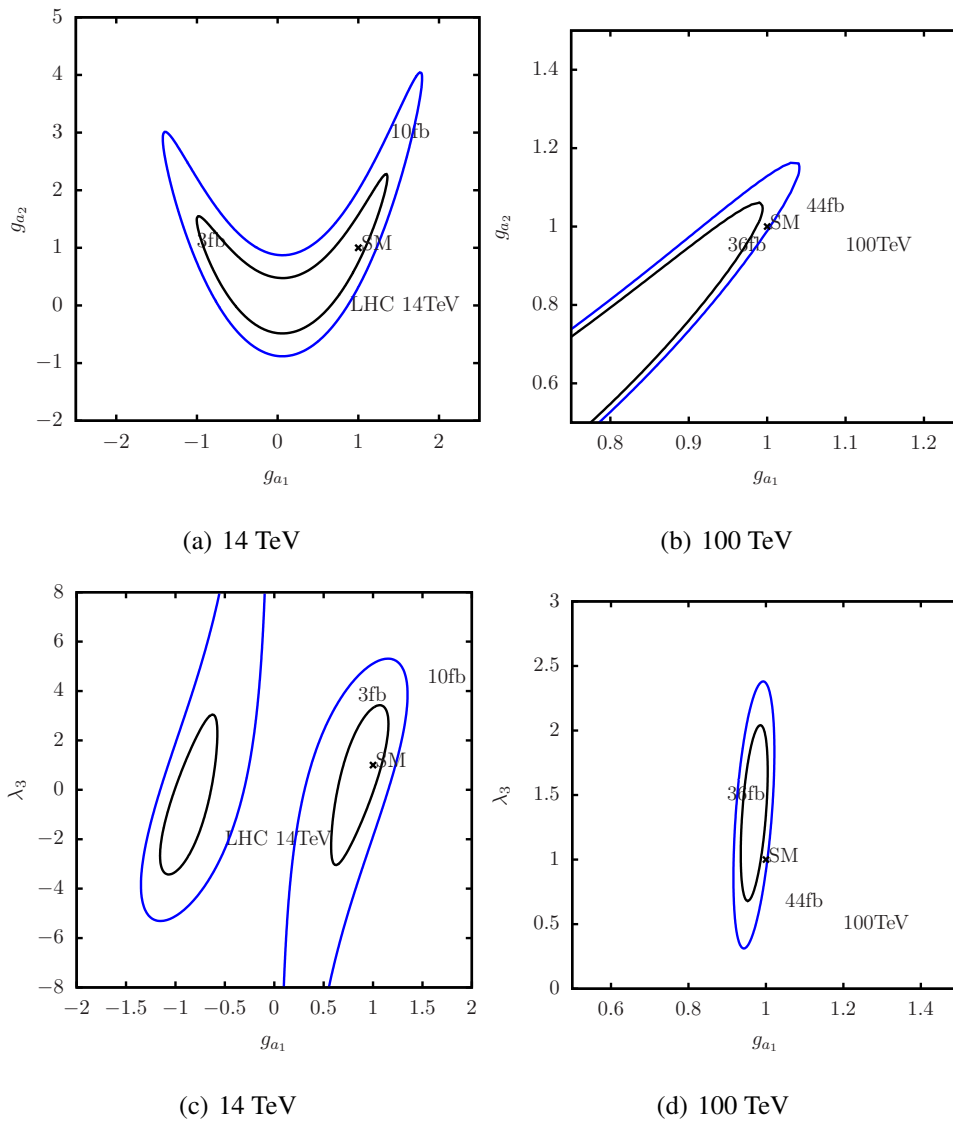
Figure 5.10: Projections for correlated bounds in the planes g_{a_1}-g_{a_2} and g_{a_1}-λ_3, from the process $pp \to hhjj$ with a strongly interacting Higgs sector at two different collider energies.

We conclude that an unambiguous discovery of a SM triple-Higgs signal in the VBF mode remains a real challenge. In the presence of new physics, particularly if the Higgs sector is strongly interacting, cross sections can be enhanced by two orders of magnitude, so in that case the situation is more promising.
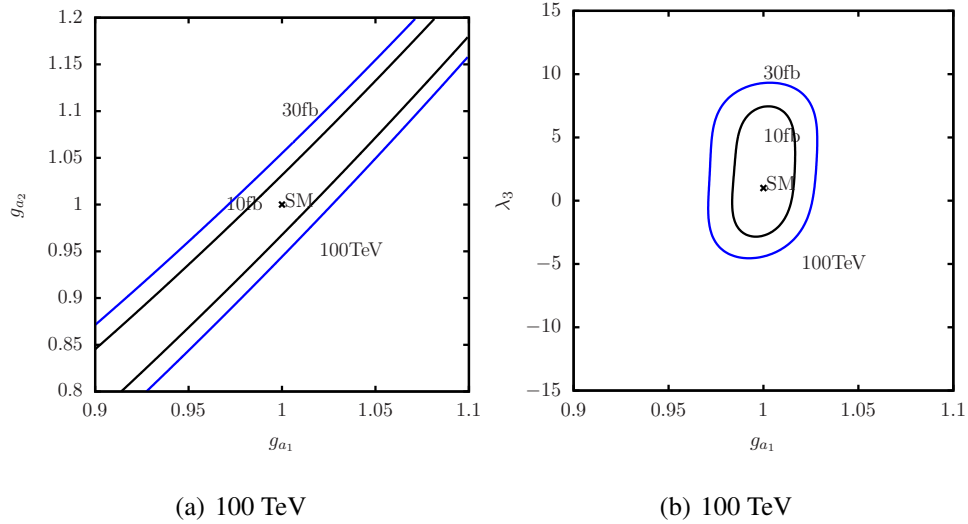
(a) 100 TeV   (b) 100 TeV

Figure 5.11: Projections for correlated bounds in the planes g_{a_1}-g_{a_2} and g_{a_1}-λ_3, from the process $pp \rightarrow hhhjj$ at a 100 TeV collider.

(a) $pp \rightarrow hhjj$ (b) $pp \rightarrow hhhjj$
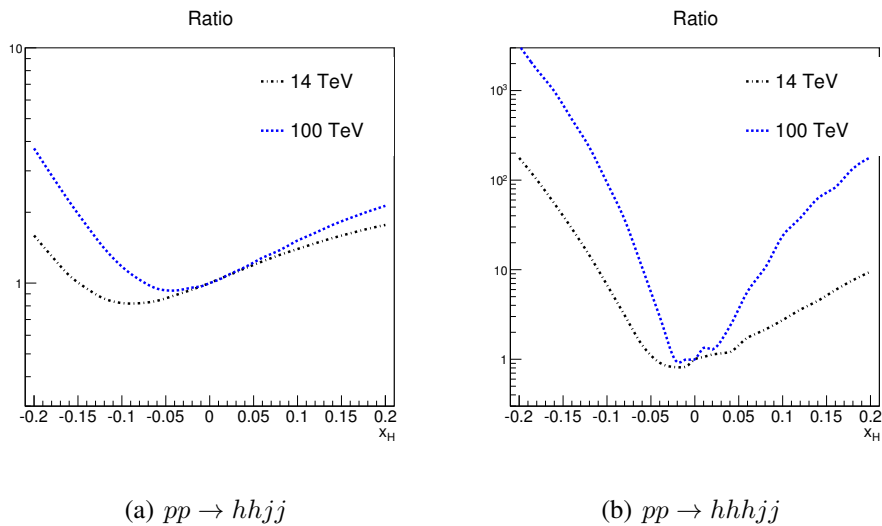
Figure 5.12: Cross section normalized to the SM cross section for the processes $pp \rightarrow hhjj$ and $pp \rightarrow hhhjj$, as a function of the parameter $\hat{x}$ in a Higgs-inflation model.

Chapter 6

Conclusion and Discussion

The SM is proven to be a successful theory to describe elementary particles and their interactions. However, some experimental measurements also suggest that the SM is not the final answer of our universe, and new physics beyond SM should exist. After the discovery of Higgs boson, measurements on its property and couplings to SM particles become essential to search for new physics. A complete knowledge of the Higgs potential and electroweak symmetry breaking cannot be obtained without the information of Higgs triple and quartic self-couplings. Measurements of these couplings involve multi-Higgs production processes, whose production rates are small at LHC. The cross sections of multi-Higgs production processes are enhanced significantly at 100 TeV hadron collider, so it is interesting to study multi-Higgs production at such machine.

New physics effects may contribute to multi-Higgs production processes and enhance the cross sections. To study the new physics effects, we introduced an effective Lagrangian, Eq. 3.2. Measurements of multi-Higgs production processes can determine these parameters. The generic Lagrangian defined by Eq. 3.2 can be related to other models. Strongly-Interacting Light Higgs model and Higgs inflation model are two examples.

At a hadron collider, gluon-gluon fusion is the dominant process of multi-Higgs production. We have explored the discovery potential for $gg \rightarrow hhh$ via the $2b2l^{\pm}4j + \not{E}$ decay channel at a 100 TeV hadron collider. Parton-level results show that the $mT2$ variable is useful to find the correct combinations of the visible objects that originate from Higgs boson decay, and to suppress background efficiently. However, once parton shower and detector effects are properly accounted for, extracting the SM signal becomes a real challenge. Two main problems are that (1) the transverse momentum of the softest jet from Higgs boson decay is around 10 GeV, which makes it difficult to reconstruct; (2) since there are six jets in the final state, the lepton isolation condition rejects most of the signal events.

Our effective field theory analysis shows that a sizable coefficient for a derivative operator can modify the kinematical distributions of the visible objects in the final states. In this case, a reconstruction of the triple-Higgs signal becomes feasible. We also investigate the potential of such a measurement to improve on constraints which is already obtained from single and double-Higgs production data. It turns out that while those processes are generally more powerful in constraining parameters

76

of Eq. 3.2, the triple-Higgs signal can be a supplementary and reduces the allowed parameter space.

The subdominant process of multi-Higgs production in hadron collisions is vector-boson-fusion. Even at a 100 TeV hadron collider, observing the multi-Higgs final state via this mode is very difficult if the SM is valid. Measurement for this process can nevertheless improve our knowledge about the interactions of the Higgs field. Our numerical results show that anomalous couplings can spoil the delicate gauge cancellations of the SM, and therefore can lead to an increase in rates of several orders of magnitude. Turning this around, putting bounds on vector-boson-fusion process does yield meaningful constraints on parameter space.

We also derive the generic formalism of unitarity to vector-boson-fusion process. Applying the generic formalism, we can figure out the energy-dependent region of parameter space where the model can still be considered as valid. We find that couplings of multiple Higgs fields to transverse polarized vector bosons can be constrained within that region, while constraints on couplings to longitudinally polarized vector fields become only marginally useful. In that case, for a detailed and quantitative assessment of the experimental resolution power, the straightforward effective theory approach should be replaced by parameterized unitary models as a physically more reliable source of simulated data.

For an alternative interpretation of the same measurements, we have investigated two more specific models. The first one is the Strongly-Interacting Light Higgs effective Lagrangian. The operator series expansion is truncated at dimension six but the higher-dimensional coefficients are not restricted to small values. The second one is the Higgs inflation models, which is considered as a connection between Higgs physics and cosmology. For both models, we perform the numerical computation of multi-Higgs production process, and show appropriate projections for the achievable bounds in parameter space at future hadron colliders, namely at the proposed 27 TeV HE-LHC and at a future 100 TeV collider.

Appendix A

Numerical cross sections of $gg \to h$, $gg \to hh$, and $gg \to hhh$

The cross section of $gg \to h$ can be parameterized as

$$\sigma(gg \to h) = K^h \times \left(\sum_{i=1}^{3} F_i^h C^{i,h}\right),$$ (A.1)

where the integrated form factors F_i^h and the coefficients $C^{i,h}$ are given in Table A.1, and K^h denotes the K-factor. The unit of F_i^h is pb.

It is found that values of F_i^h given in Table (A.1) do produce a positive definite cross section of $gg \to h$.

The cross section of $gg \to hh$ at 14 TeV LHC and a 100 TeV collider can be parameterized as

$$\sigma(gg \to hh) = K^{2h} \times \left(\sum_{i=1}^{27} F_i^{2h} C^{i,2h}\right),$$ (A.2)

where the integrated form factors F_i^{2h} and the coefficients $C^{i,2h}$ are given in Table A.2 and Table A.3. K^{2h} denotes the K-factor, which is equal to 2.20 for the LHC 14 TeV and 2.17 for the 100 TeV collision, respectively. The unit of F_i^{2h} in these two tables is fb.

	K^h	$C^{1,h} = a_1^2$	$C^{2,h} = a_1 c_1$	$C^{3,h} = c_1^2$
14 TeV	2.85	$F_1^h = 19.15$	$F_2^h = 36.05$	$F_3^h = 17.14$
100 TeV	2.24	$F_1^h = 357.53$	$F_2^h = 687.04$	$F_3^h = 332.79$

Table A.1: The numerical value of $F_1^h - F_3^h$ at hadron colliders in Eq. (A.1).

	C^{2h}		C^{2h}		C^{2h}
$F_1^{2h} = 36.17$	$a_1{}^4$	$F_2^{2h} = -74.13$	$a_1{}^2 a_2$	$F_3^{2h} = 44.58$	$a_2{}^2$
$F_4^{2h} = -32.32$	$a_1{}^2 c_2$	$F_5^{2h} = 43.31$	$a_2 c_2$	$F_6^{2h} = 23.34$	$c_2{}^2$
$F_7^{2h} = -48.98$	$a_1{}^3 \kappa_5$	$F_8^{2h} = 56.9$	$a_1 a_2 \kappa_5$	$F_9^{2h} = -22.96$	$a_1{}^2 c_1 \kappa_5$
$F_{10}^{2h} = 29.01$	$a_2 c_1 \kappa_5$	$F_{11}^{2h} = 28.9$	$a_1 c_2 \kappa_5$	$F_{12}^{2h} = 29.06$	$c_1 c_2 \kappa_5$
$F_{13}^{2h} = 18.54$	$a_1{}^2 \kappa_5{}^2$	$F_{14}^{2h} = 19.78$	$a_1 c_1 \kappa_5{}^2$	$F_{15}^{2h} = 9.32$	$c_1{}^2 \kappa_5{}^2$
$F_{16}^{2h} = -23.87$	$a_1{}^3 \lambda_3$	$F_{17}^{2h} = 24.71$	$a_1 a_2 \lambda_3$	$F_{18}^{2h} = -13.7$	$a_1{}^2 c_1 \lambda_3$
$F_{19}^{2h} = 14.78$	$a_2 c_1 \lambda_3$	$F_{20}^{2h} = 14.53$	$a_1 c_2 \lambda_3$	$F_{21}^{2h} = 11.36$	$c_1 c_2 \lambda_3$
$F_{22}^{2h} = 17.28$	$a_1{}^2 \kappa_5 \lambda_3$	$F_{23}^{2h} = 21.3$	$a_1 c_1 \kappa_5 \lambda_3$	$F_{24}^{2h} = 8.19$	$c_1{}^2 \kappa_5 \lambda_3$
$F_{25}^{2h} = 4.94$	$a_1{}^2 \lambda_3{}^2$	$F_{26}^{2h} = 6.68$	$a_1 c_1 \lambda_3{}^2$	$F_{27}^{2h} = 2.53$	$c_1{}^2 \lambda_3{}^2$

Table A.2: The numerical value of $F_1^{2h} - F_{27}^{2h}$ at the LHC 14 TeV in Eq. (A.2).

	C^{2h}		C^{2h}		C^{2h}
$F_1^{2h} = 1565.1$	$a_1{}^4$	$F_2^{2h} = -3346.56$	$a_1{}^2 a_2$	$F_3^{2h} = 2274.94$	$a_2{}^2$
$F_4^{2h} = -1232.43$	$a_1{}^2 c_2$	$F_5^{2h} = 1790.73$	$a_2 c_2$	$F_6^{2h} = 2407.17$	$c_2{}^2$
$F_7^{2h} = -2133.02$	$a_1{}^3 \kappa_5$	$F_8^{2h} = 2781.8$	$a_1 a_2 \kappa_5$	$F_9^{2h} = -857.36$	$a_1{}^2 c_1 \kappa_5$
$F_{10}^{2h} = 1174.17$	$a_2 c_1 \kappa_5$	$F_{11}^{2h} = 1202.36$	$a_1 c_2 \kappa_5$	$F_{12}^{2h} = 2651.46$	$c_1 c_2 \kappa_5$
$F_{13}^{2h} = 866.44$	$a_1{}^2 \kappa_5{}^2$	$F_{14}^{2h} = 797.2$	$a_1 c_1 \kappa_5{}^2$	$F_{15}^{2h} = 745.46$	$c_1{}^2 \kappa_5{}^2$
$F_{16}^{2h} = -924.06$	$a_1{}^3 \lambda_3$	$F_{17}^{2h} = 1014.84$	$a_1 a_2 \lambda_3$	$F_{18}^{2h} = -494.$	$a_1{}^2 c_1 \lambda_3$
$F_{19}^{2h} = 567.$	$a_2 c_1 \lambda_3$	$F_{20}^{2h} = 604.62$	$a_1 c_2 \lambda_3$	$F_{21}^{2h} = 510.85$	$c_1 c_2 \lambda_3$
$F_{22}^{2h} = 679.86$	$a_1{}^2 \kappa_5 \lambda_3$	$F_{23}^{2h} = 817.06$	$a_1 c_1 \kappa_5 \lambda_3$	$F_{24}^{2h} = 342.33$	$c_1{}^2 \kappa_5 \lambda_3$
$F_{25}^{2h} = 172.4$	$a_1{}^2 \lambda_3{}^2$	$F_{26}^{2h} = 232.94$	$a_1 c_1 \lambda_3{}^2$	$F_{27}^{2h} = 88.15$	$c_1{}^2 \lambda_3{}^2$

Table A.3: The numerical value of $F_1^{2h} - F_{27}^{2h}$ at a 100 TeV collider in Eq. (A.2).

The largest absolute value goes to the coefficient F_2^{2h}, which is 74.13 and 3346.56 for either 14 TeV or 100 TeV cases. The minimal absolute value goes to the coefficient F_{27}^{2h}, which is 2.53 for 14 TeV and 88.15 for 100 TeV case.

Compared with those of the 14 TeV case, most of coefficients can be enhanced by a factor around 40 or so for the 100 TeV case. Among them, the coefficients F_6^{2h}, F_{12}^{2h} and F_{15}^{2h} have the largest enhancements from 14 TeV to 100 TeV collisions, and they are 103.1, 91.2, and 79.9, respectively.

In order to guarantee the positive and definite results of the cross section of all points in the parameter space, the contribution of b quark should be removed from the diagrams. Otherwise, a more general parameterisation of the cross section should be introduced. Furthermore, we have used more than 5,000 points in the parameter space of a_2, c_2, κ_5, and λ_3 to determine these F_i^{2h} after taking into account the constraints on parameters a_1 and c_1 from the projected precision in the measurement of $\sigma(gg \to h)$. The positivity and definiteness of the cross sections are examined to be hold in a random scan in the parameter space of a_2, c_2, κ_5, and λ_3 with a total number of points 10^7. If a_1 and c_1 can significantly deviate from the values of the SM, these results might not be valid anymore.

The cross section of $gg \to hhh$ at a 100 TeV collider can be parameterized as

$$\sigma(gg \to hhh) = K^{3h} \times \left(\sum_{i=1}^{154} F_i^{3h} C^{i,3h} \right), \tag{A.3}$$

where the integrated form factors F_i^{3h} and the coefficients $C^{i,3h}$ are given in Table A.4 and Table A.5. K denotes the K-factor which is taken as 2.1. The unit of F_i^{3h} is fb. We have used more than 12,000 points to determine these F_i^{3h}.

The largest absolute coefficient is F_{30}^{3h}. In contrast, the smallest absolute coefficients are F_{81}^{3h} and F_{83}^{3h}.

After taking into account the constraints on parameters a_1 and c_1 from the projected precision data of $\sigma(gg \to h)$ and the constraints on parameters a_2, c_2, λ_3 and κ_5 from the projected precision data of $\sigma(gg \to hh)$, the positivity and definiteness of the cross sections are examined to be hold in a random scan in the parameter space of a_3, λ_4 and κ_6 with a total number of points 10^7.

	C^{3h}		C^{3h}		C^{3h}
$F_1^{3h} = 7.47$	$a_1{}^6$	$F_2^{3h} = -19.58$	$a_1{}^4 a_2$	$F_3^{3h} = 31.31$	$a_1{}^2 a_2{}^2$
$F_4^{3h} = -1.57$	$a_1{}^3 a_3$	$F_5^{3h} = -18.57$	$a_1 a_2 a_3$	$F_6^{3h} = 11.62$	$a_3{}^2$
$F_7^{3h} = -13.69$	$a_1{}^5 \kappa_5$	$F_8^{3h} = 38.21$	$a_1{}^3 a_2 \kappa_5$	$F_9^{3h} = -35.02$	$a_1 a_2{}^2 \kappa_5$
$F_{10}^{3h} = -11.93$	$a_1{}^2 a_3 \kappa_5$	$F_{11}^{3h} = 40.49$	$a_2 a_3 \kappa_5$	$F_{12}^{3h} = -12.54$	$a_1{}^3 c_2 \kappa_5$
$F_{13}^{3h} = 68.7$	$a_1 a_2 c_2 \kappa_5$	$F_{14}^{3h} = -43.97$	$a_3 c_2 \kappa_5$	$F_{15}^{3h} = 12.32$	$a_1{}^4 \kappa_5{}^2$
$F_{16}^{3h} = -48.4$	$a_1{}^2 a_2 \kappa_5{}^2$	$F_{17}^{3h} = 35.74$	$a_2{}^2 \kappa_5{}^2$	$F_{18}^{3h} = 28.13$	$a_1 a_3 \kappa_5{}^2$
$F_{19}^{3h} = -9.72$	$a_1{}^3 c_1 \kappa_5{}^2$	$F_{20}^{3h} = 46.85$	$a_1 a_2 c_1 \kappa_5{}^2$	$F_{21}^{3h} = -28.8$	$a_3 c_1 \kappa_5{}^2$
$F_{22}^{3h} = 44.85$	$a_1{}^2 c_2 \kappa_5{}^2$	$F_{23}^{3h} = -61.34$	$a_2 c_2 \kappa_5{}^2$	$F_{24}^{3h} = 935.73$	$c_2{}^2 \kappa_5{}^2$
$F_{25}^{3h} = -16.66$	$a_1{}^3 \kappa_5{}^3$	$F_{26}^{3h} = 49.63$	$a_1 a_2 \kappa_5{}^3$	$F_{27}^{3h} = 30.55$	$a_1{}^2 c_1 \kappa_5{}^3$
$F_{28}^{3h} = -40.08$	$a_2 c_1 \kappa_5{}^3$	$F_{29}^{3h} = -33.7$	$a_1 c_2 \kappa_5{}^3$	$F_{30}^{3h} = 1244.83$	$c_1 c_2 \kappa_5{}^3$
$F_{31}^{3h} = 17.29$	$a_1{}^2 \kappa_5{}^4$	$F_{32}^{3h} = -21.77$	$a_1 c_1 \kappa_5{}^4$	$F_{33}^{3h} = 414.36$	$c_1{}^2 \kappa_5{}^4$
$F_{34}^{3h} = -0.57$	$a_1{}^4 \kappa_6$	$F_{35}^{3h} = -10.98$	$a_1{}^2 a_2 \kappa_6$	$F_{36}^{3h} = 12.06$	$a_1 a_3 \kappa_6$
$F_{37}^{3h} = -2.73$	$a_1{}^3 c_1 \kappa_6$	$F_{38}^{3h} = 20.91$	$a_1 a_2 c_1 \kappa_6$	$F_{39}^{3h} = -14.48$	$a_3 c_1 \kappa_6$
$F_{40}^{3h} = -6.95$	$a_1{}^3 \kappa_5 \kappa_6$	$F_{41}^{3h} = 21.22$	$a_1 a_2 \kappa_5 \kappa_6$	$F_{42}^{3h} = 13.81$	$a_1{}^2 c_1 \kappa_5 \kappa_6$
$F_{43}^{3h} = -20.28$	$a_2 c_1 \kappa_5 \kappa_6$	$F_{44}^{3h} = -22.57$	$a_1 c_2 \kappa_5 \kappa_6$	$F_{45}^{3h} = 609.84$	$c_1 c_2 \kappa_5 \kappa_6$
$F_{46}^{3h} = 14.81$	$a_1{}^2 \kappa_5{}^2 \kappa_6$	$F_{47}^{3h} = -25.91$	$a_1 c_1 \kappa_5{}^2 \kappa_6$	$F_{48}^{3h} = 406.05$	$c_1{}^2 \kappa_5{}^2 \kappa_6$
$F_{49}^{3h} = 3.17$	$a_1{}^2 \kappa_6{}^2$	$F_{50}^{3h} = -7.38$	$a_1 c_1 \kappa_6{}^2$	$F_{51}^{3h} = 99.6$	$c_1{}^2 \kappa_6{}^2$
$F_{52}^{3h} = -7.66$	$a_1{}^5 \lambda_3$	$F_{53}^{3h} = 19.44$	$a_1{}^3 a_2 \lambda_3$	$F_{54}^{3h} = -15.69$	$a_1 a_2{}^2 \lambda_3$
$F_{55}^{3h} = -5.8$	$a_1{}^2 a_3 \lambda_3$	$F_{56}^{3h} = 11.98$	$a_2 a_3 \lambda_3$	$F_{57}^{3h} = -6.43$	$a_1{}^3 c_2 \lambda_3$
$F_{58}^{3h} = 13.84$	$a_1 a_2 c_2 \lambda_3$	$F_{59}^{3h} = -0.21$	$a_3 c_2 \lambda_3$	$F_{60}^{3h} = 14.43$	$a_1{}^4 \kappa_5 \lambda_3$
$F_{61}^{3h} = -37.05$	$a_1{}^2 a_2 \kappa_5 \lambda_3$	$F_{62}^{3h} = 22.98$	$a_2{}^2 \kappa_5 \lambda_3$	$F_{63}^{3h} = 9.86$	$a_1 a_3 \kappa_5 \lambda_3$
$F_{64}^{3h} = -5.78$	$a_1{}^3 c_1 \kappa_5 \lambda_3$	$F_{65}^{3h} = 10.78$	$a_1 a_2 c_1 \kappa_5 \lambda_3$	$F_{66}^{3h} = 0.4$	$a_3 c_1 \kappa_5 \lambda_3$
$F_{67}^{3h} = 9.62$	$a_1{}^2 c_2 \kappa_5 \lambda_3$	$F_{68}^{3h} = 2.49$	$a_2 c_2 \kappa_5 \lambda_3$	$F_{69}^{3h} = 73.58$	$c_2{}^2 \kappa_5 \lambda_3$
$F_{70}^{3h} = -18.8$	$a_1{}^3 \kappa_5{}^2 \lambda_3$	$F_{71}^{3h} = 35.59$	$a_1 a_2 \kappa_5{}^2 \lambda_3$	$F_{72}^{3h} = 7.37$	$a_1{}^2 c_1 \kappa_5{}^2 \lambda_3$
$F_{73}^{3h} = 3.23$	$a_2 c_1 \kappa_5{}^2 \lambda_3$	$F_{74}^{3h} = 4.32$	$a_1 c_2 \kappa_5{}^2 \lambda_3$	$F_{75}^{3h} = 97.65$	$c_1 c_2 \kappa_5{}^2 \lambda_3$

Table A.4: The numerical value of $F_1 - F_{75}$ at 100TeV hadron collider in Eq. (A.3).

	C^{3h}		C^{3h}		C^{3h}
$F_{76}^{3h} = 13.75$	$a_1{}^2\kappa_5{}^3\lambda_3$	$F_{77}^{3h} = 4.16$	$a_1 c_1 \kappa_5{}^3 \lambda_3$	$F_{78}^{3h} = 32.71$	$c_1{}^2 \kappa_5{}^3 \lambda_3$
$F_{79}^{3h} = -3.37$	$a_1{}^3 \kappa_6 \lambda_3$	$F_{80}^{3h} = 6.86$	$a_1 a_2 \kappa_6 \lambda_3$	$F_{81}^{3h} = 0.01$	$a_1{}^2 c_1 \kappa_6 \lambda_3$
$F_{82}^{3h} = 0.57$	$a_2 c_1 \kappa_6 \lambda_3$	$F_{83}^{3h} = -0.01$	$a_1 c_2 \kappa_6 \lambda_3$	$F_{84}^{3h} = 22.56$	$c_1 c_2 \kappa_6 \lambda_3$
$F_{85}^{3h} = 5.58$	$a_1{}^2 \kappa_5 \kappa_6 \lambda_3$	$F_{86}^{3h} = 1.29$	$a_1 c_1 \kappa_5 \kappa_6 \lambda_3$	$F_{87}^{3h} = 14.88$	$c_1{}^2 \kappa_5 \kappa_6 \lambda_3$
$F_{88}^{3h} = 4.32$	$a_1{}^4 \lambda_3{}^2$	$F_{89}^{3h} = -8.46$	$a_1{}^2 a_2 \lambda_3{}^2$	$F_{90}^{3h} = 5.24$	$a_2{}^2 \lambda_3{}^2$
$F_{91}^{3h} = 0.99$	$a_1 a_3 \lambda_3{}^2$	$F_{92}^{3h} = -0.53$	$a_1{}^3 c_1 \lambda_3{}^2$	$F_{93}^{3h} = 0.37$	$a_1 a_2 c_1 \lambda_3{}^2$
$F_{94}^{3h} = 0.29$	$a_3 c_1 \lambda_3{}^2$	$F_{95}^{3h} = 1.19$	$a_1{}^2 c_2 \lambda_3{}^2$	$F_{96}^{3h} = 2.32$	$a_2 c_2 \lambda_3{}^2$
$F_{97}^{3h} = 7.71$	$c_2{}^2 \lambda_3{}^2$	$F_{98}^{3h} = -7.67$	$a_1{}^3 \kappa_5 \lambda_3{}^2$	$F_{99}^{3h} = 11.39$	$a_1 a_2 \kappa_5 \lambda_3{}^2$
$F_{100}^{3h} = 0.94$	$a_1{}^2 c_1 \kappa_5 \lambda_3{}^2$	$F_{101}^{3h} = 3.02$	$a_2 c_1 \kappa_5 \lambda_3{}^2$	$F_{102}^{3h} = 3.06$	$a_1 c_2 \kappa_5 \lambda_3{}^2$
$F_{103}^{3h} = 12.29$	$c_1 c_2 \kappa_5 \lambda_3{}^2$	$F_{104}^{3h} = 5.69$	$a_1{}^2 \kappa_5{}^2 \lambda_3{}^2$	$F_{105}^{3h} = 3.39$	$a_1 c_1 \kappa_5{}^2 \lambda_3{}^2$
$F_{106}^{3h} = 5.$	$c_1{}^2 \kappa_5{}^2 \lambda_3{}^2$	$F_{107}^{3h} = 0.58$	$a_1{}^2 \kappa_6 \lambda_3{}^2$	$F_{108}^{3h} = 0.41$	$a_1 c_1 \kappa_6 \lambda_3{}^2$
$F_{109}^{3h} = 0.36$	$c_1{}^2 \kappa_6 \lambda_3{}^2$	$F_{110}^{3h} = -0.96$	$a_1{}^3 \lambda_3{}^3$	$F_{111}^{3h} = 1.18$	$a_1 a_2 \lambda_3{}^3$
$F_{112}^{3h} = -0.06$	$a_1{}^2 c_1 \lambda_3{}^3$	$F_{113}^{3h} = 0.44$	$a_2 c_1 \lambda_3{}^3$	$F_{114}^{3h} = 0.41$	$a_1 c_2 \lambda_3{}^3$
$F_{115}^{3h} = 0.69$	$c_1 c_2 \lambda_3{}^3$	$F_{116}^{3h} = 1.14$	$a_1{}^2 \kappa_5 \lambda_3{}^3$	$F_{117}^{3h} = 0.85$	$a_1 c_1 \kappa_5 \lambda_3{}^3$
$F_{118}^{3h} = 0.6$	$c_1{}^2 \kappa_5 \lambda_3{}^3$	$F_{119}^{3h} = 0.09$	$a_1{}^2 \lambda_3{}^4$	$F_{120}^{3h} = 0.07$	$a_1 c_1 \lambda_3{}^4$
$F_{121}^{3h} = 0.04$	$c_1{}^2 \lambda_3{}^4$	$F_{122}^{3h} = 0.16$	$a_1{}^4 \lambda_4$	$F_{123}^{3h} = -1.54$	$a_1{}^2 a_2 \lambda_4$
$F_{124}^{3h} = 0.96$	$a_1 a_3 \lambda_4$	$F_{125}^{3h} = -0.59$	$a_1{}^3 c_1 \lambda_4$	$F_{126}^{3h} = 0.9$	$a_1 a_2 c_1 \lambda_4$
$F_{127}^{3h} = 0.11$	$a_3 c_1 \lambda_4$	$F_{128}^{3h} = -1.08$	$a_1{}^3 \kappa_5 \lambda_4$	$F_{129}^{3h} = 1.86$	$a_1 a_2 \kappa_5 \lambda_4$
$F_{130}^{3h} = 0.56$	$a_1{}^2 c_1 \kappa_5 \lambda_4$	$F_{131}^{3h} = 0.28$	$a_2 c_1 \kappa_5 \lambda_4$	$F_{132}^{3h} = 0.24$	$a_1 c_2 \kappa_5 \lambda_4$
$F_{133}^{3h} = 3.71$	$c_1 c_2 \kappa_5 \lambda_4$	$F_{134}^{3h} = 1.35$	$a_1{}^2 \kappa_5{}^2 \lambda_4$	$F_{135}^{3h} = 0.47$	$a_1 c_1 \kappa_5{}^2 \lambda_4$
$F_{136}^{3h} = 2.54$	$c_1{}^2 \kappa_5{}^2 \lambda_4$	$F_{137}^{3h} = 0.54$	$a_1{}^2 \kappa_6 \lambda_4$	$F_{138}^{3h} = 0.17$	$a_1 c_1 \kappa_6 \lambda_4$
$F_{139}^{3h} = 1.15$	$c_1{}^2 \kappa_6 \lambda_4$	$F_{140}^{3h} = -0.65$	$a_1{}^3 \lambda_3 \lambda_4$	$F_{141}^{3h} = 0.91$	$a_1 a_2 \lambda_3 \lambda_4$
$F_{142}^{3h} = 0.08$	$a_1{}^2 c_1 \lambda_3 \lambda_4$	$F_{143}^{3h} = 0.28$	$a_2 c_1 \lambda_3 \lambda_4$	$F_{144}^{3h} = 0.22$	$a_1 c_2 \lambda_3 \lambda_4$
$F_{145}^{3h} = 0.85$	$c_1 c_2 \lambda_3 \lambda_4$	$F_{146}^{3h} = 0.83$	$a_1{}^2 \kappa_5 \lambda_3 \lambda_4$	$F_{147}^{3h} = 0.48$	$a_1 c_1 \kappa_5 \lambda_3 \lambda_4$
$F_{148}^{3h} = 0.68$	$c_1{}^2 \kappa_5 \lambda_3 \lambda_4$	$F_{149}^{3h} = 0.11$	$a_1{}^2 \lambda_3{}^2 \lambda_4$	$F_{150}^{3h} = 0.08$	$a_1 c_1 \lambda_3{}^2 \lambda_4$
$F_{151}^{3h} = 0.06$	$c_1{}^2 \lambda_3{}^2 \lambda_4$	$F_{152}^{3h} = 0.04$	$a_1{}^2 \lambda_4{}^2$	$F_{153}^{3h} = 0.03$	$a_1 c_1 \lambda_4{}^2$
$F_{154}^{3h} = 0.03$	$c_1{}^2 \lambda_4{}^2$				

Table A.5: The numerical value of $F_{76} - F_{154}$ at 100TeV hadron collider in Eq. (A.3).

Appendix B

Details for the derivation of unitarity constraints

In this appendix, we provide the explict derivation and its connection to the generic formulas in Chapter 5. The derivation is not only applied to $2 \to 2$ scattering, but also to $2 \to n$ scattering.

B.1 $2 \to 2$ scattering

In this section, we derive the unitarity for $2 \to 2$ scattering. It applys to any combination of two-particle initial and final states a and b, respectively. For a two-particle state vector $|\alpha, \Phi_a\rangle$, working in the center of mass frame, it is convenient to choose the polar angle θ_a and azimuthal angle ϕ_a as phase-space parameters. In this case, the normalized kinematics variables are $\vec{x}_a = (\frac{1}{2}(\cos\theta_a + 1), \frac{\phi_a}{2\pi})$. The Jacobian determinant is given by

$$J_a = \frac{1}{8\pi} \frac{1}{S_\alpha} s^{-1} \sqrt{[s - (m_{a1} + m_{a2})^2][s - (m_{a1} - m_{a2})^2]} \tag{B.1}$$

where m_{a1}, m_{a2} are the masses of particles in initial state a. S_α is the symmetry factor that accounts for identical particles in a with quantum-number combination α: if the two particles are identical then $S_\alpha = 2$, otherwise $S_\alpha = 1$.

Following Ref. [132], in the center of mass frame, the scattering matrix from the two-particle state $|\alpha, \Phi_a\rangle$ to $|\beta, \Phi_b\rangle$ can be written as[1]

$$
\begin{aligned}
M^{\beta\alpha}(x_b, x_a) &\equiv J_b^{\frac{1}{2}} \langle \beta, \theta_b, \phi_b | \mathcal{M} | \alpha, \theta_a, \phi_a \rangle J_a^{\frac{1}{2}} \\
&= 2 \sum_j (2j+1) a_j^{\alpha\beta} D^j_{\lambda_\alpha \lambda_\beta}(\zeta_1, \zeta_2, \zeta_3) \\
&= 2 \sum_{j,m} (2j+1) a_j^{\alpha\beta} D^{j*}_{m\lambda_\alpha}(\phi_a, \theta_a, 0) D^j_{m\lambda_\beta}(\phi_b, \theta_b, 0)
\end{aligned}
\tag{B.2}
$$

---

[1]To be consistent with the explicit choice of polarization vector in Eq. B.6, our phase convention differs from Ref. [132].

where θ_a (θ_b) are the polar angles and ϕ_a (ϕ_b) are the azimuthal angles for the states $|\alpha, \Phi_a\rangle$ ($|\beta, \Phi_b\rangle$), respectively. ζ_1, ζ_2, and ζ_3 denote corresponding Euler angles of the rotation from direction (θ_a, ϕ_a) to direction (θ_b, ϕ_b). The four-momenta of these particles can be parametrized in terms of polar and azimuthal angles

$$p^\mu = (E, |\vec{p}| \sin\theta \cos\phi, |\vec{p}| \sin\theta \sin\phi, |\vec{p}| \cos\theta) \tag{B.3}$$

When the particle is a massive vector boson, the polarization states are defined as follows:

$$|p, +\rangle = \frac{1}{\sqrt{2}}(0, \cos\phi\cos\theta + i\sin\phi, \sin\phi\cos\theta - i\cos\phi, -\sin\theta) \tag{B.4}$$

$$|p, -\rangle = \frac{1}{\sqrt{2}}(0, \cos\phi\cos\theta - i\sin\phi, \sin\phi\cos\theta + i\cos\phi, -\sin\theta) \tag{B.5}$$

$$|p, 0\rangle = (\frac{|\vec{p}|}{m}, \frac{p^0}{m}\sin\theta\cos\phi, \frac{p^0}{m}\sin\theta\sin\phi, \frac{p^0}{m}\cos\theta) \tag{B.6}$$

where $m = \sqrt{E^2 - |\vec{p}|^2}$.

This expansion suggests that we choose the Wigner D-matrix is an orthonormal basis for the 2-particle phase spaces,

$$H_{jm}^\alpha(\vec{x}) = \sqrt{2j+1} D_{m\lambda_\alpha}^{j*}(\phi_a, \theta_a, 0) \tag{B.7}$$

As a result, in the scattering amplitude between two-particle states the corresponding amplitude a becomes diagonal and depends only on one index:

$$a_{jm,j'm'}^{\alpha\beta} = \delta_{jj'}\delta_{mm'}a_j^{\alpha\beta} \tag{B.8}$$

where we introduce reduced a-coefficients $a_j^{\alpha\beta}$.

Similarly, the b-coefficients can be reduced to a one-index version:

$$b_{jm}^{\alpha\beta} = \sum_{j'm'} |a_{jm,j'm'}^{\alpha\beta}|^2 = |a_j^{\alpha\beta}|^2 \tag{B.9}$$

So the set of unitarity conditions is thus reduced to

$$|\mathrm{Re}\, a_j^{\alpha\alpha}| \leq \frac{1}{2} \tag{B.10}$$

$$|\mathrm{Im}\, a_j^{\alpha\alpha} - \frac{1}{2}| \leq \frac{1}{2} \tag{B.11}$$

$$\sum_{\beta \neq \alpha} b_j^{\alpha\beta} = \sum_{\beta \neq \alpha} |a_j^{\alpha\beta}|^2 \leq \frac{1}{4} \tag{B.12}$$

These conditions are equivalent to those in Refs. [121, 133, 134], if only $2 \to 2$ processes are considered.

B.2 $2 \to n$ **scattering: general idea**

The unitarity conditions (5.13) do not depend on the features of the intermediate state c, which can be any n-particle state. The conditions can be expressed in terms of b coefficients,

$$b_A^{\alpha\gamma} \equiv \frac{1}{4} \int \mathrm{d}x_a \mathrm{d}x_b \mathrm{d}x_c H_A^{\alpha*}(x_a) H_A^{\alpha}(x_b) M^{\gamma\alpha*}(x_c, x_b) M^{\gamma\alpha}(x_c, x_a) \leq \frac{1}{4} \qquad (B.13)$$

which by construction are independent of the phase-space parameterization pertaining to Φ_c. γ represent discrete quantum numbers of the intermediate state c.

In analogy to the $2 \to 2$ case, we may use any orthonormal basis for the initial two-particle state a. Choosing the same Wigner D-matrix expansion is most convenient. However, due to angular-momentum conservation, the b coefficients only depend on one index

$$b_{jm}^{\alpha\gamma} \equiv b_{jm'}^{\alpha\gamma} \equiv b_j^{\alpha\gamma}, \qquad (B.14)$$

but is independent of the complexity of the intermediate states c.

At this point, we may discuss the connection to literature on this subject [122, 123, 125].

- In Refs. [122, 123], unitarity constraints are formulated for the total cross section of $2 \to n$ scattering with a assumption that the $j = 0$ partial wave (s-wave) is dominant. This assumption applies to some subsets of the states that we consider here, but clearly is not justified for the generic case of polarized vector-boson scattering.

  In fact, with our notation, the cross section for $a \to c$ with discrete quantum numbers α, γ is given by:

$$\sigma_{\alpha\gamma}(a \to c) = \frac{16\pi S_\alpha s}{[s - (m_{a1} + m_{a2})^2][s - (m_{a1} - m_{a2})^2]} \sum_j (2j + 1) b_j^{\alpha\gamma} \qquad (B.15)$$

  where b_j are the reduced b-coefficients after choosing the Wigner D-matrix as basis.

  Assuming that the $j = 0$ partial wave dominates in the high-energy limit, we obtain

$$\sigma_{\alpha\gamma}(a \to c) \approx \frac{16\pi S_\alpha}{s} b_0^{\alpha\gamma} \leq \frac{4\pi S_\alpha}{s} \qquad (B.16)$$

  which is equivalent to the result of Ref. [122, 123]. This inequality applies to any polarized cross section and could provide a stronger bound than its equivalent for an unpolarized cross section.

- Ref. [125] considers a more generic case of $2 \to n$ scattering without s-wave dominance, but restricts the derivation to spin-less particles. In that case, the Wigner D-matrix formalism collapses to the familiar formalism of Legendre polynomials and spherical harmonics. By the

general relation

$$P_l(\cos\theta_{ba}) = \frac{4\pi}{2l+1} \sum_{m=-l}^{l} Y_l^m(\theta_b, \phi_b) Y_l^{m*}(\theta_a, \phi_a),$$ (B.17)

the relative polar angle θ_{ba} can be determined via

$$\cos\theta_{ba} = \cos\theta_b \cos\theta_a + \sin\theta_b \sin\theta_a \cos(\phi_b - \phi_a).$$ (B.18)

The Wigner D-matrix reduces to spherical harmonics as follows,

$$D_{m0}^j(\phi, \theta, 0) = \sqrt{\frac{4\pi}{2j+1}} Y_l^{m*}(\theta, \phi)$$ (B.19)

With these relations, it is easy to verify that our formulas are equivalent to those of Ref. [125] in the spin-less case.

B.3 Generalized s-wave

For some helicity combinations, the unitarity condition for $2 \to n$ scattering becomes independent of phase-space parameters in the high-energy limit. This situation was considered in Refs. [122, 123]. In this subsection, we introduce the details for our application.

In the high-energy limit, all external particles can be treated as massless, $p_i^2 = 0$. The generalized s-wave condition for scattering $a \to c$ have the form

$$\langle \gamma, \Phi_c | \mathcal{M} | \alpha, \Phi_a \rangle \approx \mathcal{C},$$ (B.20)

where $\mathcal{C}$ is a constant with respect to the kinematical parameters, for fixed total four-momentum. In fact, in the EFT approximation, this situation occurs naturally for some of the terms since the leading contributions become polynomials of the Lorentz invariants.

(a) For the case of inelastic scattering $\alpha \neq \gamma$, the b-coefficients with (multi-)index A take the form

$$\begin{aligned} b_A^{\alpha\gamma} &= \frac{1}{4} \int_0^1 \mathrm{d}\vec{x}_a \mathrm{d}\vec{x}_b \, H_A^{\alpha*}(\vec{x}_a) \, H_A^\alpha(\vec{x}_b) \, J_\alpha^{\frac{1}{2}}(\vec{x}_a) \, J_\alpha^{\frac{1}{2}}(\vec{x}_b) \\ &\quad \times \int_0^1 \mathrm{d}\vec{x}_c J_\gamma(\vec{x}_c) \, \langle \gamma, \Phi_c | \mathcal{M} | \alpha, \Phi_b \rangle^* \langle \gamma, \Phi_c | \mathcal{M} | \alpha, \Phi_a \rangle \\ &= \frac{1}{4} |\mathcal{C}|^2 \Delta_\gamma |F_A^\alpha|^2 \end{aligned}$$ (B.21)

where the total phase-space volume Δ_γ is given by [135, 136]

$$\Delta_\gamma \equiv \int_0^1 \mathrm{d}\vec{x}_c J_\gamma(\vec{x}_c) = \frac{1}{S_\gamma} \frac{1}{(2\pi)^{3n_\gamma - 4}} \left(\frac{\pi}{2}\right)^{n_\gamma - 1} \frac{s^{n_\gamma - 2}}{(n_\gamma - 1)!(n_\gamma - 2)!} \tag{B.22}$$

and the function F is defined as

$$F_A^\alpha = \int_0^1 \mathrm{d}\vec{x}_a H_A^\alpha(\vec{x}_a) \, J_\alpha^{\frac{1}{2}}(\vec{x}_a) \tag{B.23}$$

Using the Cauchy-Schwarz inequality, the orthonormality condition for the basis yields

$$|F_A^\alpha|^2 \leq \int_0^1 \mathrm{d}\vec{x}_a |H_{l_u}^\alpha(\vec{x}_a)|^2 \int_0^1 \mathrm{d}\vec{x}_b J_\alpha(\vec{x}_b) = \Delta_\alpha \tag{B.24}$$

Therefore, we obtain

$$b_A^{\alpha\gamma} \leq \frac{1}{4} \Delta_\alpha \Delta_\gamma |\mathcal{C}|^2 \tag{B.25}$$

The strongest bound is obtained if the sign applies in Eq. (B.25). The inequality becomes

$$\frac{1}{4} \Delta_\alpha \Delta_\gamma |\mathcal{C}|^2 \leq \frac{1}{4} \tag{B.26}$$

To realize the optimal bound within a given phase-space parameterization, the following condition should be satisfied:

$$\frac{H_A^\alpha(\vec{x}_a)}{J_\alpha^{\frac{1}{2}}(\vec{x}_a)} = \text{constant} \tag{B.27}$$

The condition can be satisfied if both $H_A^\alpha(\vec{x}_a)$ and $J_\alpha(\vec{x}_a)$ are constants. Since a constant basis function is a member of commonly used orthonormal bases, the condition reduces to the requirement of a constant Jacobian determinant for the phase-space parameterization. Ref. [136] introduces an algorithm to achieves it.

We observe that the bounds in Eq. (B.26) are symmetric under the exchange $\alpha \leftrightarrow \gamma$, although the states a and c may have different number or species of particles. We may exploit this property by performing polarization sums to either the initial or final state, when applying the formalism to scattering processes.

(b) In elastic scattering, i.e. $\alpha = \gamma$, the unitarity constraint may be expressed in terms of the a-coefficients rather than b-coefficients. After an analogous derivation, we arrive at the following

optimal constraint:

$$|\text{Re}\,\frac{1}{2}\Delta_\alpha \mathcal{C}| \leq \frac{1}{2} \tag{B.28}$$

$$0 \leq |\text{Im}\,\frac{1}{2}\Delta_\alpha \mathcal{C} - \frac{1}{4}| \leq 1 \tag{B.29}$$

The above discussion can be also applied to the case that the independence of phase-space parameters results from summing over degenerate states (polarization, color, etc.). Explicitly, for a set of degenerate states S^2,

$$\sum_{\gamma \in S}(\langle \gamma, \Phi_c | \mathcal{M} | \alpha, \Phi_a \rangle)^* \langle \gamma, \Phi_c | \mathcal{M} | \alpha, \Phi_b \rangle = |\mathcal{C}_S|^2 \tag{B.30}$$

where $|\mathcal{C}_S|^2$ is independent of the phase-space parameters $\vec{x}_a, \vec{x}_b, \vec{x}_c$. With an optimal choice of kinematic variables and basis we obtain the bound

$$\frac{1}{4}\Delta_\alpha \Delta_\gamma |\mathcal{C}_S|^2 \leq \frac{1}{4} \tag{B.31}$$

B.4   Generic case: recursive kinematics

For the concrete evaluation of unitarity bounds in the generic case where the phase-space parameter dependence remains nontrivial, we have to choose a specific phase-space parameterization. In our calculations, we used the standard recursive generation of $2 \to n$ phase space in terms of $2 \to 2$ scattering followed by a tree of $1 \to 2$ momentum splittings. The phase-space manifold ultimately is mapped to the the $3n - 4$-dimensional unit hypercube, $\vec{x} \in [0, 1]^{3n-4}$. Below, we review this construction and provide the detailed formulas.

We denote the n-body phase-space element with total four-momentum Q^μ as $\mathrm{d}\Phi_n\{Q^\mu\}$.

1. For $n > 2$, the phase-space element is given by

$$\mathrm{d}\Phi_n\{Q^\mu\} = \delta^{(4)}(\sum_{i=1}^{n} p_i^\mu - Q^\mu)\,\mathrm{d}\Phi_n$$

$$= \frac{\mathrm{d}^4 p_n}{(2\pi)^3}\delta(p_n^2 - m_n^2)\,\mathrm{d}\Phi_{n-1}\{Q^\mu - p_n^\mu\} \tag{B.32}$$

---

[2]We require all states in S to have indentical particle numbers and symmetry factors.

Working in the c.m. frame of Q^μ where $Q^\mu_{\text{CM}} = (\sqrt{Q^2}, 0, 0, 0)$, we obtain:

$$\frac{\mathrm{d}^4 p_n}{(2\pi)^3} \delta(p_n^2 - m_n^2) = \frac{\mathrm{d}^4 p_{n,\text{CM}}}{(2\pi)^3} \delta(p_{n,\text{CM}}^2 - m_n^2)$$

$$= \frac{\rho^3(Q^2, m_n, \sum_{i=1}^{n-1} m_i) x_{3n-6}^2 \sin\theta_n}{8\pi E_{n,\text{CM}}} \mathrm{d}x_{3n-6}\mathrm{d}x_{3n-5}\mathrm{d}x_{3n-4} \quad \text{(B.33)}$$

where the function ρ is defined by

$$\rho(s, m_1, m_2) = \sqrt{[s - (m_1 + m_2)^2][s - (m_1 - m_2)^2]} \quad \text{(B.34)}$$

and the four-momentum $p_{n,\text{CM}}$ is parameterized to

$$p^\mu_{n,\text{CM}} = (E_{n,\text{CM}}, \vec{p}_{n,\text{CM}}) \quad \text{(B.35)}$$

$$\vec{p}_{n,\text{CM}} = x_{3n-6}\rho(Q^2, m_n, \sum_{i=1}^{n-1} m_i)(\sin\theta_n \cos\phi_n, \sin\theta_n \sin\phi_n, \cos\theta_n) \quad \text{(B.36)}$$

$$E_{n,\text{CM}} = \sqrt{|\vec{p}_{n,\text{CM}}|^2 + m_n^2} \quad \text{(B.37)}$$

$$\theta_n = \pi x_{3n-5} \quad \text{(B.38)}$$

$$\phi_n = 2\pi x_{3n-4} \quad \text{(B.39)}$$

The corresponding four-momentum in original frame can be obtained by a simple Lorentz boost:

$$p^\mu_n = \Lambda(Q_{\text{CM}}, Q, p_{n,\text{CM}})$$

$$= p^\mu_{n,\text{CM}} - 2(Q^\mu_{\text{CM}} + Q^\mu)\frac{(Q_{\text{CM}} + Q) \cdot p_{n,\text{CM}}}{(Q_{\text{CM}} + Q)^2} + 2Q^\mu \frac{Q_{\text{CM}} \cdot p_{n,\text{CM}}}{Q^2} \quad \text{(B.40)}$$

2. For $n = 2$, working again in the c.m. frame, the formulas simplify accordingly:

$$\mathrm{d}\Phi_2(Q) = \mathrm{d}x_1 \mathrm{d}x_2 \frac{\rho(Q^2, m_1, m_2)\sin\theta}{128\pi^4\sqrt{Q^2}}. \quad \text{(B.41)}$$

The corresponding $p_{1,\text{CM}}$ and $p_{2,\text{CM}}$ can be parametrized to

$$p^\mu_{1,\text{CM}} = (\sqrt{p_{CM}^2 + m_1^2}, -\vec{p}_{\text{CM}}) \quad \text{(B.42)}$$

$$p^\mu_{2,\text{CM}} = (\sqrt{p_{CM}^2 + m_2^2}, \vec{p}_{\text{CM}}) \quad \text{(B.43)}$$

$$\vec{p}_{\text{CM}} = \rho(Q^2, m_1, m_2)(\sin\theta_2 \cos\phi_2, \sin\theta_2 \sin\phi_2, \cos\theta_2) \quad \text{(B.44)}$$

$$\theta_2 = \pi x_1 \quad \text{(B.45)}$$

$$\phi_2 = 2\pi x_2 \quad \text{(B.46)}$$

Similarly, the corresponding four-momenta in the original frame can be obtained via the Lorentz boost given in Eq. (B.40).

Bibliography

[1] Georges Aad et al. Observation of a new particle in the search for the Standard Model Higgs boson with the ATLAS detector at the LHC. *Phys. Lett.*, B716:1–29, 2012, arXiv:1207.7214.

[2] Serguei Chatrchyan et al. Observation of a new boson at a mass of 125 GeV with the CMS experiment at the LHC. *Phys. Lett.*, B716:30–61, 2012, arXiv:1207.7235.

[3] Mark Trodden. Electroweak baryogenesis. *Rev. Mod. Phys.*, 71:1463–1500, 1999, arXiv:hep-ph/9803479.

[4] J. Ellis, J. R. Espinosa, G. F. Giudice, A. Hoecker, and A. Riotto. The Probable Fate of the Standard Model. *Phys. Lett.*, B679:369–375, 2009, arXiv:0906.0954.

[5] Giuseppe Degrassi, Stefano Di Vita, Joan Elias-Miro, Jose R. Espinosa, Gian F. Giudice, Gino Isidori, and Alessandro Strumia. Higgs mass and vacuum stability in the Standard Model at NNLO. *JHEP*, 08:098, 2012, arXiv:1205.6497.

[6] E. A. Reyes Rojas. *The Higgs Boson at LHC and the Vacuum Stability of the Standard Model*. PhD thesis, Colombia, U. Natl., 2015, arXiv:1511.03651.

[7] Wolfgang Kilian, Thorsten Ohl, and Jurgen Reuter. WHIZARD: Simulating Multi-Particle Processes at LHC and ILC. *Eur. Phys. J.*, C71:1742, 2011, arXiv:0708.4233.

[8] J. Alwall, R. Frederix, S. Frixione, V. Hirschi, F. Maltoni, O. Mattelaer, H. S. Shao, T. Stelzer, P. Torrielli, and M. Zaro. The automated computation of tree-level and next-to-leading order differential cross sections, and their matching to parton shower simulations. *JHEP*, 07:079, 2014, arXiv:1405.0301.

[9] Wolfgang Kilian, Sichun Sun, Qi-Shu Yan, Xiaoran Zhao, and Zhijie Zhao. New Physics in multi-Higgs boson final states. *JHEP*, 06:145, 2017, arXiv:1702.03554.

[10] Wolfgang Kilian, Sichun Sun, Qi-Shu Yan, Xiaoran Zhao, and Zhijie Zhao. Multi-Higgs Production and Unitarity in Vector-Boson Fusion at Future Hadron Colliders. 2018, arXiv:1808.05534.

[11] M. Tanabashi et al. Review of Particle Physics. *Phys. Rev.*, D98(3):030001, 2018.

[12] Michael E. Peskin and Daniel V. Schroeder. *An Introduction to Quantum Field Theory*. West-view Press, 1995.

[13] Matthew D. Schwartz. *Quantum Field Theory and the Standard Model*. Cambridge University Press, 2014.

[14] R. K. Ellis, W. J. Stirling, and B. R. Webber. *QCD and Collider Physics*. Cambridge University Press, 2003.

[15] F. Englert and R. Brout. Broken Symmetry and the Mass of Gauge Vector Mesons. *Phys. Rev. Lett.*, 13:321–323, 1964. [,157(1964)].

[16] Peter W. Higgs. Broken Symmetries and the Masses of Gauge Bosons. *Phys. Rev. Lett.*, 13:508–509, 1964. [,160(1964)].

[17] The ATLAS collaboration. Measurement of the Higgs boson coupling properties in the $H \to ZZ^* \to 4\ell$ decay channel at $\sqrt{s} = 13$ TeV with the ATLAS detector. ATLAS-CONF-2017-043, 2017.

[18] CMS Collaboration. Higgs to WW measurements with 15.2 fb^{-1} of 13 TeV proton-proton collisions. CMS-PAS-HIG-16-021, 2017.

[19] CMS Collaboration. Search for Higgs boson pair production in the final state containing two photons and two bottom quarks in proton-proton collisions at $\sqrt{s} = 13$ TeV. CMS-PAS-HIG-17-008, 2017.

[20] Albert M Sirunyan et al. Observation of $t\bar{t}$H production. *Phys. Rev. Lett.*, 120(23):231801, 2018, arXiv:1804.02610.

[21] W. Buchmuller and D. Wyler. Effective Lagrangian Analysis of New Interactions and Flavor Conservation. *Nucl. Phys.*, B268:621–653, 1986.

[22] Howard Georgi. On-shell effective field theory. *Nucl. Phys.*, B361:339–350, 1991.

[23] Kenneth G. Wilson. Renormalization group and critical phenomena. 1. Renormalization group and the Kadanoff scaling picture. *Phys. Rev.*, B4:3174–3183, 1971.

[24] Steven Weinberg. Phenomenological Lagrangians. *Physica*, A96(1-2):327–340, 1979.

[25] Celine Degrande, Nicolas Greiner, Wolfgang Kilian, Olivier Mattelaer, Harrison Mebane, Tim Stelzer, Scott Willenbrock, and Cen Zhang. Effective Field Theory: A Modern Approach to Anomalous Couplings. *Annals Phys.*, 335:21–32, 2013, arXiv:1205.4231.

[26] Steven Weinberg. Baryon and Lepton Nonconserving Processes. *Phys. Rev. Lett.*, 43:1566–1570, 1979.

[27] Andre de Gouvea, Juan Herrero-Garcia, and Andrew Kobach. Neutrino Masses, Grand Unification, and Baryon Number Violation. *Phys. Rev.*, D90(1):016011, 2014, arXiv:1404.4057.

[28] B. Grzadkowski, M. Iskrzynski, M. Misiak, and J. Rosiek. Dimension-Six Terms in the Standard Model Lagrangian. *JHEP*, 10:085, 2010, arXiv:1008.4884.

[29] G. F. Giudice, C. Grojean, A. Pomarol, and R. Rattazzi. The Strongly-Interacting Light Higgs. *JHEP*, 06:045, 2007, arXiv:hep-ph/0703164.

[30] Vernon Barger, Lisa L. Everett, C. B. Jackson, and Gabe Shaughnessy. Higgs-Pair Production and Measurement of the Triscalar Coupling at LHC(8,14). *Phys. Lett.*, B728:433–436, 2014, arXiv:1311.2931.

[31] Hong-Jian He, Jing Ren, and Weiming Yao. Probing new physics of cubic Higgs boson interaction via Higgs pair production at hadron colliders. *Phys. Rev.*, D93(1):015003, 2016, arXiv:1506.03302.

[32] Roberto Contino, Margherita Ghezzi, Christophe Grojean, Margarete Muhlleitner, and Michael Spira. Effective Lagrangian for a light Higgs-like scalar. *JHEP*, 07:035, 2013, arXiv:1303.3876.

[33] Alexei A. Starobinsky. Spectrum of relict gravitational radiation and the early state of the universe. *JETP Lett.*, 30:682–685, 1979. [,767(1979)].

[34] Alexei A. Starobinsky. A New Type of Isotropic Cosmological Models Without Singularity. *Phys. Lett.*, B91:99–102, 1980. [,771(1980)].

[35] Alan H. Guth. The Inflationary Universe: A Possible Solution to the Horizon and Flatness Problems. *Phys. Rev.*, D23:347–356, 1981. [Adv. Ser. Astrophys. Cosmol.3,139(1987)].

[36] Andrei D. Linde. A New Inflationary Universe Scenario: A Possible Solution of the Horizon, Flatness, Homogeneity, Isotropy and Primordial Monopole Problems. *Phys. Lett.*, 108B:389–393, 1982. [Adv. Ser. Astrophys. Cosmol.3,149(1987)].

[37] Andreas Albrecht and Paul J. Steinhardt. Cosmology for Grand Unified Theories with Radiatively Induced Symmetry Breaking. *Phys. Rev. Lett.*, 48:1220–1223, 1982. [Adv. Ser. Astrophys. Cosmol.3,158(1987)].

[38] Fedor L. Bezrukov and Mikhail Shaposhnikov. The Standard Model Higgs boson as the inflaton. *Phys. Lett.*, B659:703–706, 2008, arXiv:0710.3755.

[39] F. Bezrukov and M. Shaposhnikov. Standard Model Higgs boson mass from inflation: Two loop analysis. *JHEP*, 07:089, 2009, arXiv:0904.1537.

[40] Ippei Obata, Takashi Miura, and Jiro Soda. Dynamics of Electroweak Gauge Fields during and after Higgs Inflation. *Phys. Rev.*, D90(4):045005, 2014, arXiv:1405.3091.

[41] T. Plehn, M. Spira, and P. M. Zerwas. Pair production of neutral Higgs particles in gluon-gluon collisions. *Nucl. Phys.*, B479:46–64, 1996, arXiv:hep-ph/9603205. [Erratum: Nucl. Phys.B531,655(1998)].

[42] Ulrich Baur, Tilman Plehn, and David L. Rainwater. Measuring the Higgs boson self coupling at the LHC and finite top mass matrix elements. *Phys. Rev. Lett.*, 89:151801, 2002, arXiv:hep-ph/0206024.

[43] Qiang Li, Qi-Shu Yan, and Xiaoran Zhao. Higgs Pair Production: Improved Description by Matrix Element Matching. *Phys. Rev.*, D89(3):033015, 2014, arXiv:1312.3830.

[44] Biplob Bhattacherjee and Arghya Choudhury. Role of supersymmetric heavy Higgs boson production in the self-coupling measurement of 125 GeV Higgs boson at the LHC. *Phys. Rev.*, D91:073015, 2015, arXiv:1407.6866.

[45] U. Baur, T. Plehn, and David L. Rainwater. Determining the Higgs boson selfcoupling at hadron colliders. *Phys. Rev.*, D67:033003, 2003, arXiv:hep-ph/0211224.

[46] Jing Ren, Rui-Qing Xiao, Maosen Zhou, Yaquan Fang, Hong-Jian He, and Weiming Yao. LHC Search of New Higgs Boson via Resonant Di-Higgs Production with Decays into 4W. *JHEP*, 06:090, 2018, arXiv:1706.05980.

[47] U. Baur, T. Plehn, and David L. Rainwater. Probing the Higgs selfcoupling at hadron colliders using rare decays. *Phys. Rev.*, D69:053004, 2004, arXiv:hep-ph/0310056.

[48] Weiming Yao. Studies of measuring Higgs self-coupling with $HH \rightarrow b\bar{b}\gamma\gamma$ at the future hadron colliders. In *Proceedings, 2013 Community Summer Study on the Future of U.S. Particle Physics: Snowmass on the Mississippi (CSS2013): Minneapolis, MN, USA, July 29-August 6, 2013*, 2013, arXiv:1308.6302.

[49] Felix Kling, Tilman Plehn, and Peter Schichtel. Maximizing the significance in Higgs boson pair analyses. *Phys. Rev.*, D95(3):035026, 2017, arXiv:1607.07441.

[50] Jeong Han Kim, Yasuhito Sakaki, and Minho Son. Combined analysis of double Higgs production via gluon fusion at the HL-LHC in the effective field theory approach. *Phys. Rev.*, D98(1):015016, 2018, arXiv:1801.06093.

[51] Jung Chang, Kingman Cheung, Jae Sik Lee, Chih-Ting Lu, and Jubin Park. Higgs-boson-pair production $H(\rightarrow b\bar{b})H(\rightarrow \gamma\gamma)$ from gluon fusion at the HL-LHC and HL-100 TeV hadron collider. 2018, arXiv:1804.07130.

[52] Andreas Papaefstathiou, Li Lin Yang, and Jose Zurita. Higgs boson pair production at the LHC in the $b\bar{b}W^+W^-$ channel. *Phys. Rev.*, D87(1):011301, 2013, arXiv:1209.1489.

[53] U. Baur, T. Plehn, and David L. Rainwater. Examining the Higgs boson potential at lepton and hadron colliders: A Comparative analysis. *Phys. Rev.*, D68:033001, 2003, arXiv:hep-ph/0304015.

[54] Matthew J. Dolan, Christoph Englert, and Michael Spannowsky. Higgs self-coupling measurements at the LHC. *JHEP*, 10:112, 2012, arXiv:1206.5001.

[55] Alan J. Barr, Matthew J. Dolan, Christoph Englert, and Michael Spannowsky. Di-Higgs final states augMT2ed – selecting hh events at the high luminosity LHC. *Phys. Lett.*, B728:308–313, 2014, arXiv:1309.6318.

[56] Lan-Chun Lu, Chun Du, Yaquan Fang, Hong-Jian He, and Huijun Zhang. Searching heavier Higgs boson via di-Higgs production at LHC Run-2. *Phys. Lett.*, B755:509–522, 2016, arXiv:1507.02644.

[57] Danilo Enoque Ferreira de Lima, Andreas Papaefstathiou, and Michael Spannowsky. Standard model Higgs boson pair production in the ($b\bar{b}$)($b\bar{b}$) final state. *JHEP*, 08:030, 2014, arXiv:1404.7139.

[58] J. Katharina Behr, Daniela Bortoletto, James A. Frost, Nathan P. Hartland, Cigdem Issever, and Juan Rojo. Boosting Higgs pair production in the $b\bar{b}b\bar{b}$ final state with multivariate techniques. *Eur. Phys. J.*, C76(7):386, 2016, arXiv:1512.08928.

[59] Qing-Hong Cao, Gang Li, Bin Yan, Dong-Ming Zhang, and Hao Zhang. Double Higgs production at the 14 TeV LHC and a 100 TeV pp collider. *Phys. Rev.*, D96(9):095031, 2017, arXiv:1611.09336.

[60] Alan J. Barr, Matthew J. Dolan, Christoph Englert, Danilo Enoque Ferreira de Lima, and Michael Spannowsky. Higgs Self-Coupling Measurements at a 100 TeV Hadron Collider. *JHEP*, 02:016, 2015, arXiv:1412.7154.

[61] Andreas Papaefstathiou. Discovering Higgs boson pair production through rare final states at a 100 TeV collider. *Phys. Rev.*, D91(11):113016, 2015, arXiv:1504.04621.

[62] Qiang Li, Zhao Li, Qi-Shu Yan, and Xiaoran Zhao. Probe Higgs boson pair production via the $3\ell2j+\not{E}$ mode. *Phys. Rev.*, D92(1):014015, 2015, arXiv:1503.07611.

[63] Xiaoran Zhao, Qiang Li, Zhao Li, and Qi-Shu Yan. Discovery potential of Higgs boson pair production through $4\ell+\not{E}$ final states at a 100 TeV collider. *Chin. Phys.*, C41(2):023105, 2017, arXiv:1604.04329.

[64] R. Contino et al. Physics at a 100 TeV pp collider: Higgs and EW symmetry breaking studies. *CERN Yellow Report*, (3):255–440, 2017, arXiv:1606.09408.

[65] Dorival Goncalves, Tao Han, Felix Kling, Tilman Plehn, and Michihisa Takeuchi. Higgs boson pair production at future hadron colliders: From kinematics to dynamics. *Phys. Rev.*, D97(11):113004, 2018, arXiv:1802.04319.

[66] Tilman Plehn and Michael Rauch. The quartic higgs coupling at hadron colliders. *Phys. Rev.*, D72:053008, 2005, arXiv:hep-ph/0507321.

[67] T. Binoth, S. Karg, N. Kauer, and R. Ruckl. Multi-Higgs boson production in the Standard Model and beyond. *Phys. Rev.*, D74:113008, 2006, arXiv:hep-ph/0608057.

[68] Duane A. Dicus, Chung Kao, and Wayne W. Repko. Self Coupling of the Higgs boson in the processes $pp \rightarrow ZHHH + X$ and $pp \rightarrow WHHH + X$. *Phys. Rev.*, D93(11):113003, 2016, arXiv:1602.05849.

[69] F. Maltoni, E. Vryonidou, and M. Zaro. Top-quark mass effects in double and triple Higgs production in gluon-gluon fusion at NLO. *JHEP*, 11:079, 2014, arXiv:1408.6542.

[70] Andreas Papaefstathiou and Kazuki Sakurai. Triple Higgs boson production at a 100 TeV proton-proton collider. *JHEP*, 02:006, 2016, arXiv:1508.06524.

[71] Chien-Yi Chen, Qi-Shu Yan, Xiaoran Zhao, Yi-Ming Zhong, and Zhijie Zhao. Probing triple-Higgs productions via $4b2\gamma$ decay channel at a 100 TeV hadron collider. *Phys. Rev.*, D93(1):013007, 2016, arXiv:1510.04013.

[72] Benjamin Fuks, Jeong Han Kim, and Seung J. Lee. Probing Higgs self-interactions in proton-proton collisions at a center-of-mass energy of 100 TeV. *Phys. Rev.*, D93(3):035026, 2016, arXiv:1510.07697.

[73] Pankaj Agrawal, Debashis Saha, and Ambresh Shivaji. Production of HHH and $HHV(V = \gamma, Z)$ at the hadron colliders. *Phys. Rev.*, D97(3):036006, 2018, arXiv:1708.03580.

[74] Benjamin Fuks, Jeong Han Kim, and Seung J. Lee. Scrutinizing the Higgs quartic coupling at a future 100 TeV proton-proton collider with taus and b-jets. *Phys. Lett.*, B771:354–358, 2017, arXiv:1704.04298.

[75] Roberto Pittau. Status of MadLoop/aMC@NLO. In *International Workshop on Future Linear Colliders (LCWS11) Granada, Spain, September 26-30, 2011*, 2012, arXiv:1202.5781.

[76] J. Pumplin, D. R. Stump, J. Huston, H. L. Lai, Pavel M. Nadolsky, and W. K. Tung. New generation of parton distributions with uncertainties from global QCD analysis. *JHEP*, 07:012, 2002, arXiv:hep-ph/0201195.

[77] K. Arnold et al. VBFNLO: A Parton level Monte Carlo for processes with electroweak bosons. *Comput. Phys. Commun.*, 180:1661–1670, 2009, arXiv:0811.4559.

[78] J. Baglio et al. VBFNLO: A Parton Level Monte Carlo for Processes with Electroweak Bosons – Manual for Version 2.7.0. 2011, arXiv:1107.4038.

[79] J. Baglio et al. Release Note - VBFNLO 2.7.0. 2014, arXiv:1404.3940.

[80] Valentin Hirschi and Olivier Mattelaer. Automated event generation for loop-induced processes. *JHEP*, 10:146, 2015, arXiv:1507.00020.

[81] S. Dawson, C. Jackson, L. H. Orr, L. Reina, and D. Wackeroth. Associated Higgs production with top quarks at the large hadron collider: NLO QCD corrections. *Phys. Rev.*, D68:034022, 2003, arXiv:hep-ph/0305087.

[82] Gavin Cullen et al. G$OSAM$-2.0: a tool for automated one-loop calculations within the Standard Model and beyond. *Eur. Phys. J.*, C74(8):3001, 2014, arXiv:1404.7096.

[83] Fabio Cascioli, Philipp Maierhofer, and Stefano Pozzorini. Scattering Amplitudes with Open Loops. *Phys. Rev. Lett.*, 108:111601, 2012, arXiv:1111.5206.

[84] Johannes Bellm, Stefan Gieseke, Nicolas Greiner, Gudrun Heinrich, Simon Platzer, Christian Reuschle, and Johann Felix von Soden-Fraunhofen. Anomalous coupling, top-mass and parton-shower effects in W^+W^- production. *JHEP*, 05:106, 2016, arXiv:1602.05141.

[85] Michelangelo L. Mangano, Mauro Moretti, Fulvio Piccinini, and Michele Treccani. Matching matrix elements and shower evolution for top-quark production in hadronic collisions. *JHEP*, 01:013, 2007, arXiv:hep-ph/0611129.

[86] C. G. Lester and D. J. Summers. Measuring masses of semiinvisibly decaying particles pair produced at hadron colliders. *Phys. Lett.*, B463:99–103, 1999, arXiv:hep-ph/9906349.

[87] Alan Barr, Christopher Lester, and P. Stephens. m(T2): The Truth behind the glamour. *J. Phys.*, G29:2343–2363, 2003, arXiv:hep-ph/0304226.

[88] Alan J. Barr and Christopher G. Lester. A Review of the Mass Measurement Techniques proposed for the Large Hadron Collider. *J. Phys.*, G37:123001, 2010, arXiv:1004.2732.

[89] A. J. Barr, T. J. Khoo, P. Konar, K. Kong, C. G. Lester, K. T. Matchev, and M. Park. Guide to transverse projections and mass-constraining variables. *Phys. Rev.*, D84:095031, 2011, arXiv:1105.2977.

[90] Won Sang Cho, James S. Gainer, Doojin Kim, Konstantin T. Matchev, Filip Moortgat, Luc Pape, and Myeonghun Park. On-shell constrained M_2 variables with applications to mass measurements and topology disambiguation. *JHEP*, 08:070, 2014, arXiv:1401.1449.

[91] Torbjorn Sjostrand, Stephen Mrenna, and Peter Z. Skands. PYTHIA 6.4 Physics and Manual. *JHEP*, 05:026, 2006, arXiv:hep-ph/0603175.

[92] Matteo Cacciari, Gavin P. Salam, and Gregory Soyez. FastJet User Manual. *Eur. Phys. J.*, C72:1896, 2012, arXiv:1111.6097.

[93] Matteo Cacciari, Gavin P. Salam, and Gregory Soyez. The anti-k_t jet clustering algorithm. *JHEP*, 04:063, 2008, arXiv:0802.1189.

[94] S. Ovyn, X. Rouby, and V. Lemaitre. DELPHES, a framework for fast simulation of a generic collider experiment. 2009, arXiv:0903.2225.

[95] J. de Favereau, C. Delaere, P. Demin, A. Giammanco, V. Lemaitre, A. Mertens, and M. Selvaggi. DELPHES 3, A modular framework for fast simulation of a generic collider experiment. *JHEP*, 02:057, 2014, arXiv:1307.6346.

[96] Wolfgang Kilian, Thorsten Ohl, Juergen Reuter, and Marco Sekulla. High-Energy Vector Boson Scattering after the Higgs Discovery. *Phys. Rev.*, D91:096007, 2015, arXiv:1408.6207.

[97] Wolfgang Kilian, Thorsten Ohl, Juergen Reuter, and Marco Sekulla. Resonances at the LHC beyond the Higgs boson: The scalar/tensor case. *Phys. Rev.*, D93(3):036004, 2016, arXiv:1511.00022.

[98] Celine Degrande, Claude Duhr, Benjamin Fuks, David Grellscheid, Olivier Mattelaer, and Thomas Reiter. UFO - The Universal FeynRules Output. *Comput. Phys. Commun.*, 183:1201–1214, 2012, arXiv:1108.2040.

[99] Giovanni Ossola, Costas G. Papadopoulos, and Roberto Pittau. Reducing full one-loop amplitudes to scalar integrals at the integrand level. *Nucl. Phys.*, B763:147–169, 2007, arXiv:hep-ph/0609007.

[100] Giovanni Ossola, Costas G. Papadopoulos, and Roberto Pittau. On the Rational Terms of the one-loop amplitudes. *JHEP*, 05:004, 2008, arXiv:0802.1876.

[101] P. Draggiotis, M. V. Garzelli, C. G. Papadopoulos, and R. Pittau. Feynman Rules for the Rational Part of the QCD 1-loop amplitudes. *JHEP*, 04:072, 2009, arXiv:0903.0356.

[102] Celine Degrande. Automatic evaluation of UV and R2 terms for beyond the Standard Model Lagrangians: a proof-of-principle. *Comput. Phys. Commun.*, 197:239–262, 2015, arXiv:1406.3030.

[103] John Ellis, Veronica Sanz, and Tevong You. The Effective Standard Model after LHC Run I. *JHEP*, 03:157, 2015, arXiv:1410.7703.

[104] Georges Aad et al. Constraints on non-Standard Model Higgs boson interactions in an effective Lagrangian using differential cross sections measured in the $H \to \gamma\gamma$ decay channel at $\sqrt{s} = 8\text{TeV}$ with the ATLAS detector. *Phys. Lett.*, B753:69–85, 2016, arXiv:1508.02507.

[105] D. de Florian et al. Handbook of LHC Higgs Cross Sections: 4. Deciphering the Nature of the Higgs Sector. 2016, arXiv:1610.07922.

[106] Daniel de Florian and Javier Mazzitelli. Higgs Boson Pair Production at Next-to-Next-to-Leading Order in QCD. *Phys. Rev. Lett.*, 111:201801, 2013, arXiv:1309.6594.

[107] Kaustubh Agashe, Roberto Contino, and Alex Pomarol. The Minimal composite Higgs model. *Nucl. Phys.*, B719:165–187, 2005, arXiv:hep-ph/0412089.

[108] Shinya Kanemura, Kunio Kaneta, Naoki Machida, Shinya Odori, and Tetsuo Shindou. Single and double production of the Higgs boson at hadron and lepton colliders in minimal composite Higgs models. *Phys. Rev.*, D94(1):015028, 2016, arXiv:1603.05588.

[109] D. R. T. Jones and S. T. Petcov. Heavy Higgs Bosons at LEP. *Phys. Lett.*, 84B:440–444, 1979.

[110] Matthew J. Dolan, Christoph Englert, Nicolas Greiner, and Michael Spannowsky. Further on up the road: $hhjj$ production at the LHC. *Phys. Rev. Lett.*, 112:101802, 2014, arXiv:1310.1084.

[111] Liu-Sheng Ling, Ren-You Zhang, Wen-Gan Ma, Lei Guo, Wei-Hua Li, and Xiao-Zhou Li. NNLO QCD corrections to Higgs pair production via vector boson fusion at hadron colliders. *Phys. Rev.*, D89(7):073001, 2014, arXiv:1401.7754.

[112] Matthew J. Dolan, Christoph Englert, Nicolas Greiner, Karl Nordstrom, and Michael Spannowsky. $hhjj$ production at the LHC. *Eur. Phys. J.*, C75(8):387, 2015, arXiv:1506.08008.

[113] Fady Bishara, Roberto Contino, and Juan Rojo. Higgs pair production in vector-boson fusion at the LHC and beyond. *Eur. Phys. J.*, C77(7):481, 2017, arXiv:1611.03860.

[114] Ernesto Arganda, Claudia Garcia-Garcia, and Maria Jose Herrero. Probing the Higgs self-coupling through double Higgs production in vector boson scattering at the LHC. 2018, arXiv:1807.09736.

[115] R. Frederix, S. Frixione, V. Hirschi, F. Maltoni, O. Mattelaer, P. Torrielli, E. Vryonidou, and M. Zaro. Higgs pair production at the LHC with NLO and parton-shower effects. *Phys. Lett.*, B732:142–149, 2014, arXiv:1401.7340.

[116] J. Baglio, A. Djouadi, R. Grober, M. M. Muhlleitner, J. Quevillon, and M. Spira. The measurement of the Higgs self-coupling at the LHC: theoretical status. *JHEP*, 04:151, 2013, arXiv:1212.5581.

[117] Christoph Englert, Qiang Li, Michael Spannowsky, Mengmeng Wang, and Lei Wang. VBS $W^{\pm}W^{\pm}H$ production at the HL-LHC and a 100 TeV pp-collider. *Int. J. Mod. Phys.*, A32(18):1750106, 2017, arXiv:1702.01930.

[118] Roberto Contino, Christophe Grojean, Duccio Pappadopulo, Riccardo Rattazzi, and Andrea Thamm. Strong Higgs Interactions at a Linear Collider. *JHEP*, 02:006, 2014, arXiv:1309.7038.

[119] A. S. Belyaev, P. B. Schaefers, and M. C. Thomas. Precise test of Higgs properties via triple Higgs production in VBF at future colliders. 2018, arXiv:1801.10157.

[120] John M. Cornwall, David N. Levin, and George Tiktopoulos. Derivation of Gauge Invariance from High-Energy Unitarity Bounds on the s Matrix. *Phys. Rev.*, D10:1145, 1974. [Erratum: Phys. Rev.D11,972(1975)].

[121] U. Baur and D. Zeppenfeld. Unitarity Constraints on the Electroweak Three Vector Boson Vertices. *Phys. Lett.*, B201:383–389, 1988.

[122] F. Maltoni, J. M. Niczyporuk, and S. Willenbrock. The Scale of fermion mass generation. *Phys. Rev.*, D65:033004, 2002, arXiv:hep-ph/0106281.

[123] Duane A. Dicus and Hong-Jian He. Scales of fermion mass generation and electroweak symmetry breaking. *Phys. Rev.*, D71:093009, 2005, arXiv:hep-ph/0409131.

[124] Duane A. Dicus and Hong-Jian He. Scales of mass generation for quarks, leptons and majorana neutrinos. *Phys. Rev. Lett.*, 94:221802, 2005, arXiv:hep-ph/0502178.

[125] Zhao-Huan Yu, Qi-Shu Yan, and Peng-Fei Yin. Detecting interactions between dark matter and photons at high energy e^+e^- colliders. *Phys. Rev.*, D88(7):075015, 2013, arXiv:1307.5740.

[126] T. Kinoshita. Mass singularities of Feynman amplitudes. *J. Math. Phys.*, 3:650–677, 1962.

[127] T. D. Lee and M. Nauenberg. Degenerate Systems and Mass Singularities. *Phys. Rev.*, 133:B1549–B1562, 1964. [,25(1964)].

[128] R. E. Cutkosky. Singularities and discontinuities of Feynman amplitudes. *J. Math. Phys.*, 1:429–433, 1960.

[129] M. J. G. Veltman. Unitarity and causality in a renormalizable field theory with unstable particles. *Physica*, 29:186–207, 1963.

[130] Simon Brass, Christian Fleper, Wolfgang Kilian, Jurgen Reuter, and Marco Sekulla. Transversal Modes and Higgs Bosons in Electroweak Vector-Boson Scattering at the LHC. 2018, arXiv:1807.02512.

[131] Genessis Perez, Marco Sekulla, and Dieter Zeppenfeld. Anomalous quartic gauge couplings and unitarization for the vector boson scattering process $pp \to W^+W^+jjX \to \ell^+\nu_\ell\ell^+\nu_\ell jjX$. *Eur. Phys. J.*, C78(9):759, 2018, arXiv:1807.02707.

[132] M. Jacob and G. C. Wick. On the general theory of collisions for particles with spin. *Annals Phys.*, 7:404–428, 1959. [Annals Phys.281,774(2000)].

[133] Mamta Dahiya, Sukanta Dutta, and Rashidul Islam. Investigating perturbative unitarity in the presence of anomalous couplings. *Phys. Rev.*, D93(5):055013, 2016, arXiv:1311.4523.

[134] Tyler Corbett, O. J. P. Eboli, and M. C. Gonzalez-Garcia. Unitarity Constraints on Dimension-Six Operators. *Phys. Rev.*, D91(3):035014, 2015, arXiv:1411.5026.

[135] R. Kleiss, W. James Stirling, and S. D. Ellis. A New Monte Carlo Treatment of Multiparticle Phase Space at High-energies. *Comput. Phys. Commun.*, 40:359, 1986.

[136] Simon Platzer. RAMBO on diet. 2013, arXiv:1308.2922.